Direct laser writing of polymeric and metallic nanostructures via optically induced local thermal effect

Quang Cong Tong

To cite this version:

Quang Cong Tong. Direct laser writing of polymeric and metallic nanostructures via optically induced local thermal effect. Other [cond-mat.other]. Université Paris Saclay (COmUE), 2016. English. NNT : 2016SACLN073 . tel-01424960

HAL Id: tel-01424960
https://theses.hal.science/tel-01424960

Submitted on 3 Jan 2017

NNT : 2016SACLN073

THÈSE DE DOCTORAT
DE
L'UNIVERSITÉ PARIS-SACLAY
PRÉPARÉE A
L'ECOLE NORMALE SUPERIEURE PARIS-SACLAY

ÉCOLE DOCTORALE N°575
electrical, optical, bio-physics and engineering
Spécialité de doctorat : **physics**

by

M. Quang Cong TONG

Direct laser writing of polymeric and metallic nanostructures via optically induced local thermal effect

Defensed at ENS Cachan, December 13th 2016.

Examining committee :

Mr. BRUNEL Marc	Professor, University of Rennes 1	President
Mr. COOLEN Laurent	Associate professor, UPMC	Referee
Mr. SOPPERA Olivier	Director of research CNRS, Mulhouse	Referee
Mr. LAI Ngoc Diep	Associate professor, ENS Cachan	Director
Ms. LEDOUX-RAK Isabelle	Professor, ENS Cachan	Co-supervisor
Mr. JOURNET Bernard	Associate professor, ENS Cachan	Co-supervisor

Acknowledgment

The past three years have been a time of tremendous learning and growth for me both professionally and personally. I would not have been able to complete my graduate studies at ENS Cachan without the support and guidance of my advisors, colleagues, thesis committee, friends and most-importantly-my family.

First, I would like to express my deepest gratitude to my supervisor, Prof. Ngoc Diep Lai, for the continuous support of my PhD study and related research, for his patience, motivation, and immense knowledge. His guidance helped me in all the time of research and writing of this thesis.

As well, I would like to express my sincere thanks and immense pleasure to my co-supervisors, Prof. Bernard Journet and Prof. Isabell Ledoux-Rak, for their scientific guidance, consistent support, and encouragement throughout the duration of my PhD.

I would like to thank to my labmates with whom I worked over the years– especially, Thuy Trang, Au Huong, Luong Hoang, Minh Thanh, Mo, Jacqueline Remmel. It has been a true pleasure working with them.

I also deeply thank to my colleagues and friends, who gave me their helps and times during three years– especially, Dr. Rasta Ghasemi and Mr. Joseph Lautru for their great helps with clean-room facilities and nano-fabrications.

Besides my advisors, I would like to thank the rest of my thesis committee: Prof. Olivier Soppera, Prof. Laurent Coolen, and Prof. Marc Brunel, for their insightful comments and encouragement, but also for the question which incensed me to widen my research from various perspectives.

Last but not the least, I would like to thank my family for the love, support, and constant encouragement, I have gotten over the years.

List of publications (related to this work)

- **Tong, Q. C.**, Luong, M. H., Tran, T. M., Remmel, J., Do, M. T., Kieu, D. M., Ghasemi, R., Nguyen, D. T., Lai, N. D., "*Realization of desired plasmonic nanostructures via direct laser writing technique*," accepted, Journal of Electronic Materials (2016).
- **Tong, Q. C.**, Luong, M. H., Remmel, J., Do, M. T., Lai, N. D., "*Optically induced thermal effect for fabrication of desired plasmonic nanostructures*," submitted (2016).
- Au, T. H., Trinh, D. T., **Tong, Q. C.**, Do, D. B., Nguyen, D. P., Phan, M. H., Lai, N. D., "*Direct laser writing of magneto-photonic sub-microstructures*," submitted (2016).
- **Tong, Q. C.**, Nguyen, D. T. T., Do, M. T., Luong, M. H., Journet, B., Ledoux-Rak, I., Lai, N. D., "*Direct laser writing of polymeric nanostructures via optically induced local thermal effect*," Applied Physics Letters 108(18), 183104 (2016).
- **Tong, Q. C.**, Do, M. T., Journet, B., Ledoux-Rak, I., Lai, N. D., "*Fabrication of controllable form submicrometer structures on positive photoresist by one-photon absorption direct laser writing technique*," Proc. SPIE 9885, Photonic Crystal Materials and Devices XII, 988519 (April 2016)
- Do, M. T., **Tong, Q. C.**, Lidiak, A., Luong, M. H., Ledoux-Rak, I., Lai, N. D., "*Nano-patterning of gold thin film by thermal annealing combined with laser interference techniques*," Applied Physics A 122(4) (2016).
- Nguyen, D. T. T., **Tong, Q. C.**, Ledoux-Rak, I., Lai, N. D., "*One-step fabrication of submicrostructures by low one-photon absorption direct laser writing technique with local thermal effect*," Journal of Applied Physics 119(1), 13101 (2016).
- Do, M. T., **Tong, Q. C.**, Luong, M. H., Lidiak, A., Ledoux-Rak, I., Lai, N. D., "*Fabrication and Characterization of Large-Area Unpatterned and Patterned Plasmonic Gold Nanostructures*," Journal of Electronic Materials 45(5), 2347–2353 (2016).
- Nguyen, D. T. T., Pelissier, A., Montes, K., **Tong, Q. C.**, Ngo, H. M., Ledoux-Rak, I., Lai, N. D., "*Deterministic embedding of a single gold nanoparticle into polymeric microstructures by direct laser writing technique,*" Proc. SPIE 9884, Nanophotonics VI, 98842C (April 2016).
- Nguyen, D. T. T., Au, T. H., **Tong, Q. C.**, Luong, M. H., Pelissier, A., Montes,

K., Ngo, H. M., Do, M. T., Do, D. B., Trinh, D. T., Nguyen, T. H., Palpant, B., Hsu, C. C., Ledoux-Rak, I., Lai, N. D., “*Coupling of a single active nanoparticle to a polymer-based photonic structure*,” Journal of Science: Advanced Materials and Devices 1, 18-30 (2016).

- Nguyen, T. T. N., Luong, M. H., Do, M. T., Kieu, D. M., Li, Q., Nguyen, D. T. T., **Tong, Q. C.**, Ledoux-Rak, I., Lai, N. D., “*Micro and nanostructuration of polymer materials and applications*,” Proc. SPIE 9171, Nanobiosystems: Processing, Characterization, and Applications VII, 91710O (August 2014).

Conference contributions

- **Tong, Q. C.**, Luong, M. H., Tran, T. M., Remmel, J., Do, M. T., Kieu, D. M., Ghasemi, R., Nguyen, T., Lai, N. D., “*Realization of desired plasmonic nanostructures via direct laser writing technique*,” International Workshop on Advanced Materials and Nanotechnology 2016 (IWAMN 2016), Hanoi, Vietnam (November 2016), Poster.
- **Tong, Q. C.**, Do, M. T., Journet, B., Ledoux-Rak, I., Lai, N. D., “*Fabrication of controllable form submicrometer structures on positive photoresist by one-photon absorption direct laser writing technique*,” SPIE Photonic Europe, Brussels (April 2016), Poster.
- Nguyen, D. T. T., Pelissier, A., Montes, K., **Tong, Q. C.**, Ngo, H. M., Ledoux-Rak, I., Lai, N. D., “*Deterministic embedding of a single gold nanoparticle into polymeric microstructures by direct laser writing technique,*” SPIE Photonic Europe, Brussels (April 2016), Poster.
- **Tong, Q. C.**, Do, M. T., Do, M. T., Journet, B., Ledoux-Rak, I., Lai, N. D., “*Réalisation de structures sub-micrométriques de forme “positive” par une photorésine positive*,” Optique Bretagne, Rennes (Juillet 2015), Poster.
- **Tong, Q. C.**, Journet, B., Ledoux-Rak, I., Lai, N. D., “*Realization of polymer-based 2d or 3d arbitrary form microresonators by low one photon absorption direct laser writing technique*,” *7th* International Workshop on Advanced Materials Science and Nanotechnology (IWAMSN 2014), Ha Long City, Vietnam (November 2014), Poster.

- **Tong, Q. C.**, Journet, B., Ledoux-Rak, I., Lai, N. D., "*Realisation de micro-resonateurs en materiaux polymères, de forme arbitraire, par la methode de gravure directe par laser avec absorption lineaire ultra-faible*," Les 34 *èmes* JNOG, Nice, France (Octobre 2014), Poster.
- **Tong, Q. C.**, Journet, B., Ledoux-Rak, I., Lai, N. D., "*Study of 2D and 3D polymer-based microresonators: application for compact optoelectronic oscillators*," USTH Workshop, Montpellier (September 2014), Oral.
- Nguyen, T. T. N., Luong, M. H., Do, M. T., Kieu, D. M., Li, Q., Nguyen, D. T. T., **Tong, Q. C.**, Ledoux-Rak, I., Lai, N. D., "*Micro and nanostructuration of polymer materials and applications*," SPIE Optics and Photonics, San Diego (August 2014), Invited talk.

Contents

Chapter 1

General introduction

Nanostructures occur in nature in many different forms, for example: insect wings, bird feathers, or plant leaves. The Morpho butterflies are famous for the magnificent bright blue wing color, which is not a result of pigmentation, but of the interaction of light with the periodic microscopic structures covering the morpho's wings as shown in figure 1.1(a). Similarly, many other living creatures also perform such kind of structural colors. Lotus leaf possesses self-cleaning property which derives from the ultrahydrophobic micro-nanostructures on its surface. Inspired by those wonderful properties of natural nanostructures, humans have been trying to mimic nature by creating artificial nanostructures, which then lead to various potential applications in electronics, photonics, and biology. Among the recent progresses in the fabrication of artificial nanostructures, photonic crystals and plasmonic structures have drawn a great attention due to their particularly promising properties.

Photonic crystal (PhC) is a special class of optical media with periodic modulation of dielectric constant, allowing the confinement and manipulation of light. PhC is characterized by a photonic bandgap (PBG) – a range of frequencies within which light cannot propagate through the PhC. Many PhC-based optical components have been realized such as lenses [1], polarizers, beam splitters [2], optical fibers [3], prisms [4] or wavelength division multiplexers [5]. PhCs exist in different forms as shown in figure 1.1(b). The simplest example of PhC is a one-dimensional (1D) structure formed from periodic multi-layer dielectric stacks (such as a Bragg mirror). The thickness and the number of dielectric layers can be optimized for the highest reflection at a certain wavelength range corresponding to its PBG [6]. Two-dimensional (2D) PhCs are periodic in two directions and homogeneous in the third. An example of 2D PhCs is a periodically arranged system of dielectric cylinders in air or air-holes in a dielectric background. These 2D structures

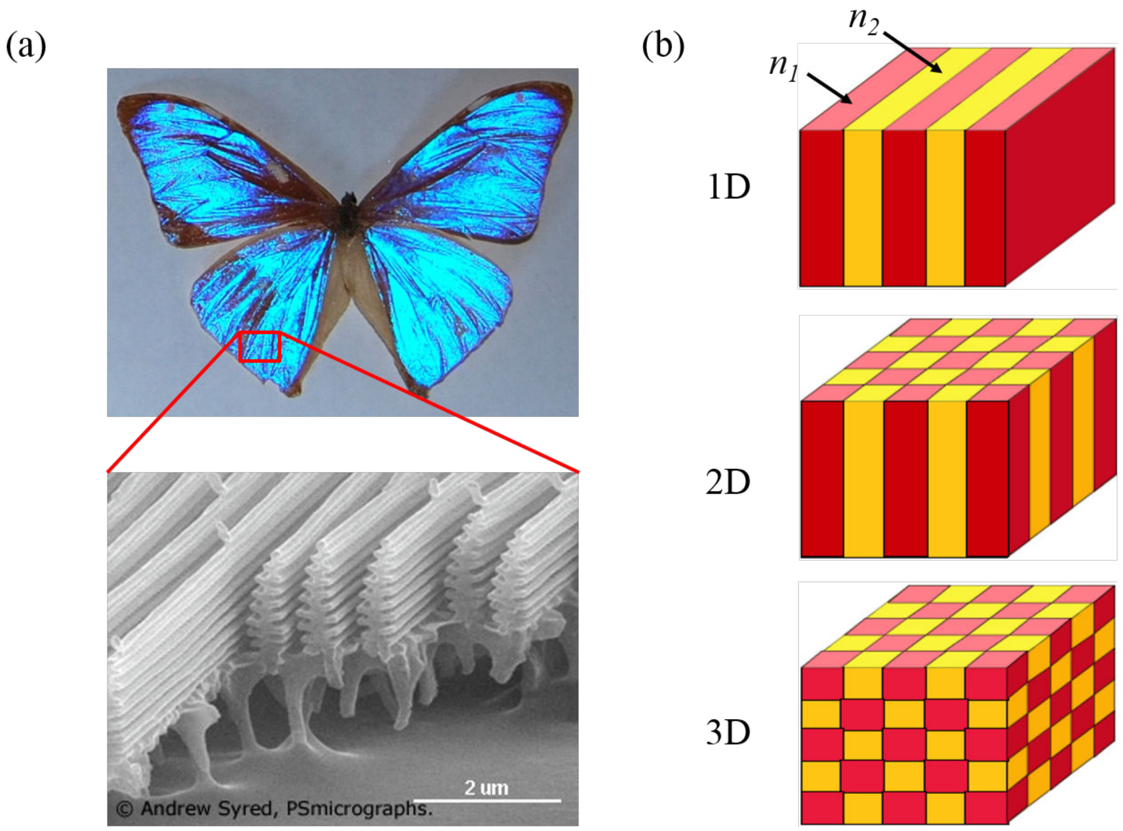

Figure 1.1: (a) A male Morpho aega and a SEM image of the wings. Photo from http://www.microscopy-uk.org.uk/mag/indexmag.html. (b) Models of 1D, 2D and 3D photonic crystal structures. The colors represent materials with different refractive indices (n_1 and n_2).

can have a PBG in the planes of periodicity. The complete confinement of light can only be achieved by extending the PBGs to the third dimension. Such structures with permittivity modulation along all three directions are called three-dimensional (3D) PhC. Furthermore, defects can be introduced to all 1D, 2D and 3D PhCs to create waveguides and cavities, in which light with wavelengths satisfying resonant conditions can be confined. Compared with common cavities such as micro-ring or micro-disk, microcavities based on PhC can provide small mode volumes and high quality factors [7]. Such structures have great potential for strong-coupling cavity quantum electrodynamics [8], enhancement and suppression of spontaneous emission [9], novel light sources [10], and dynamic filters in optical communication [11, 12].

Plasmonics is a new research direction dealing with the interaction between an elec-

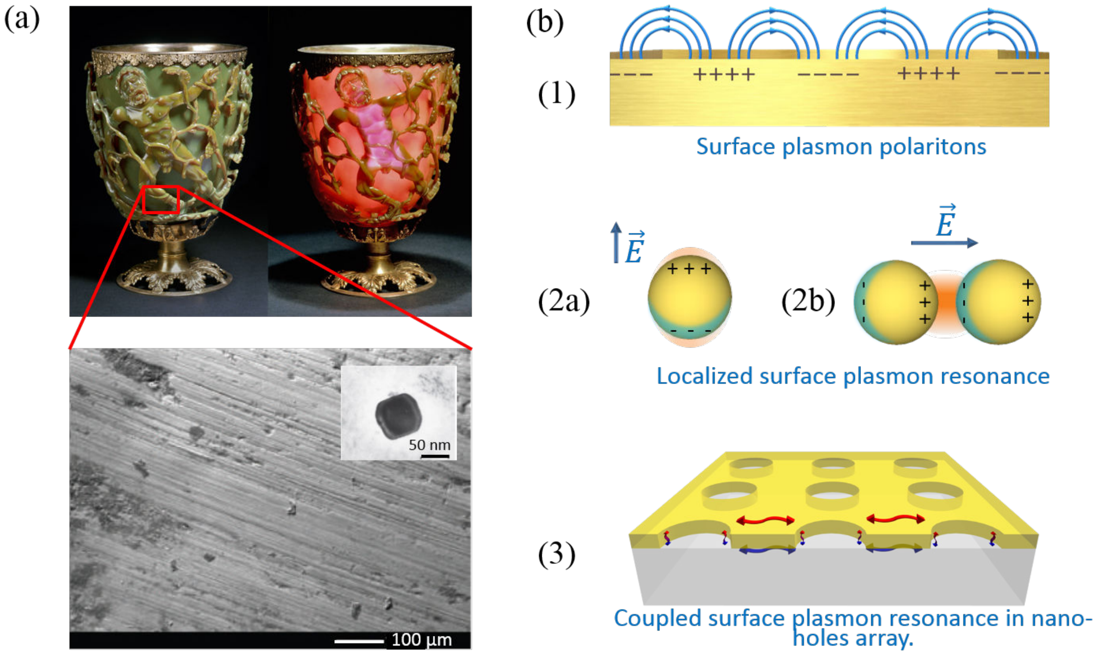

Figure 1.2: (a) The Lycurgus Cup in reflected (left) and transmitted (right) light, and backscattered electron image of cut-work fragment from the Lycurgus Cup (bottom). The inset shows TEM image of a silver-gold alloy particle within the glass of the Lycurgus Cup. (b) Plasmonic effects in different metallic nano-structures: (1) surface plasmon polariton (SPP) at a gold-air interface; (2a) localized surface plasmon resonance (LSPR) in a single nanoparticle; (2b) enhanced electric field (hotspots) in dimer nanoparticles; (3) coupled surface plasmon resonance in a nano-holes array.

tromagnetic field and free electrons in a metal. It is well-known that the first historical report of plasmonic phenomena is the Lycurgus Cup (British Museum, London, UK). Under ambient lighting, this Cup appears green, but when illuminated from inside, the transmitted light glints bright red as we can see in figure 1.2(a). Today, we know that this behavior is due to gold and silver nanoparticles embedded in the glass (see the inset of the figure 1.2(a)). Metallic nanostructures exhibit special optical properties deriving from a resonant oscillation of conduction electrons at the interface between a metal and a dielectric. This effect is called surface plasmon resonance (SPR) [13].

SPR can be divided into three categories with respect to plasmonic structures (see figure 1.2(b)): (1) surface plasmon polaritons (SPP) are infrared or visible-frequency electromagnetic waves, which occur and propagate along a metal-dielectric or metal-air interface, (2a)-(2b) localized surface plasmon resonance (LSPR) is the result of the con-

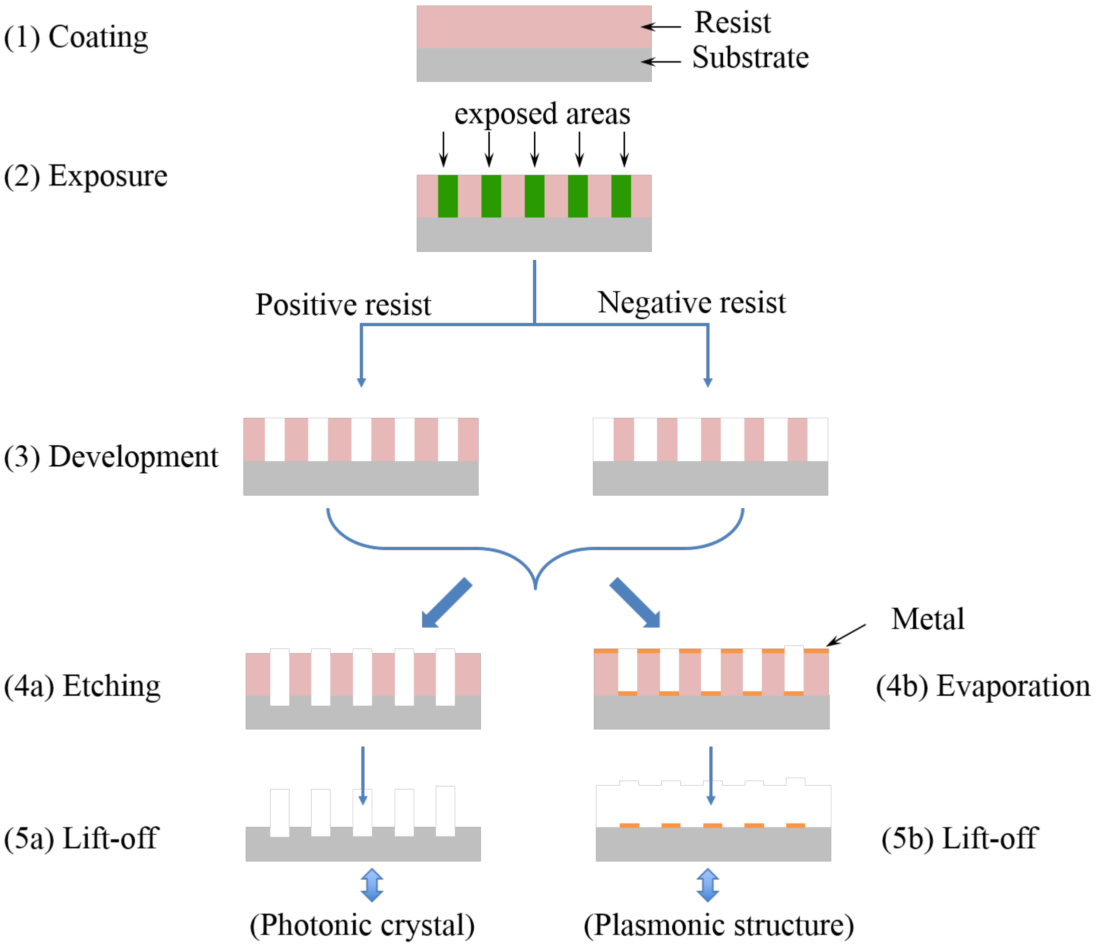

Figure 1.3: Schematic presentation of lithographic process used to fabricate photonic crystals and plasmonic structures.

finement of a surface plasmon in nanoparticles having a size smaller than the wavelength of the light used to excite the plasmon, (3) surface plasmon of periodic nanostructures results from the enhancement of the electromagnetic field near periodic metallic nano objects. Plasmonics is drawing more and more attention thanks to its wide range of applications in the field of electronics, photonics and biology. Examples include solar cells [14], thermal cancer treatments [15], light sources [16, 17], catalysis and nanostructure growths [18, 19], imaging devices [20], and nanosensors [21].

The fabrication of PhCs and plasmonic structures requires a submicrometer scale approach that could be implemented by an optical lithographic process shown in figure 1.3. In this lithographic process, the photoresist patterns are first fabricated through three steps: (1) spin-coating in which a photosensitive polymer film is coated on a planar substrate (for example, a thin silicon wafer); (2) exposing a pattern using a focused laser beam, or a large beam through a mask; (3) development. There are two kinds of photoresists for fabricating different-form patterns. “Negative” form structures (eg. air-holes in polymeric background) are usually fabricated by using positive photoresists and “positive” ones (eg. polymeric cylinders in air background) are realized by means of negative photoresists. Patterned photoresists are then used as templates to construct structures on other materials by etching or by an evaporation technique. For example, PhCs are obtained by etching substrates, where the patterned photoresist plays the role of a protection mask (4a), and subsequent removing the photoresist using a lift-off process (5a). On the other hand, plasmonic structures are obtained by a combination of the evaporation of metallic materials (4b) and lift-off process (5b).

A variety of techniques was developed to generate complex patterns of photoresists [22]. The most common methods used to pattern structures are electron-beam lithography (EBL), or ultra-violet (UV) photolithography. EBL allows the fabrication of 2D structures with high resolution. However, this method has disadvantages in terms of facility cost, fabrication throughput, and control process. UV lithography is more simple and can create large patterns but its resolution remain at the micrometer scale. In particular, these methods are very limited in the fabrication of arbitrary 3D structures. This problem stimulated the development of new methods, which should be simple and inexpensive during the high-resolution fabrication process.

Direct laser writing (DLW) is currently one of the most interesting fabrication technologies enabling desired 1D, 2D and 3D structures at sub-micrometer scale [23–25]. In regular DLW, a femto second laser beam is tightly focused into a photoresist by means of a high numerical aperture (NA) objective lens (OL). Only a tiny volume at focusing spot is sufficiently polymerized/depolymerized by two- or multi-photon absorption (TPA or MPA) mechanisms. By moving the focus of the laser beam, arbitrary structures can be written into the volume of photoresist. After the development step, desired structures could be obtained.

During the last two decades, DLW has been continuously optimized to overcome its limitations with respect to the structuring speed, sample volume, complicated pre- and post- processing, as well as minimum feature size and resolution. Some developments of DLW were demonstrated such as an improvement of feature size and resolution by using a shorter wavelength laser source [26], by applying a stimulated emission depletion (STED) lithography [27], or by an increase of the scanning speed by using pivoted galvanometric mirrors [24].

Our recent work indicated that 1D, 2D and 3D submicrometer structures, which are conventionally fabricated using TPA or MPA mechanism, could be perfectly obtained by means of a simple continuous-wave (cw) laser at a 532 nm wavelength with a modest power [28]. In this method, a photoresist that possesses a very low one-photon absorption (LOPA) effect at the wavelength of the excitation laser source is used so that the laser beam can write deeply inside the material. This method has many advantages such as simplicity, low-cost and compatibility. A lot of multi-dimensional microstructures have been fabricated with a SU8 negative photoresist via LOPA-based DLW. As compared to negative photoresists, positive resists are widely used because of their low shrinkage effect, easy to be tripped off after the pattern transfer. *Therefore, an investigation on LOPA-based DLW on positive resists is a strong motivation.*

Plasmonic structures display surface plasmon (SP) bands, ranging from UV to near infrared (NIR). The SP bands strongly depend on many factors such as period, size, and shape of plasmonic structures. For example, a SP band appears in the NIR domain for metallic structures showing a period of micrometer scale whereas the SP appearing in the UV-VIS range demands a metallic structure having a periodicity of less than one micrometer. Obviously, patterned photoresists with controllable forms and periodicities will be very useful for fabricating plasmonic structures. *Therefore, an investigation on the ways to produce plasmonic structures from patterned photoresists is very important for related applications.*

The aim of this thesis is to investigate the LOPA-based DLW for the fabrication of desired nanostructures on positive photoresists and metallic materials for PhCs and plasmonic applications. To do so, we target to fabricate high resolution polymeric template structures through photochemical and photothermal processes, which will open a new way for producing PhCs and plasmonic structures. Besides, in order to fabricate plasmonic structures based on polymeric templates, we concentrate on investigating a combination of thermal evaporation and lift-off processes as well as a combination of sputtering and thermal annealing technique. Furthermore, we also exploit the photothermal effect to demonstrate a one-step fabrication of plasmonic structures. Finally, we focus on investigation of some applications such as refractive index sensor, color printing, and data storages.

The thesis is organized as follows:

In chapter 2, we introduce the DLW technique, which will be used to fabricate desired structures on a positive photoresist by LOPA mechanism. Then, we demonstrate theoretically and experimentally the fabrication of sub-micrometer controllable-form structures from “negative” (air-hole in polymer background) to “positive” (polymeric cylinder in air background) forms. We design and fabricate many kinds of sub-micrometer periodic structures such as hexagonal, honeycomb, assembled-multiring lattices. We theoretically show that these structures possess a deep photonic bandgap even at low dielectric constant contrast.

In chapter 3, we implement the DLW technique for the fabrication of polymeric nanostructures on a S1805 positive photoresist through the photothermal process. We first investigate the thermal behaviour of S1805 positive photoresist. Then, we show the working principle of DLW on the S1805 positive photoresist by optically induced thermal effect. A simple thermal model is introduced to take into account and to clarify the photothermal processes occurring inside absorbing materials. Some advantages of this method such as high resolution and absence of accumulation effect are discussed in detail. We finally demonstrate experimentally the fabrication of 1D, 2D, and 3D sub-micrometer structures.

In chapter 4, by using results realized in chapter 2 and chapter 3, we present a method for patterning gold structures at micrometer scale, which could show a plasmonic effect in NIR range. These structures are obtained by using a combination of the templates fabricated by DLW and metal deposition and lift-off processes. By using finite-difference time domain (FDTD) method, we calculate theoretically the optical properties of gold nano hole arrays (GNHA) structures. We then demonstrate experimentally the optical properties of these GNHAs and also investigate the use of these structures for refractive index sensor application.

In chapter 5, we investigate the morphology and SP bands of dewetted gold films realized by the thermal annealing technique. We study the influence of gold thickness, thermal annealing temperature, and substrates on these Au nanostructures and on their SP bands. We then propose a method for patterning gold nanostructures by a combination of DLW lithography, metal deposition and thermal annealing technique. In this technique, a gold film is sputtered on the surface of a polymeric template and the whole sample is annealed at a high temperature to create desired gold nano structures. Plasmonic nanostructures having a double periodicity are demonstrated.

In chapter 6, we demonstrate a one-step method for fabricating arbitrary plasmonic structures of gold nanoisland films with tunable surface plasmon wavelength by local photothermal effect induced by the DLW technique. We first study gold films annealed by a large laser beam of high power. Then, we investigate the tuning of SP band of structures fabricated by scanning a focused laser beam. Finally, we consider some possibilities of applications such as data storage or color printing.

In the last chapter, we summarize our works and discuss about some applications and prospects of this work.

Chapter 2

Direct laser writing of desired submicrometer structures on positive photoresist

2.1 Introduction

Direct laser writing (DLW) is a commonly used technique for the fabrication of micro and submicrometer structures with arbitrary geometries [23]. In this technique, a laser beam is tightly focused into a photoresist inducing a photopolymerization or a photodepolymerization effect in a small volume. By scanning the focusing spot inside the photoresist, desired polymeric structures can be created. These structures are very useful and can be applied in different domains: physics, chemistry, and biology [29,30]. The fabrication of photonic structures by the DLW technique can be distinguished by the excitation mechanisms and also by the photochemical reaction in photoresists.

There exists two excitation mechanisms related to the laser sources and to the absorption band of photoresists: one-photon absorption (OPA) and two- or multiple-photon absorption (TPA or MPA). Generally, OPA occurs when the photoresist is excited by a laser beam (in DLW technique) or a simple incoherent light source (for optical lithography by mask) whose wavelength is located in the absorption band of the photoresist, which is usually in the ultraviolet (UV) range. The DLW technique dealing with this excitation mechanism allows to create desired structures with small feature sizes, but with a very limited thickness due to the linear absorption of the photoresist, which limits light propagation. It means that only one- and two-dimensional (1D and 2D) structures can be fabricated by this technique. In contrast, TPA or MPA offers a solution to overcome this limit thanks to the nonlinear absorption effect, which happens only at very high excitation intensity. In this case, a laser beam whose wavelength is usually in the near-infrared range, which is out of the linear absorption band of the photoresist, is employed. To enable photopolymerization/photodepolymerization effects, a femto-second laser beam and a high numerical aperture (NA) objective lens (OL) are required and used to induce a nonlinear absorption at the focusing region only. By scanning this focal spot in three-dimensions, arbitrary 1D, 2D and three-dimensional (3D) structures can be fabricated [31]. This TPA (or MPA)-based DLW is very useful and becomes a commercial fabrication technique [32]. However, this fabrication method is quite expensive due to the use of the femto-second laser and all related optical components. Recently, it was demonstrated that a simple continuous-wave (cw) laser with a modest power also allowed to realize desired 1D, 2D, and 3D submicrometer structures [28, 33], exactly as those obtained by TPA (or MPA) technique. The idea is to use a photoresist that possesses a very low OPA (LOPA) effect at the wavelength of the excitation laser source, so that the laser beam can penetrate deeply inside the material. By focusing such laser beam by a high NA OL (NA = 0.9), the light intensity at the focal spot is increased by $\approx 10^7$ times, resulting in an efficient photopolymerization/photodepolymerization effect at the focusing region. This LOPA-based DLW is of great interest because it combines advantages of the OPA and TPA (or MPA) fabrication techniques.

All fabrication techniques mentioned above can be applied to realize submicrometer structures in photoresists, which are divided into two categories: *negative* and *positive* photoresists. Depending on the photoresist type, different kinds of structures could be created. For a negative photoresist, light exposure induces a polymerization effect resulting in solid structures after washing out all un-exposed areas. This fabricated structure is called “positive structure” (material in air). The negative photoresist is used to fabricate any structure, in particular 3D photonic structures, because of its rigidity and indefectibility versus the development process. In contrast, a positive photoresist is depolymerized when exposed to light, resulting in remaining polymeric structures, which are inverse of light exposure pattern, and called “negative structures” (air holes). Positive photoresists are often used to create 1D and 2D structures, which are then served as templates to obtain structures in other materials, for example metallic materials for plasmonic applications. Due to the development effect and the weak rigidity, 3D structures are never realized by positive photoresists. However, it can be very interesting to work with a positive photoresist in term of resolution (structures size) and the removability

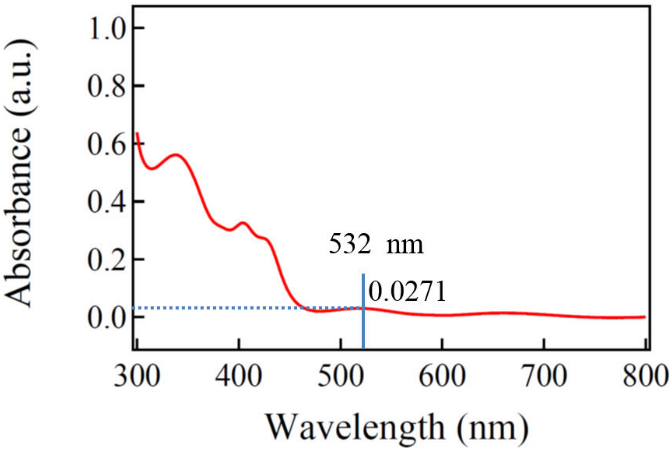

Figure 2.1: Absorption spectrum of S1805 positive photoresist. The films thickness is 600 nm.

property, as compared to negative photoresists. Positive photoresists are commonly used for fabrication of 1D and 2D structures by mask lithography technique. Recently, Cao *et al.* [34] have also demonstrated the use of TPA-based DLW technique to fabricate structures with a feature size of 85 nm on a positive AZ-4620 photoresist.

In this work, we investigate the use of LOPA-based DLW as a low-cost technique to fabricate desired submicrometer structures on positive photoresists, with controllable shapes (from negative to positive). In particular, we demonstrate that it is possible to obtain positive structures (material in air) with a feature size much smaller than the diffraction limit. This chapter is organized as follows. We first introduce the DLW setup, which will be used to realize all desired structures and theoretically calculate light patterns by scanning the focusing spot in two dimensions with controlled exposure doses. We then demonstrate experimentally the fabrication of polymeric nanostructures with controllable form by controlling the exposure doses and the structure periodicity. The PBG of these structures are theoretically calculated showing a possibility of direct applications of low dielectric constant materials. Finally, we make some conclusions and discuss about the potential applications of these fabricated structures.

2.2 Sample preparation and experimental setup

The photoresist used in this work is a commercial positive photoresist, S1805 (developed by MicroChem). The absorption spectrum of a S1805 film with a thickness of 600 nm

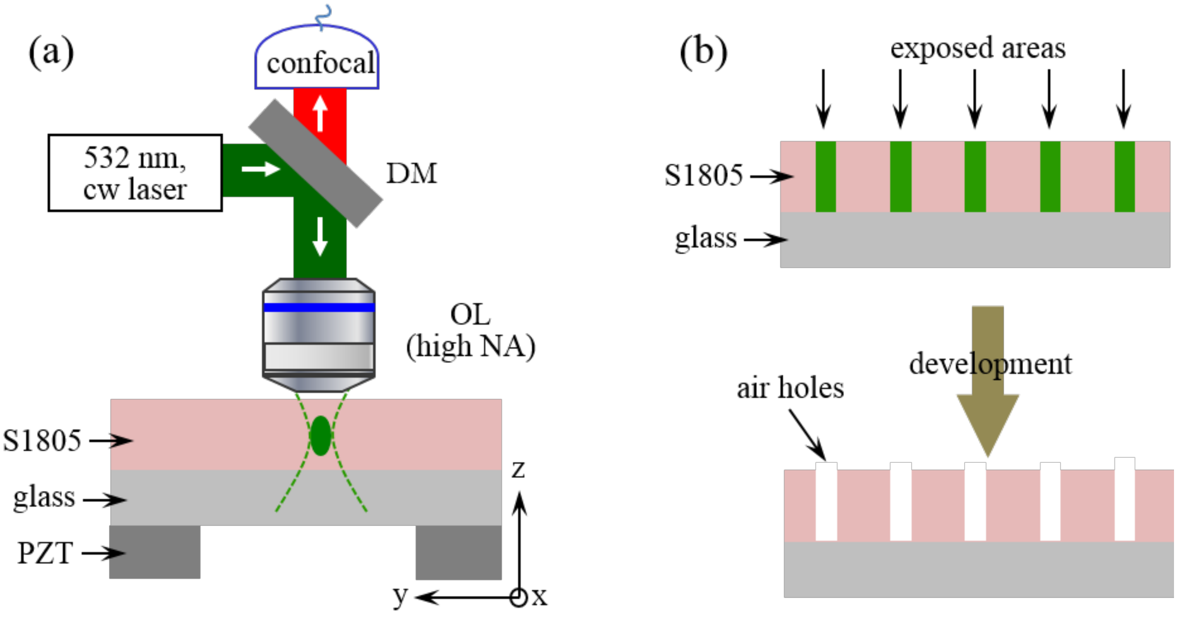

Figure 2.2: (a) Illustration of the one-photon absorption-based direct laser writing experiment used to realize desired submicrometer structures. PZT: piezoelectric translator; DM: dichroic mirror; NA: numerical aperture of microscope objective lens (OL). (b) Illustration of the fabrication process of 2D submicrometer structures on a positive photoresist (S1805).

is shown in figure 2.1. The absorbance of this photoresist is quite low at $\lambda = 532$ nm, allowing us to work in the LOPA regime. Figure 2.2(a) illustrates the experimental setup of the DLW system used in this work. A cw green laser beam ($\lambda = 532$ nm) was tightly focused into the sample by a high NA OL (NA = 0.9, air-immersion). Since the DLW operates with an OPA mechanism, the required laser power is very modest, in the range of few microwatts. Thanks to the use of a high NA OL, the light intensity at the focusing region is increased by a factor of about 10^7 times, which is high enough for depolymerizing the S1805 photoresist at the focusing spot. The sample was mounted on a 3D piezoelectric translator (PZT) connected to a computer control, which allows the focusing spot to move inside the sample following a pre-designed trajectory. The exposure doses were controlled by choosing the laser power and/or the scanning velocities of the PZT. A detection (confocal) system consisting of a set of lenses, a pinhole (diameter = 100 μm) and an avalanche photodiode was also built to determine the focusing position by detecting the reflection or fluorescence light from the focusing point. The fluorescent light was separated from the excitation beam by a dichroic mirror (DM).

To fabricate submicrometer structures, the photoresist was first coated on pre-treated glass substrates and then pre-baked at 115°C for two minutes to remove the residual solvent. The samples were kept in a dark room and were used for fabrication in the same day of their preparation. After exposure by the DLW system, the samples were developed in AZ 351 developer (diluted in water by a ratio of 1:5) for 60 seconds. All exposed parts were removed resulting in the desired structures (the unexposed parts), as illustrated in figure 2.2(b). All fabricated samples were examined first by optical microscope and then by scanning electron microscope (SEM).

2.3 Numerical calculation of 2D structures created by DLW technique

We first calculated the light patterns created by moving the focusing spot in the (xy)-plane (see setup in figure 2.2(a)), and following different configurations, such as square, hexagonal, etc. The light intensity distribution at the focusing spot was calculated numerically by using a vectorial diffraction theory [35]. It is shown that the NA of OL is a crucial factor for the resolution of the optical system or for the feature size of fabricated structures. With high NA, the transverse size of the focusing spot is about half of the excitation wavelength (diffraction limit). By moving this focusing spot, the light intensity is accumulated while keeping a resolution at $\lambda/2$. Figure 2.3(a) shows the moving path of the focusing beam to create a square pattern and figure 2.3(b) shows a corresponding theoretical light pattern by using an OL with $\mathrm{NA} = 0.9$ (air-immersion). We can see that the overlapping areas of two scanning lines possess a double intensity of a single line. Therefore, the exposure dose depends on the position of the scanning lines and their overlapping areas. Besides, the fabrication of polymeric structures depends strongly on the depolymerization rate that is proportional to the exposure dose, which is compared to a so-called depolymerization threshold, above which the depolymerized positive photoresist will be washed out during the development process (see figure 2.4(a)). The exposure dose depends on both light intensity (or power) and exposure time. In our calculation, we assumed theoretically that the dose is equivalent to the exposure intensity, and the threshold intensity is I_0. By scanning the focusing spot whose intensity is I_0 in a square structure, the overlapping of two scanning lines allow to obtain an air-hole, resulting in a square array of air-holes as illustrated in figure 2.3(c) (left). This kind of structure is called "negative structure" as defined above. Using higher doses ($2\mathrm{I}_0$ and $4\mathrm{I}_0$), different square structures with different filling factors (ratio between polymer material and air)

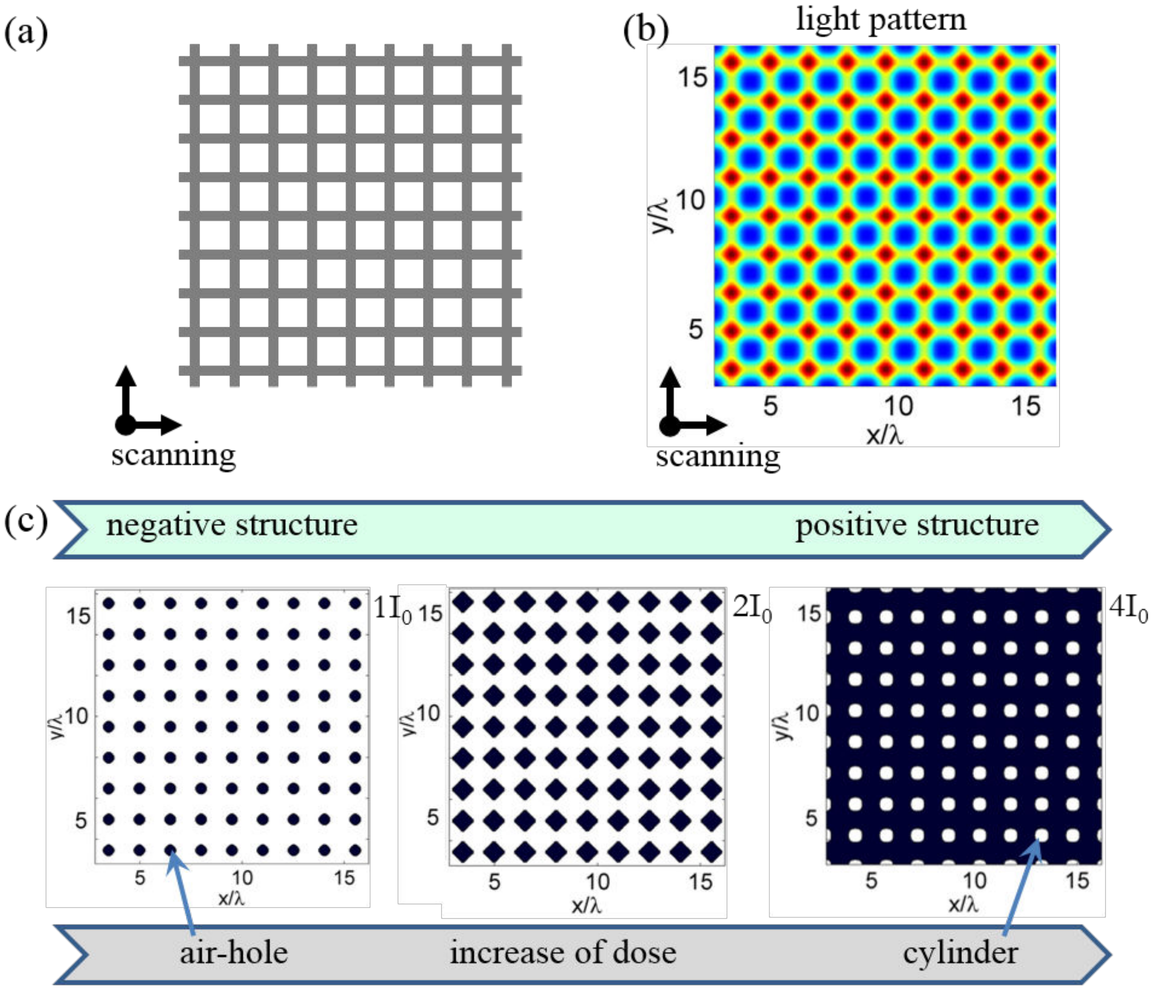

Figure 2.3: (a) Illustration of pattern realized by scanning the focusing spot of the DLW technique. (b) A theoretical light pattern (square form) obtained by scanning continuously the focal spot of an OL (NA = 0.9, $\lambda = 532$ nm) in $x-$ and $y-$directions. (c) Submicrometer structures, from negative (air-holes) to positive (polymeric cylinders) forms, can be created by choosing appropriate exposure dose, corresponding to different iso-intensities.

can be generated, as shown in figure 2.3(c) (center and right), respectively. By controlling the exposure dose in an appropriate range, we confirmed that the same structure (square in this case) can be generated with desired forms, from negative (air-holes) to positive (polymeric cylinders). In particular, the positive structures can be fabricated with a feature size smaller than the diffraction limit, because the structure size (the remained material) is not exposed to light and is not limited by the diffraction effect, as

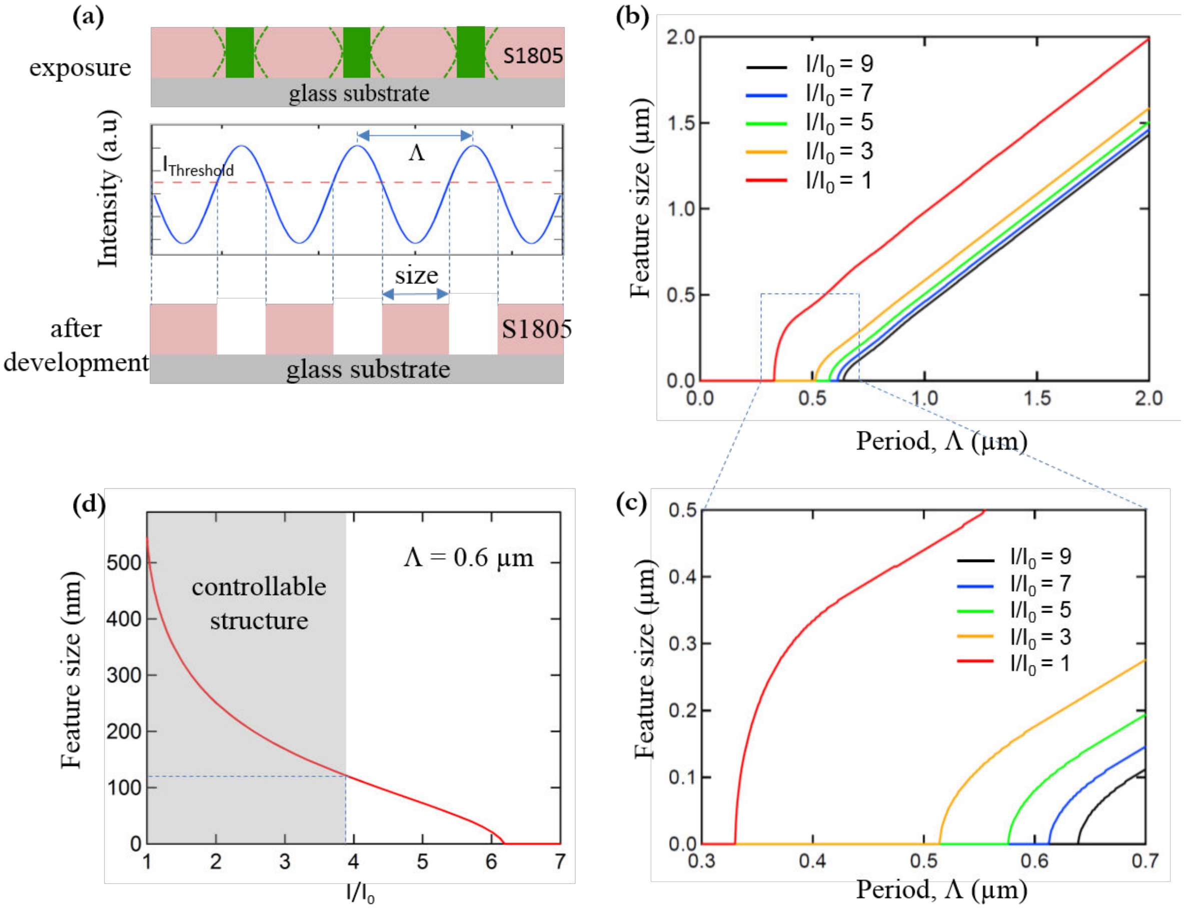

Figure 2.4: (a) Schematic illustration of the fabrication process of positive structures (polymeric cylinders) by using a positive photoresist (S1805). (b) Theoretical calculation of cylinders size as a function of the structure period (Λ) for different exposure doses. (c) Zoom in of the results shown in (b) for the periods in between 0.3 μm and 0.7 μm. (d) Theoretical calculation of the cylinders size as a function of exposure dose for the case of $\Lambda = 0.6\ \mu$m.

illustrated in figure 2.4(a). This can be called as “inverse fabrication” (IF) technique on positive photoresist.

As shown in figure 2.4(a), the final structure is obtained after the development process, and the structures size depends inversely on the exposure dose, *i.e.* small sizes are obtained for large exposure dose. It is important to note that, for 2D structures, the remain materials are obtained by scanning multiple lines, therefore the structure size depends also on the distance between the lines (period of structure). Figure 2.4(b) shows the feature sizes as a function of the structure periods for different exposure dose ratios

(I/I_0), where I_0 is the intensity threshold and I is the writing beam intensity. We note that the actual DLW operates by OPA mechanism, therefore there exists an accumulation effect of exposure doses when the scanning lines are very close [33]. With very large periods ($> 1\ \mu$m), the structures sizes vary linearly as a function of the exposure doses. However, with small periods ($0.3 - 1\ \mu$m), the structures sizes vary nonlinearly versus both exposure doses and structures periods, as shown in figure 2.4(c). It is clear that low exposure dose ($I/I_0 \approx 1$) allows to obtain structures with very small feature size and with very short lattice constant. In contrast, high exposure dose (*e.g.* $I/I_0 = 9$) induces a strong accumulation effect between scanning lines, and no structures can be obtained for periods smaller than 0.63 μm. Thus, by choosing a structure period, we can theoretically control the structures size down to zero. Figure 2.4(d) shows the feature size of a positive structure ($\Lambda = 0.6\ \mu$m) as a function of the writing dose. We see that the feature size decreases as the exposure dose increases, and the structure disappears for a dose ratio (I/I_0) larger than 6. We note that, in practice, the final structures size depends also on the developing process and on the quality of polymer materials, etc. Therefore, the smallest structures size is in the range of 100 nm, as indicated in figure 2.4(d).

2.4 Experimental results

2.4.1 Realization of 2D structures with controllable-form

Many kinds of 2D structures, periodic, quasi-periodic and arbitrary forms, have been fabricated by controlling the exposure dose and structure periods. 2D square structures, for example, have been fabricated by scanning the focusing spot along $x-$ and $y-$directions. By precisely controlling the scanning speed, structures with different filling factors are created. Figure 2.5(a) shows SEM images of 2D square structures with $\Lambda = 1\ \mu$m, fabricated by a constant laser power of 15 μW and with different scanning speeds of 10 μm/s, 6 μm/s, and 3 μm/s, respectively. We see that at the lower dose, corresponding to larger scanning speed (10 μm/s), the depolymerization takes place only at cross points of moving paths resulting in negative structures (air-holes). At higher dose, corresponding to the lower scanning speed (for example, 3 μm/s), the depolymerization occurs along moving path, the positive structures (polymeric cylinders) are then formed.

Figure 2.5(b) shows SEM images of other 2D square structures with a period of 0.6 μm fabricated by a constant laser beam power of 10 μW and with different scanning speeds of 9 μm/s, 7 μm/s, and 5 μm/s, respectively. Obviously, with a small period

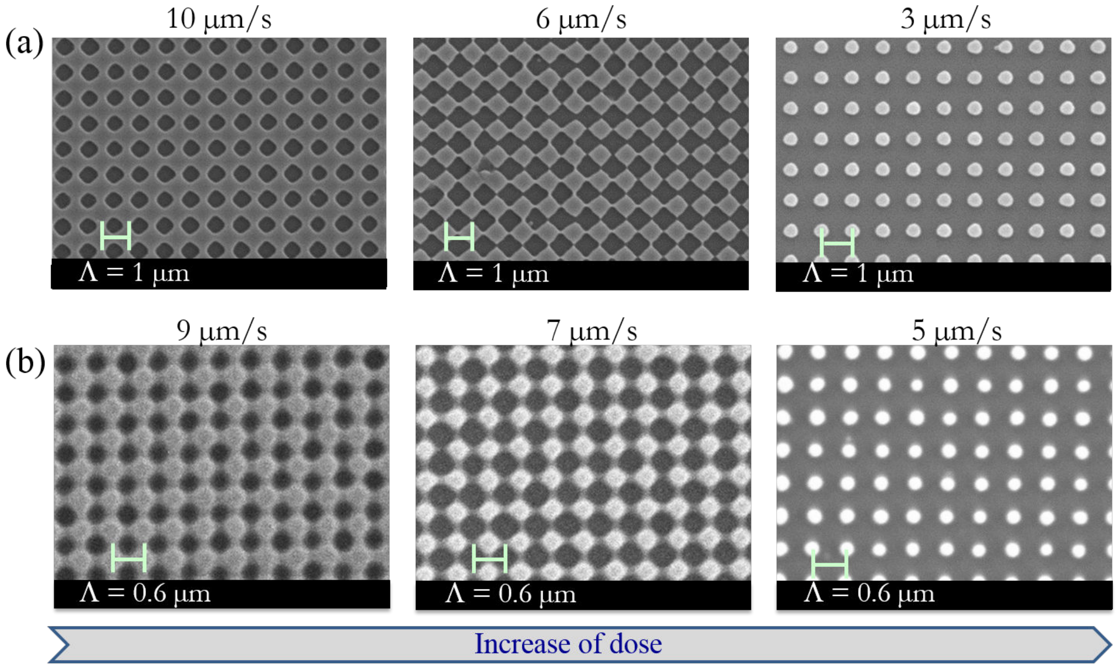

Figure 2.5: (a) SEM images of 2D square structures (period = 1 μm) fabricated by a laser power of 15 μW and scanning speeds of 10 μm/s, 6 μm/s, and 3 μm/s, respectively. (b) SEM images of 2D square structures (period = 0.6 μm) fabricated by a laser power of 10 μW and scanning speeds of 9 μm/s, 7 μm/s, and 5 μm/s, respectively.

($\Lambda = 0.6$ μm) the exposure dose required to create structures is smaller than that of large period ($\Lambda = 1$ μm) because the energy accumulation of adjacent doses is stronger. These experimental results are well consistent with those obtained numerically and presented in previous section. The fabricated structures are inverse of writing pattern and their forms are controllable.

Basically, the feature size is governed mainly by the size of the focusing spot, which is about $0.61\lambda/\mathrm{NA}$, according to Abbe's criterion. With small period ($\Lambda = 0.6$ μm), we also demonstrated that it is possible to realize structures with very small size by finely controlling the exposure dose. Figure 2.6 shows SEM images of 2D square structures with $\Lambda = 0.6$ μm fabricated by controlling the scanning speeds as 6 μm/s, 5 μm/s, and 4 μm/s, respectively (laser power is 10 μW). The feature size could be reduced from 300 nm to 150 nm corresponding to an increment of dose from $1.7I_0$ to $3.5I_0$ (figure 2.6(c)). We believe that it is possible to obtain structures with a feature size below 150 nm by using OLs with higher NA.

Similarly, arbitrary structures, for example "LOPA" letter, are also fabricated. Fig-

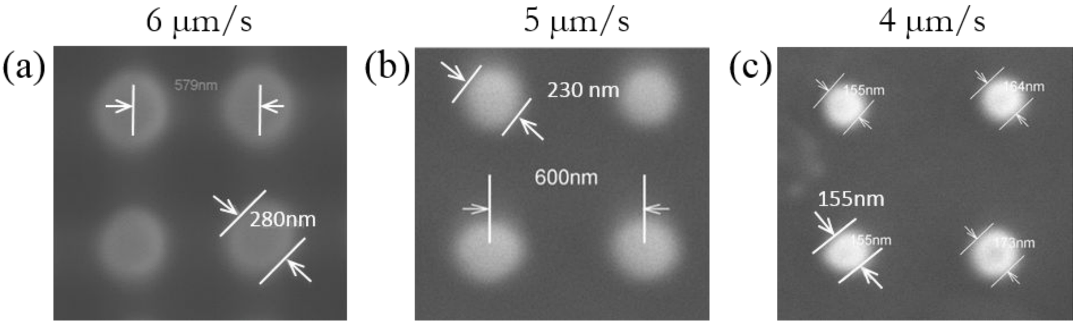

Figure 2.6: SEM images of 2D square structures with $\Lambda = 0.6$ μm fabricated by a laser power of 10 μW and a scanning speeds of 6 μm/s, 5 μm/s, and 4 μm/s, respectively. The size of polymeric cylinders are 280 nm, 250 nm, and 155 nm, respectively.

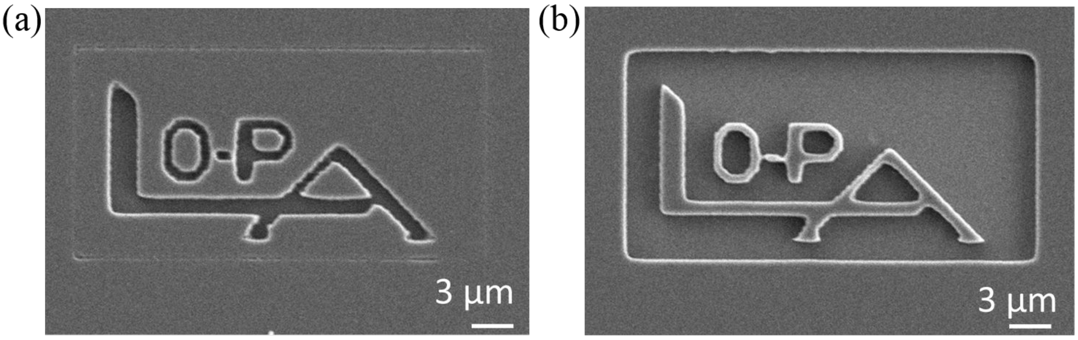

Figure 2.7: 2D arbitrary structures fabricated on S1805 photoresist by a laser power of 15 μW and a scanning speed of 10 μm/s. (a) Negative structure. (b) Positive structure.

ure 2.7(a) shows a SEM image of a negative structure of "LOPA" letter on S1805. The structure was exposed by moving the laser beam along the lines of the "LOPA" letter. In contrast, a positive structure of "LOPA" letter shown in figure 2.7(b) was obtained by exposing the whole area except the "LOPA" letter.

It was evident that this method allows the fabrication of many structures with submicrometer size. In the next part, we will apply this technique to fabricate desired photonic crystal structures.

2.4.2 Structuring of desired photonic crystals

Honeycomb lattices were fabricated by moving the laser beam following a triangular shape as shown in figure 2.8(a). Figures 2.8(b-e) show SEM images of 2D honeycomb

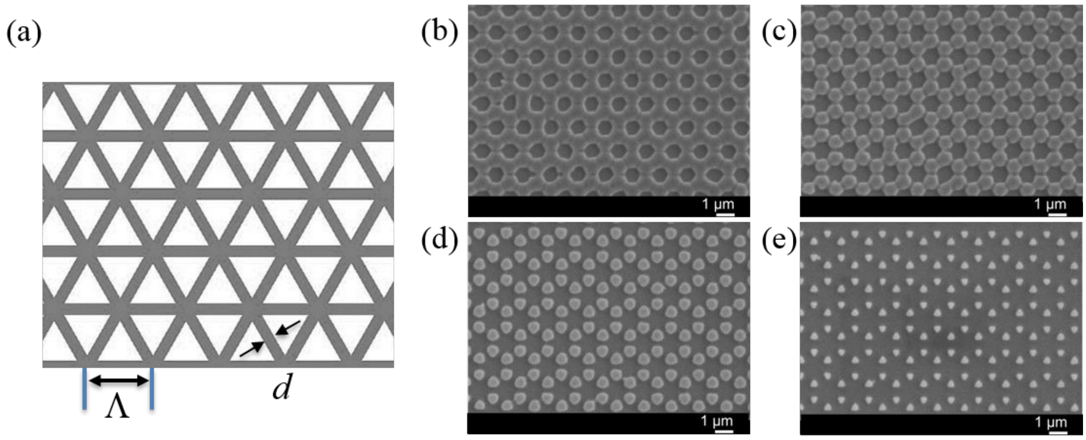

Figure 2.8: (a) The model of a honeycomb lattice created by moving the laser beam following a triangular shape, Λ is the period and d is track width. (b-e) SEM images of honeycomb lattices (period of $\Lambda = 1.5$ μm) fabricated with a laser power of 10 μW and an average scanning speed of 9 μm/s (b), 8 μm/s (c), 7 μm/s (d), 6 μm/s (e).

lattices with a period of $\Lambda = 1.5$ μm, fabricated by a constant laser power of 10 μW and with different scanning speeds of 9 μm/s, 8 μm/s, 7 μm/s, and 6 μm/s, respectively. At lower doses (ca. 9 μm/s and 8 μm/s) the adjacent cylinders were connected whereas at higher doses (ca. 7 μm/s and 6 μm/s), the cylinders were separated creating a track width (d, see figure 2.8(a)) of 250 nm and 500 nm, respectively (figures 2.8 (d-e)).

In a similar way, assembled multirings lattices were created by moving the laser beam following the circles arranged into a hexagonal lattice. Figures 2.9(b-e) show SEM images of 2D assembled multirings lattices with a period of 2 μm fabricated by a constant laser power of 9 μW and with different average scanning speeds of 10 μm/s, 9 μm/s, 8 μm/s, and 7 μm/s, respectively. We see that, by changing exposure doses, assembled multirings lattices were fabricated with different wall thicknesses: 150 nm (b), 200 nm (c), 300 nm (d), and 400 nm (e). These structures can be served as photonic crystals or can be converted into other materials by a combination with some techniques such as lift-off and etching. Comparing to negative photoresists, positive photoresists do not cross-link, and it is easy to be removed after transferring process. These fabricated 2D structures therefore can be used for numerous applications, such as diffractive gratings, color filters, as well as templates [36] for obtaining photonic crystals, plasmonic structures, etc.

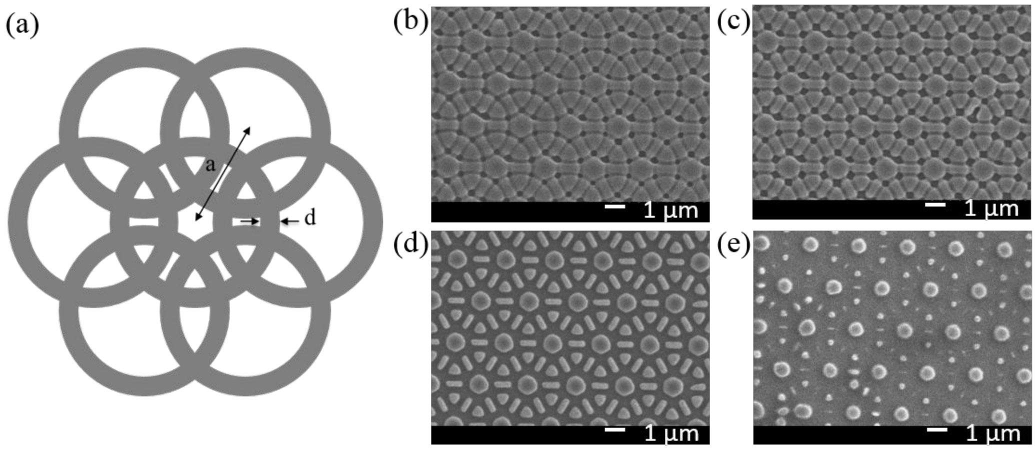

Figure 2.9: (a) Assembled multirings lattice created by an arrangement of multirings following a hexagonal configuration. d is wall thickness and a is lattice constant. (b-e) SEM images of assembled multirings lattices fabricated with $a = 2$ μm and $d =$ 150 nm (b), 200 nm (c), 300 nm (d), and 400 nm (e), respectively. These structures were written by a laser power of 10 μW and with different average scanning speeds of 9 μm/s, 8 μm/s, 7 μm/s, and 6 μm/s, respectively.

2.5 Bandgap calculations of fabricated 2D structures

2.5.1 Honeycomb photonic crystal structures

In previous part, we have demonstrated the fabrication of various kinds of 2D periodic and quasi periodic structures on a positive photoresist. These structures can be used as templates to transfer into higher dielectric constant materials by replication processes as shown in figure 1.3 of chapter 1. The question is "*can we directly use these fabricated polymeric structures as photonic crystal?*". Many structures of low dielectric constant have already been proposed to obtain partial PBGs (TE- or TM- polarized waves) by increasing the structure symmetry [37, 38]. Experimentally, a hexagonal lattice (six fold symmetry) opens a small gap while a square lattice (four fold symmetry) is not. We have calculated the PBG of honeycomb lattices that were shown in figure 2.8. Band structures of honeycomb lattices are calculated by using a 2D FDTD method for two cases: i) a honeycomb lattice consisting of polymeric cylinders ($n = 1.6$) in an air background and ii) another is inverse geometry (air holes in a polymeric background). Figures 2.10(a) and (b) illustrate a honeycomb lattice and corresponding 2D reciprocal space, where a is the lattice constant and r is the radius of the cylinders. For the first case, honeycomb

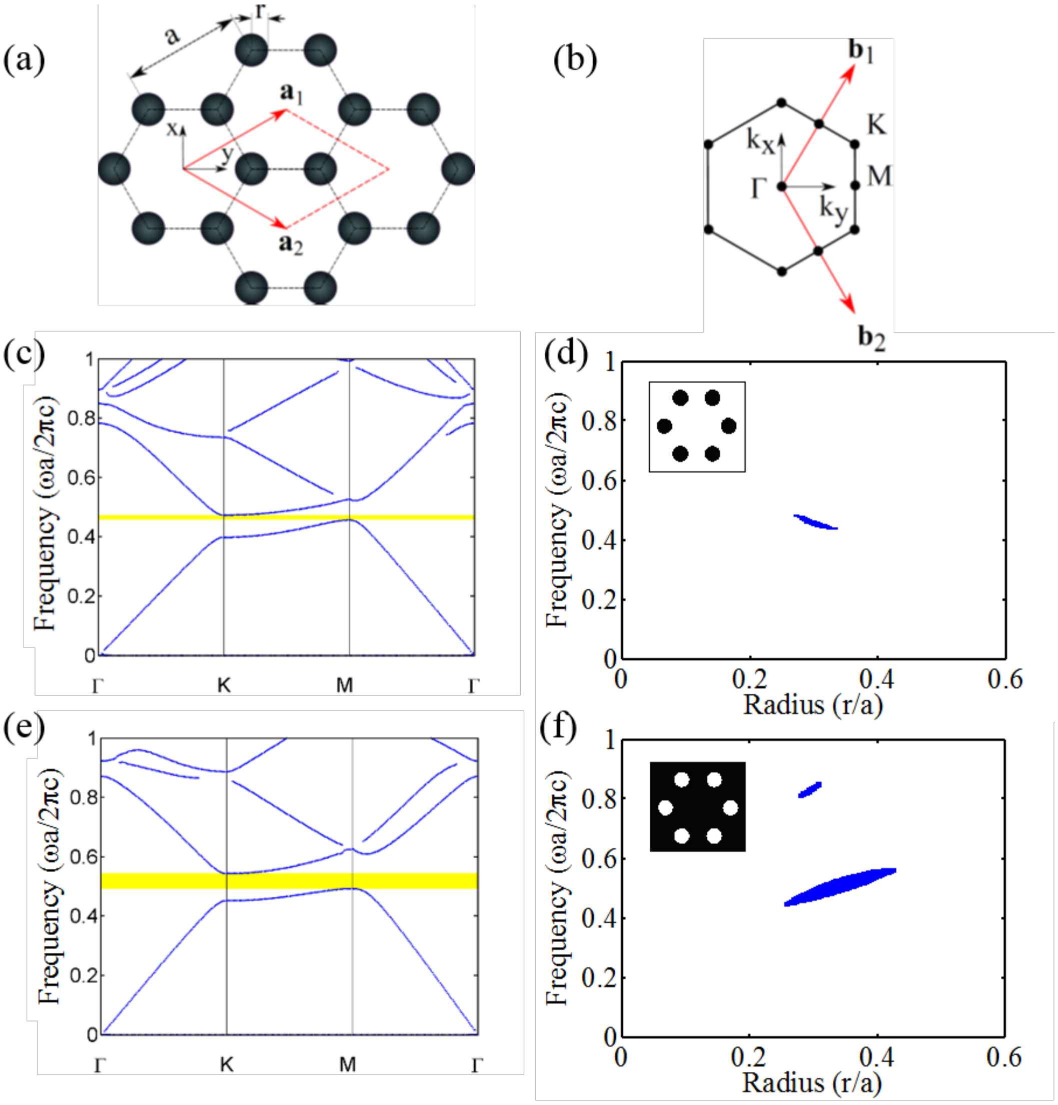

Figure 2.10: (a) 2D honeycomb lattice. $\mathbf{a}_1 = a/2\left(\sqrt{3},1\right)$ and $\mathbf{a}_2 = a/2\left(\sqrt{3},-1\right)$ are the principle lattice vectors, r is the cylinder radius. (b) Corresponding 2D reciprocal space of the honeycomb lattice. $\mathbf{b}_1 = 2\pi/a\left(1/3\sqrt{3},1/3\right)$ and $\mathbf{b}_2 = 2\pi/a\left(1/3\sqrt{3},-1/3\right)$ are the primitive vectors of the reciprocal lattice. The reduced first Brillouin zone is identified by K, M, Γ points. (c) Photonic band structure of a 2D honeycomb lattice of polymeric cylinders in an air background for TE mode at radius $r/a = 0.3$. (d) Gap map of TE mode (shaded blue region) of a 2D honeycomb lattice made by polymeric cylinders in an air background as a function of r/a. (e) Photonic band structure of a 2D honeycomb lattice of air holes in a polymeric background for TM mode at radius $r/a = 0.35$. (f) Gap map of TM mode (shaded blue region) of a 2D honeycomb lattice of air holes in a polymeric background as a function of r/a.

Table 2.1: Summary of PBG of polymeric honeycomb lattices.

Polarization mode	Honeycomb types	Existence of PBG?	Largest PBG ($\omega a/2\pi c$)
TM	Air-holes	Yes	0.05
	Polymeric cylinders	No	NA
TE	Air-holes	No	NA
	Polymeric cylinders	Yes	0.02

lattice consisting of polymeric cylinders ($n = 1.6$) in the air background, the PBG exists only for TE mode. Figure 2.10(c) shows the band structures for TE mode at radius $r/a = 0.3$. A map of complete bandgap (shaded blue region) as a function of r/a for TE mode is shown in figure 2.10(d). The largest PBG is $a\Delta\omega/2\pi\mathrm{c} = 0.02$ at $r = 0.3a$. In contrast, for the second case, honeycomb lattice consisting of air holes ($n = 1$) in the polymeric background, the PBG exists only for TM mode. Figure 2.10(e) shows the band structures for TM mode at radius $r/a = 0.35$. A map of complete bandgap (shaded blue region) as a function of r/a for TM mode is shown in figure 2.10(f). The largest PBG is $a\Delta\omega/2\pi\mathrm{c} = 0.05$ at $r = 0.35a$. All results are summary in Table 2.1. It shows that a honeycomb lattice of air holes in a polymeric background gives the best PBG for TM mode. For example, by fabricating 2D honeycomb lattices with different lattice constants, we can change the PBG from visible to infrared range. If we assume that the lattice constant is 2 μm, that is easily fabricated by our method, the honeycomb lattice will inhibit all light wavelengths in the range of 3.8-4.2 μm for the best case.

2.5.2 Assembled multirings photonic crystals

As mentioned above, the PBG width can be improved by increasing the structure symmetry [37]. We proposed a new kind of structure by assembly multirings into a hexagonal lattice. This structure has been demonstrated experimentally and shown in figure 2.9. Figure 2.11(a) illustrates an assembled multirings lattice and the corresponding reciprocal space, where a is lattice constant, r is the radius of the rings, and d is the width of wall-rings. The PBG was also calculated for two cases: one is multirings of air ($n = 1$) in the polymeric background and the another is inverse geometry (multiring of polymer in the air background). According to experimental results, the wall-rings thickness is fixed at 300 nm for both cases. For the first case, multirings lattice consisting of polymeric

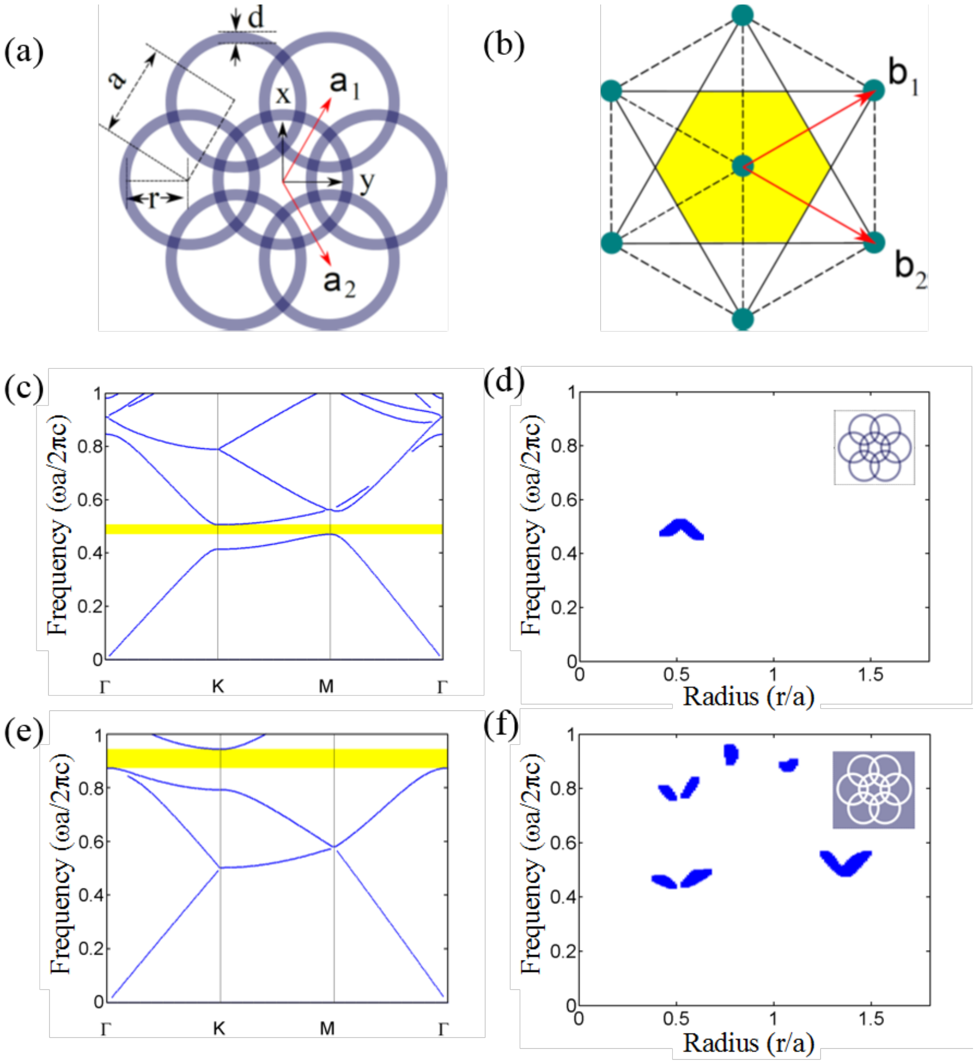

Figure 2.11: (a) 2D assembled multirings lattice. $\mathbf{a}_1 = a\left(1/2, \sqrt{3}/2\right)$ and $\mathbf{a}_2 = a\left(1/2, -\sqrt{3}/2\right)$ are the principle lattice vectors, r is the radius of rings, d is the width of ring-walls, a is the lattice constant. (b) Corresponding 2D reciprocal space of the hexagonal lattice. $\mathbf{b}_1 = 2\pi/a\left(1, 1/\sqrt{3}\right)$ and $\mathbf{b}_2 = 2\pi/a\left(1, -1/\sqrt{3}\right)$ are the primitive vectors of the reciprocal lattice. The reduced first Brillouin zone is a hexagon centered around the origin. (c) PBG of assembled multirings lattice, $r/a = 0.51$, $a = 1.5\ \mu$m, ring-wall thickness $d = 300$ nm; refractive index $n = 1.6$. (d) PBG map for TE mode of the lattice containing polymer-rings in a air background, ring-wall thickness $d = 300$ nm; $a = 1.5\ \mu$m, (e) The PBG of assembled multirings lattice, $r/a = 0.78$, $a = 1.5\ \mu$m, ring-wall thickness $d = 300$ nm; refractive index $n = 1.6$. (f) Map of PBG for TM mode of lattice containning air-rings in the polymer background, ring wall thickness $d = 300$ nm; $a = 1.5\ \mu$m.

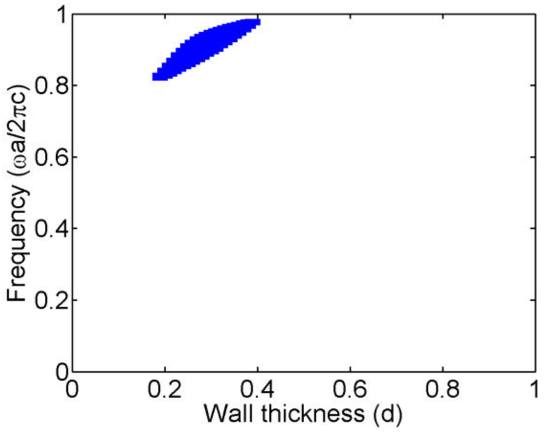

Figure 2.12: A map of PBG as a function of the ring-wall thickness for TM mode of the lattices containing air-rings in a polymeric background $r = 1.18$ μm, $a = 1.5$ μm; refractive index $n = 1.6$.

Table 2.2: Summary of PBG for polymeric assembled multirings lattices. In this case d is assumed to be 300 nm.

Polarization mode	Assembled microrings	Existence of PBG?	Largest PBG ($\omega a/2\pi c$)
TM	Air	Yes	0.089
	Polymer	No	NA
TE	Air	No	NA
	Polymer	Yes	0.035

rings ($n = 1.6$) in the air background, the PBG exists only for TE mode. Figure 2.11(c) shows a photonic band structure of a 2D assembled multirings lattice of polymeric cylinders in an air background for TE mode at radius $r/a = 0.51$, and $a = 1.5$ μm. A gap map (shaded blue region) as a function of r/a for TE mode is shown in figure 2.11(d). The largest PBG is $a\Delta\omega/2\pi\text{c} = 0.035$ at $r = 0.51a$. For the second case, multirings lattice consisting of air rings ($n = 1$) in the polymeric background, the PBG exists only for TM mode. Figure 2.11(e) shows the band structure for TM mode at radius $r/a = 0.78$, and $a = 1.5$ μm. A gap map (shaded blue region) as a function of r/a for TM mode is shown in figure 2.11(f). The largest PBG is $a\Delta\omega/2\pi\text{c} = 0.089$ at $r = 0.78a$. All results are summarized in Table 2.2.

Furthermore, PBGs of assembled multirings lattices were optimized for the ring-wall thickness. By fixing the radius of rings, $r = 1.18$ μm, and the lattice constant,

$a = 1.5$ μm, a gap map for TM mode of the lattice containing air-rings in a polymer background is calculated and shown in figure 2.12. It confirmed again that the largest PBG is $a\Delta\omega/2\pi c = 0.089$, obtained with $d = 300$ nm.

Therefore, an assembled-multirings lattices of air rings in a polymeric background gives the best PBG with TM mode. As compared with honeycomb lattices, assembled multirings lattices give lager PBGs. If we assume a lattice constant of 1.5 μm, the lattice will inhibit all wavelengths of light in the range of 1.55-1.66 μm. Such structures are potential for applications in telecommunication domain. Note that due to the optical diffraction limit, our fabricated structures have a limitation of lattice constants at 1.5 μm.

Conclusion of chapter 2

In summary, we have developed a simple but efficient way, based on one-photon absorption direct laser writing technique, to fabricate 2D structures with controllable form on a positive photoresist. The structures from negative (air-holes) to positive (polymeric cylinders) forms are demonstrated theoretically and experimentally by using a confocal laser scanning setup employing a low power continuous-wave laser at $\lambda = 532$ nm and an objective lens with NA = 0.9. Many kinds of lattices such as hexagonal, honeycomb and assembled multirings were fabricated and their PBGs were theoretically calculated for low refractive index ($n = 1.6$) using the FDTD method. The simulation results show that TM band gaps exist in lattices of air holes in polymeric background (honeycomb lattices) or in lattices of air-rings in a polymeric background (assembled multirings lattices). In contrast, TE band gaps exist only in lattices of polymeric cylinders in an air background (honeycomb lattice) or in lattices of polymeric rings in an air background (assembled multirings lattices). As compared with honeycomb lattices, assembled multirings structures have larger PBGs. Fabricated structures can be also used as templates for producing PCs of higher refractive index materials or plasmonic structures of metal materials by using replication processes shown in figure 1.3 of chapter 1.

In the next chapters, we will focus on improving the resolution (feature size) of this fabrication method, and also study the use of fabricated structures as templates for fabrication of plasmonic structures.

Chapter 3

Direct laser writing of polymeric nanostructures via optically induced local thermal effect

3.1 Introduction

Direct laser writing (DLW) based on focusing a light beam through a high numerical aperture objective lens (NA OL) is an ultimate approach for 3D fabrication. However, the resolution of a common DLW technique is limited at hundreds nanometers due to the diffraction limit effect at the focusing spot of the OL [39]. Recently, several researchers have attempted to decrease the size of structures realized by DLW method by, for example, using a laser source with a shorter wavelength [26] or a quencher [40], or applying a stimulated emission depletion method [41,42]. Nevertheless, these improvements require complicated set ups and some resists with particular properties. Therefore, a simple and low cost method allowing to achieve high resolution of arbitrary structures is a high demand.

When materials are excited by light, there are two processes, namely photochemical (photolytic) and photothermal (pyrolytic) process, generated by absorption effect [43]. Photothermal process happens when the laser-induced excitation rate is low in comparison to the thermalization rate. In most case, the absorbed laser energy is directly transformed into heat and the material response can be treated in a purely thermal way. In polymers, thermalization time is on the order of 10^{-6}s [44]. In contrast, photochemical process occurs when the laser induced excitation rate is high in comparison to the thermalization rate. In this case, the excitations can build up in the intermediary states and the excitation energy can be sufficient to directly break bonds (photo-decomposition). During the photochemical processing, the temperature of materials is almost unchanged. Hence, using a continuous-wave (cw) laser is appropriate for the photothermal processing in polymer materials instead of using a femto-second laser.

Thanks to the use of the OL having a high NA, strong absorption energy at the focusing spot can modulate the surface or control the phase of materials through thermal effect [45]. Since the laser can be precisely controlled, dimensionally as well as directionally, it is useful to locally heat a specific area. With polymer materials, glass transition occurs at T_g, and crosslinking reactions are activated from a temperature threshold that changes the chemical properties of materials [46–48]. This feature can be exploited as a positive effect for fabrication of polymeric structures.

In this chapter, we demonstrate a simple and low-cost method allowing fabrication of desired polymeric structures with feature sizes well below the diffraction limit by use of the thermal effect in a positive photoresist. A continuous-wave (cw) laser beam is employed to optically induce a local thermal effect that enables the formation of solid polymeric "positive" nanostructures, similar to those obtained by negative photoresists. The chapter is organized as follows: the thermal behaviour of the S1805 positive photoresist for a wide range of temperatures is presented in section 2; sample preparation and fabrication processes are shown in section 3; a simple heat model is introduced in section 4 to explain the mechanism of the the photothermal effect; the fabrication of 1D, 2D and 3D structures on a positive photoresist is presented in section 5; and some discussions and conclusion are summarized in the last section.

3.2 Thermal behavior of S1805 positive photoresist

The thermal behavior of polymers is important in the selection of proper processing and fabrication conditions, the characterization of the physical and mechanical properties of a material, and hence the determination of appropriate end uses. In polymers, intramolecular bonds are due to primary valence bonds (covalent) while the intermolecular attractions usually are due to secondary bonding forces. The intermolecular forces are opposed by thermal agitation, which induces vibration, rotation, and translation of a molecular system. The polymer deformations are related to the rotation and vibration of the molecular chains. Above a certain temperature, the deformation is strong enough leading to crosslinking reaction of molecular chains [47]. The thermal behavior of S1805

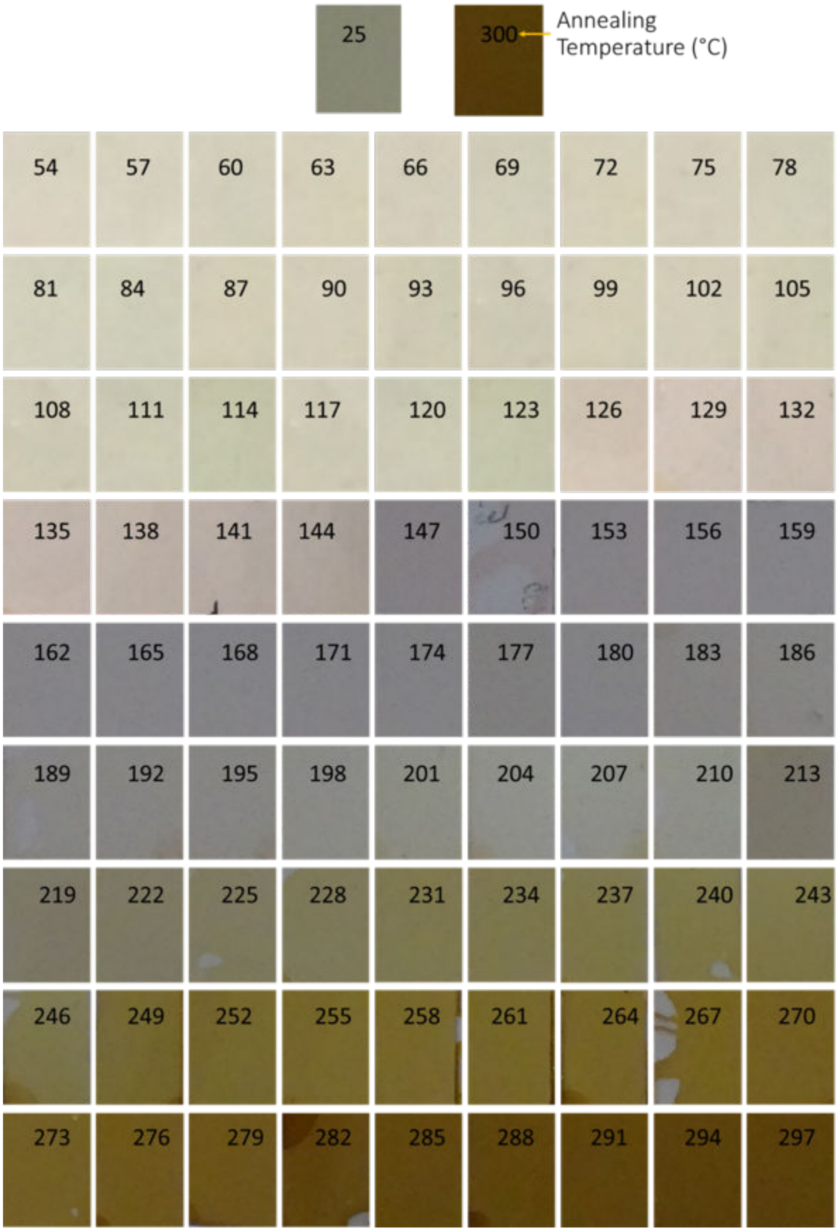

Figure 3.1: Images of S1805 films (thickness of 600 nm) coated on glass substrates and annealed at different temperatures (25-300°C) for 5 minutes.

positive photoresist was investigated for a large range of temperature, from 25 to 500°C. We experimentally studied this temperature mark as well as the absorbance properties of annealed S1805 thin films. Different samples of S1805 coated on glass substrates were annealed on a hot plate for 5 minutes. Figure 3.1 shows some images of polymer films annealed at different temperatures. They were then immersed in acetone to check the

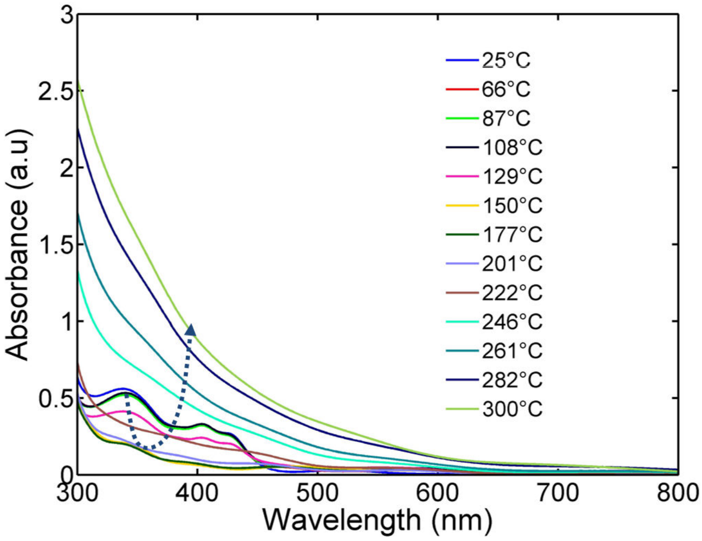

Figure 3.2: The absorbance spectra of the S1805 films annealed at different temperatures (25-500°C) for 5 minutes. The dot arrow indicates the variation of absorption spectra as a function of annealing temperature.

solubility. Another set of samples, annealed by the same parameters, was used to measure the absorption spectra. Absorbance spectra of these films are shown in figure 3.2. We experimentally found that the photoresist thin films annealed below 156°C ± 3°C were completely washed out, whilst those annealed above 156°C ± 3°C were hardened and insoluble in acetone. Therefore, it can be concluded that the crosslinking activation and glass transition temperatures of the S1805 positive photoresist are approximately in the range of 156°C. Furthermore, we observed a color change of these annealed samples as a function of the annealing temperature, indicating a significant change of the absorption of annealed photoresist. Namely, the absorption first decreases with temperature, then increases at a high annealing temperature as illustrated by a dot-arrow shown in figure 3.2. The absorption band was also extended to the visible range. The change of optical properties of positive photoresists can be explained as follow: at low temperatures (below 145°C) chain segments are frozen in fixed positions, atoms undergo only with low-amplitude vibratory motion. When the samples are annealed at high temperature, the amplitude of atomic vibrations becomes larger, hence, leading to a rotation and translation of the molecular systems. Consequently, the polymer chains are re-arranged, resulting in a change of the chemical structures and a variation of their absorbance spectra [48]. Figure 3.3 particularly exhibits the absorption coefficient of the S1805 photoresist at $\lambda = 532$ nm, the wavelength of the DLW system, as a function of annealed

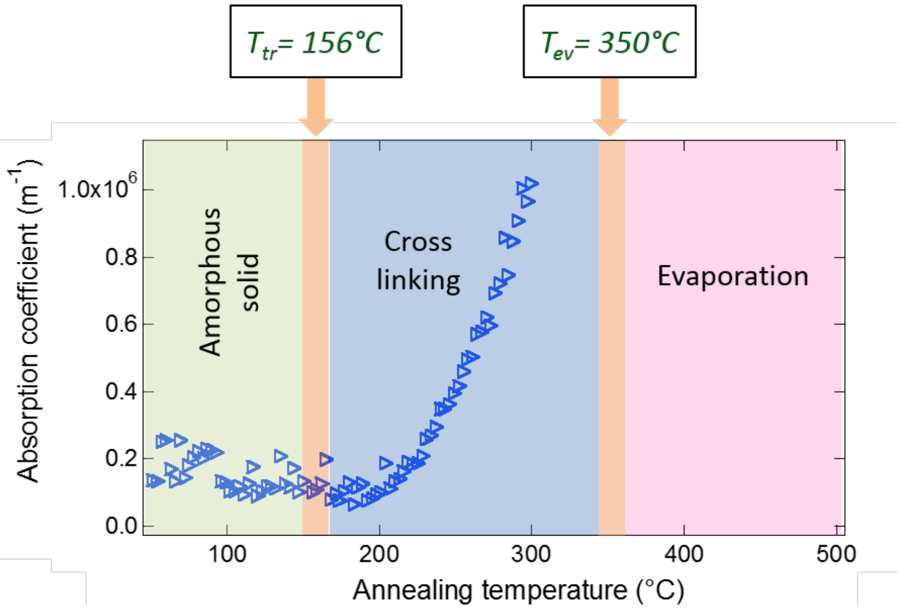

Figure 3.3: Absorption coefficient of the S1805 sample measured at λ = 532 nm as a function of annealing temperatures.

temperatures. At this wavelength, the absorption coefficient is almost unchanged in the 50°C – 200°C range, but it is dramatically increased when the annealing temperature is over 200°C. The rotation and translation of chain segments trigger important mechanisms for the energy absorption. This accounts for the change of physical and mechanical properties of S1805 photoresist. Note that because the hot plate in our experiment is limited at a maximum temperature of 300°C, different samples of S1805 coated glass substrates were then annealed at a temperature in the range from 300°C to 500°C (accuracy ± 5°C) using a Nabertherm oven. The results showed that S1805 photoresist was quickly evaporated at a temperature of about 350°C as indicated in figure 3.3. In the next part, instead of using a hot plate, we will demonstrate the use a focusing laser beam at 532 nm to locally heat up S1805 photoresist through which we can fabricate polymeric nanostructures.

3.3 Sample preparation and fabrication process

A schema of the DLW setup is introduced in figure 2.2 of chapter 2. To induce efficiently the thermal effect, we have used a cw green laser beam (λ = 532 nm) and a high NA (NA = 1.3, oil-immersion) OL. The sample was translated in 3D space following a controllable trajectory by a high-resolution piezo translation (PZT) stage. The structures

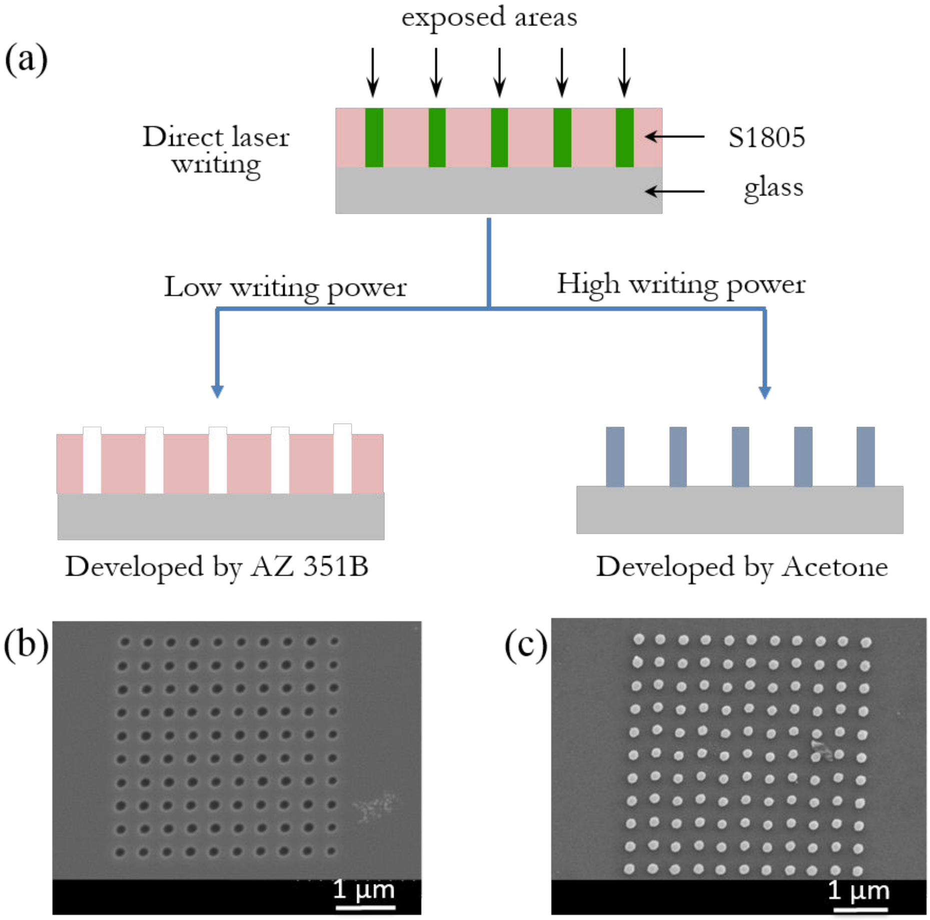

Figure 3.4: (a) Fabrication processes of nanostructures on a positive photoresist. (b) SEM image of a structure written at low power ($\sim \mu$W) and developed by AZ 351B. (c) SEM image of a structure written at high power ($\sim$ mW) and developed by acetone.

were fabricated at different powers (from 1 μW to 10 mW) and for different exposure times (from 0 ms to 1000 ms) or with different scanning speeds, from 5 to 40 μm.s^{-1}. Positive photoresists were first spin-coated on pre-treated glass substrates and then soft-baked on a hot plate at 115°C for two minutes. Samples were protected in a black box before light exposure. The absorption coefficient of S1805 at 532 nm-wavelength was experimentally measured to be approximately $1.2{\times}10^5$ m^{-1}. By manipulating the exposure intensities and choosing appropriate developers, we are able to resolve desired "positive" structures as shown in figure 3.4(a). Actually, under low writing intensity (microwatt exposure power), S1805 becomes soluble in AZ 351B developer and behaves like a conventional positive photoresist, as demonstrated in previous chapter. Whereas at high writing intensity (milliwatt exposure power), the induced temperature at a localized illuminating spot becomes important. Above glass-transition temperature, it activates the crosslinking process of the positive photoresist [49, 50]. The material becomes hardened and undissolved in AZ 351B developer or even in acetone. In this case, a positive photoresist can be regarded as a negative photoresist and considered as an image reversal material. Examples of 2D structures realized at low writing intensity and at high writing intensity are shown in figures 3.4(b-c).

The "negatively" acting of the positive photoresist is initiated by crosslinking and the glass transition process, which are triggered by an intense continuous laser exposure. Although this effect has been studied, it still exists some ambiguous understandings [46–48]. The crosslinking can be induced by chemical reactions or thermal activation from an identified temperature. Likewise, the glass transition occurs when the polymer temperature reaches the glass transition temperature (T_g), which is regarded as a satisfaction of the required activation energy for chain segment motions.

3.4 Theoretical model of optically induced local thermal effect

The above investigation suggests that, in LOPA-based DLW process, the intense light intensity at the focusing spot induces a hot spot with a temperature larger than 156°C, which then locally solidifies the S1805 photoresist. We therefore investigated a laser heating model to understand the thermal response of a positive photoresist under a tight focusing spot. When a laser beam propagates through an absorbing material, the temperature distribution in the material can be derived from the equation of heat [51]:

$$\rho C_p \frac{\partial T}{\partial t} = k\nabla^2 T + S, \tag{3.1}$$

where ρ is the mass density (kg.m^{-3}), C_p is the heat capacity (J.kg^{-1}.K^{-1}), k is the thermal conductivity (W.m^{-1}.K^{-1}), and the S(W.m^{-3}) term is calculated as a variation of light intensity along the propagation direction:

$$S = -\left(\frac{\partial I(r,z)}{\partial z}\right)_r = \mu_{\text{abs}}(1-R_c)I(r,z)\exp(-\mu_{\text{abs}}z), \tag{3.2}$$

where $I(r,z)$ is the laser intensity, μ_{abs} is the absorption coefficient of the material, and R_c is reflection coefficient. In our case, the light beam is focused into photoresist by a

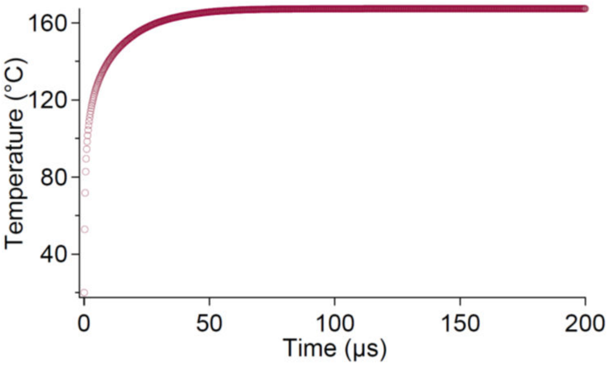

Figure 3.5: Theoretical calculation of the evolution of optically induced temperature as a function of exposure time. The laser on at t = 0 μs. The simulations were realized with following parameters: $\rho = 1200$ kg.m^{-3}, $C_p = 1500$ J.kg^{-1}.K^{-1}, $k = 0.2$ W.m^{-1}.K^{-1}, $R_c = 0$, $\mu_{\text{abs}} = 1.2 \times 10^5$ m^{-1}, $S \approx 10^{15} I_{\text{OPA}}$ W.m^{-3} corresponding to a laser power of 0.5 mW, and initial temperature of material is 20°C.

high NA OL. The intensity distribution of the focused laser beam is calculated by:

$$I(r,z) = I(0,0) I_{\text{OPA}}, \tag{3.3}$$

where r is the radial distance from the beam axis, z is the axial distance from the center of the focusing spot, $I(0{,}0)$ is the peak intensity at the center of focusing spot ($r = 0$, $z = 0$) and I_{OPA} is the normalized intensity distribution of focused light in the focal region, which is rigorously calculated by using the vector Debye method [35]. Due to the absorption of the photoresist and thanks to the optical intensity distribution (see figure 3.6(a)), a temperature distribution is produced at the focusing region (see figure 3.6(b)). By using finite element method with MATLAB PDE solver, equation (3.1) was numerically solved to characterize the optically induced heat profile. We note that, using a femtosecond laser, the induced temperature increases quickly to one million degrees but also decreases quickly to room temperature [52] (the heating time is the same as the femtosecond pulse duration), which is not suitable to solidify the positive photoresist. In our DLW method employing a cw laser, we found theoretically that the induced temperature at the focusing spot rises up quickly as a function of exposure time and reaches a stable temperature (beyond 100°C) after several 10 μs, depending on the exposure power (see figure 3.5). This time scale is consistent with previous heat models on other polymer materials [43]. The optical intensity distribution and corresponding induced temperature profile, obtained after 50 μs of exposure, are shown in figure 3.6. It

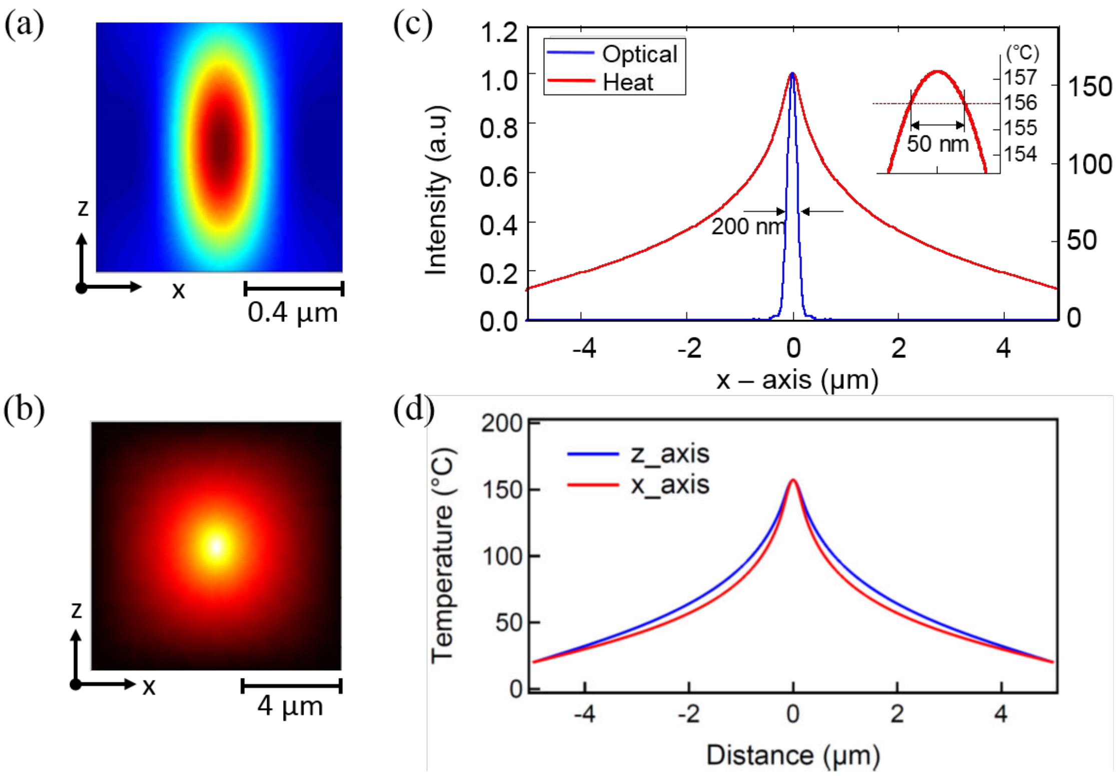

Figure 3.6: (a) Theoretical calculation of light intensity distribution at the focal region of a high NA OL for xz–plane. (b) Corresponding heat distribution inside excited material for xz–plane. (c) Cross section of heat profile and light intensity distribution at the focal region for x–axis. (d) The cross section of heat distribution along x-axis and z- axis. The simulations were realized with following parameters: $\rho = 1200$ kg.m^{-3}, $C_p = 1500$ J.kg^{-1}.K^{-1}, $k = 0.2$ W.m^{-1}.K^{-1}, $R_c = 0$, $\mu_{\text{abs}} = 1.2 \times 10^5$ m^{-1}, $S \approx 10^{15} I_{\text{OPA}}$ W.m^{-3} corresponding to a laser power of 0.5 mW, and initial temperature of material is 20°C.

can be seen that the normalized heat distribution is broader than the optical intensity distribution. However, there is only a tiny area where local temperature can surpass the crosslinking/glass transition temperature threshold (see inset of figure 3.6(c)). The size of this area is even smaller than the full-width at half maximum of the optical focusing spot, suggesting that a solidified structure made by optically induced thermal effect could be smaller than the diffraction limit, which usually limits the resolution of DLW technique.

The resolution of DLW along the propagating direction of the laser beam ($z-$dimension) plays an important role in 3D fabrication. Figure 3.6 shows theoretical calculations of light intensity distribution (figure 3.6(a)) at the focal region of a high NA OL for $xz-$plane and corresponding heat distribution inside excited material (figure 3.6(b)).

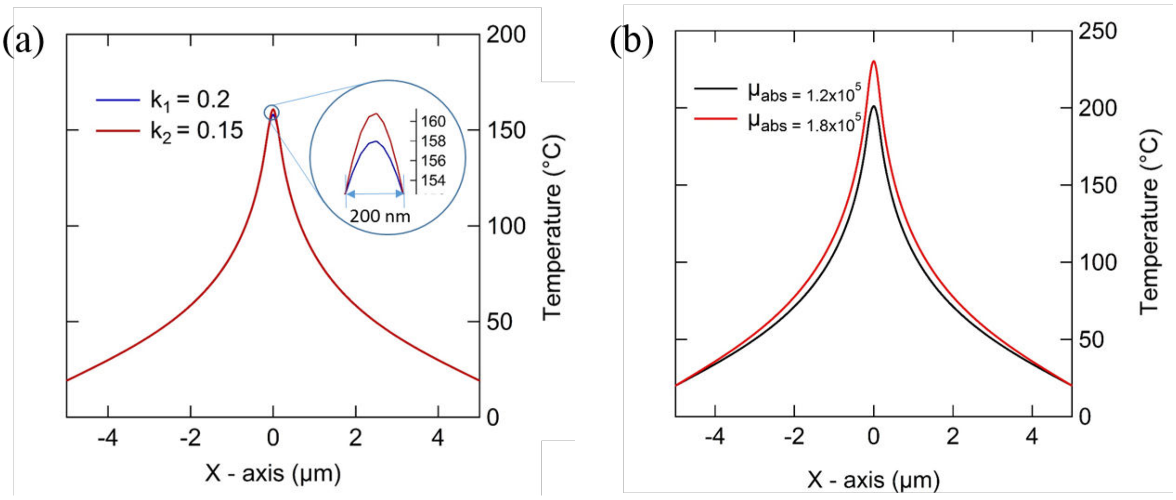

Figure 3.7: (a) Comparison of temperature distributions obtained in two possible cases: i) thermal conductivity is 0.2 for whole film (blue), and ii) thermal conductivity is 0.15 at focusing center with a diameter of 200 nm and 0.2 on the remained part (red). The simulations were realized for only x-axis with following parameters: ($\rho =$ 1200 kg.m^{-3}, $C_p = 1500$J.kg^{-1}.K^{-1}, $\mu_{\text{abs}} = 1.2\times10^5$ m^{-1}, the laser power of 0.5 mW. (b) Comparison of temperature distributions in two cases: i) absorption coefficient is constant ($\mu_{\text{abs}} = 1.2\times10^5$ m^{-1}) for whole region (black), and ii) absorption coefficient at focusing center with a diameter of 100 nm is $\mu_{abs} = 1.8\times10^5$ m^{-1} and that of the remain part is $\mu_{\text{abs}} = 1.2\times10^5$ m^{-1} (red).

We see that the longitudinal ($z-$axis) size of the focusing spot is about 2.5 times larger than the transverse size ($x-$axis), whereas the temperature distribution along the longitudinal direction ($z-$axis) is quite similar to that of transverse direction ($x-$axis, or $y-$axis) as described in figure 3.6(d). It means that the fabrication based on optically induced thermal effect could have an isotropic resolution for 3D structures.

We note that the induced temperature is very sensitive to exposure dose. Indeed, when a small area of material is strongly excited, the temporal thermal balance is immediately broken due to the change of thermal constants. We also analysed thermal profiles for many different values of thermal constants, assuming that we excite a small area of 200 nm-diameter to reach a temperature above 150°C. The thermal conductivity of the excited part will be reduced from 0.2 to 0.15. The simulation results show that the thermal profile will increase slightly and become sharper as shown in figure 3.7(a). Furthermore, we found theoretically that the absorption coefficient (μ_{abs}) is also an essential parameter to define the transfer the radiant energy rate from the DLW spot to the absorbing medium. Therefore, a minor modification of μ_{abs} can lead to a significant

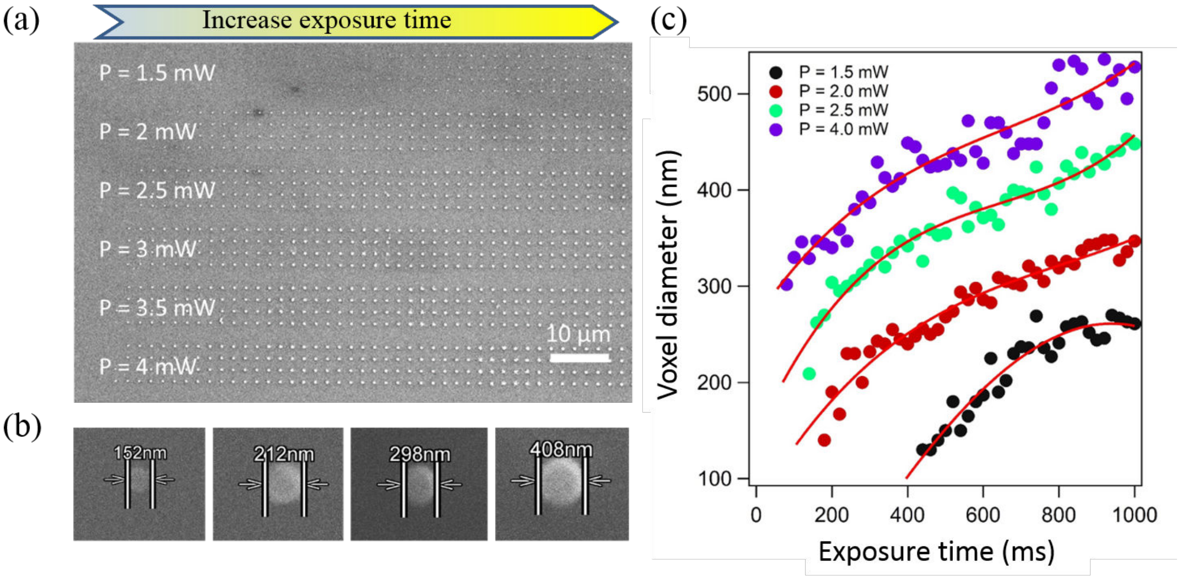

Figure 3.8: (a) SEM images of voxels fabricated on S1805 positive photoresist by DLW technique with different laser powers and different exposure times. (b) Voxels fabricated by an exposure time of 450 ms and different laser powers of 1.5 mW, 2mW, 2.5 mW, and 4 mW, respectively. (c) Dependence of the diameters of the voxels on exposure times and laser powers. Dots are experimental data, and continuous curves are fitting results.

alteration of the thermal response, *i. e.* induced temperature, as shown in figure 3.7(b). However, the absorption coefficient at the writing wavelength ($\lambda = 532$ nm) does not significantly change for temperature range of 50°C–200°C (see figure 3.3). Therefore, by limiting the laser power or exposure time to keep the induced temperature in this range, the absorption coefficient is constant. Only, if we extend the exposure process, the temperature at the focusing spot will progressively increase and the cross-linked area will be expanded accordingly. Once the temperature reaches 200°C, the absorption coefficient jumps up rapidly (see figure 3.3), leading to a great boost of induced temperature.

3.5 Fabrication of sub-wavelength multidimensional structures on positive photoresists

3.5.1 Dependence of structure size on exposure time and power

Experimentally, we have fabricated voxels by exposing a tiny volume of material with different powers and exposure times. Figure 3.8(a) shows SEM images of voxels fabricated

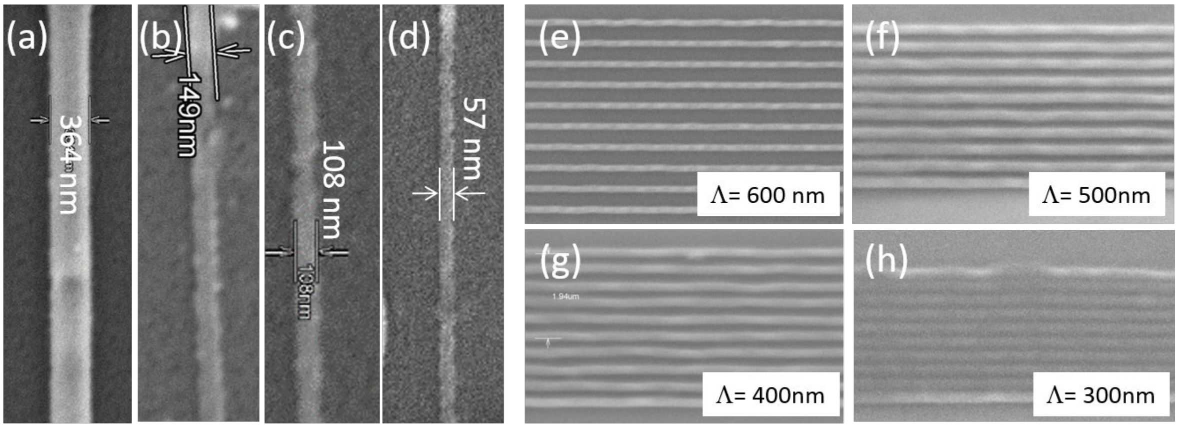

Figure 3.9: (a-d) SEM images of 1D line structures fabricated by different laser powers: 4, 3, 2.5, and 2 (mW). The scanning velocity is fixed at 10 μm/s. (e-h) SEM images of 1D structures with different periods of 0.6 μm, 0.5 μm, 0.4 μm, and 0.3 μm, respectively. The exposure power is kept at 2 mW and the scanning velocity is fixed at 5 μm/s. These structures were fabricated with S1805 (thickness = 600 nm).

using different laser powers of 1.5 mW, 2 mW, 2.5 mW, 3 mW, 3.5 mW, and 4 mW, respectively. The S1805 resist film was exposed one by one with an exposure time varying from 20 ms to 1000 ms. Figure 3.8(b) shows the voxels with a feature size of 152 nm, 212 nm, 298 nm, 408 nm, which were obtained by an exposure time of 450 ms and with laser powers of 1.5 mW, 2 mW, 2.5 mW and 4 mW, respectively. The feature sizes of voxels as a function of exposure time for different powers are shown in figure 3.8(c). We see that the size of voxels increases with the exposure time and laser power. This increment comes from the growth up of crosslinking reaction due to the induced temperature. Obviously, we can control precisely the laser power and the exposure time to obtain desired structures, with a feature size as small as 100 nm.

3.5.2 Realization of 1D and 2D arbitrary structures

Nanowires are fabricated by scanning the focusing spot along $x-$ or $y-$direction. Figures 3.9(a-d) show nanowires with the feature sizes of 364 nm, 149 nm, 108 nm, and 57 nm fabricated at a scanning velocity of 10 μm/s and laser powers of 4 mW, 3 mW, 2.5 mW, and 2 mW, respectively. With optimized laser power and writing speed, a nanowire with a feature size down to 57 nm is thus obtained, equivalent to a resolution of $\lambda/9$, much smaller than the diffraction limit, as shown in figure 3.9(d). We also studied the effect of periodicity on the quality of fabricated structures. Figures 3.9(e-h) show 1D structures (line gratings) fabricated by a laser power of 2 mW and a velocity of 5 μm/s. We see that

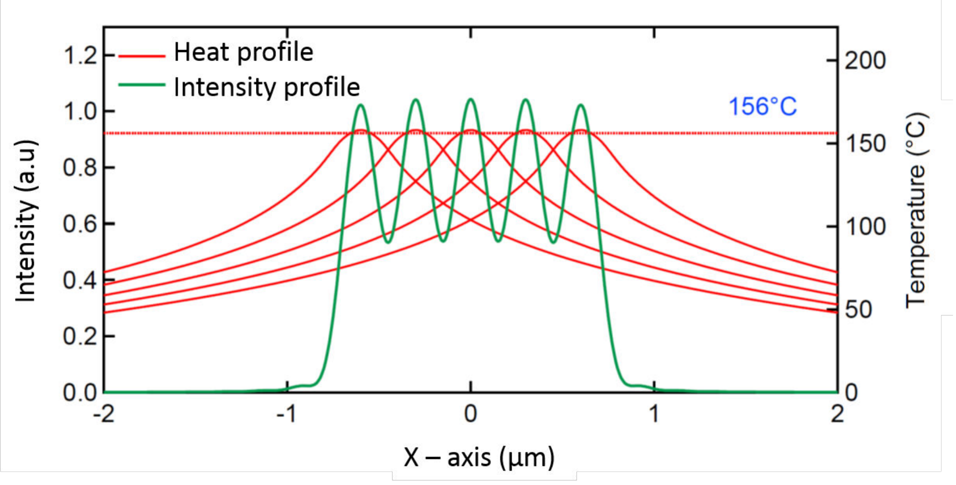

Figure 3.10: (a) The light intensity profile of multiple exposures on resist (green curve) and the corresponding temperature profiles on resist (red curves). The distance between two adjacent exposures is 300 nm.

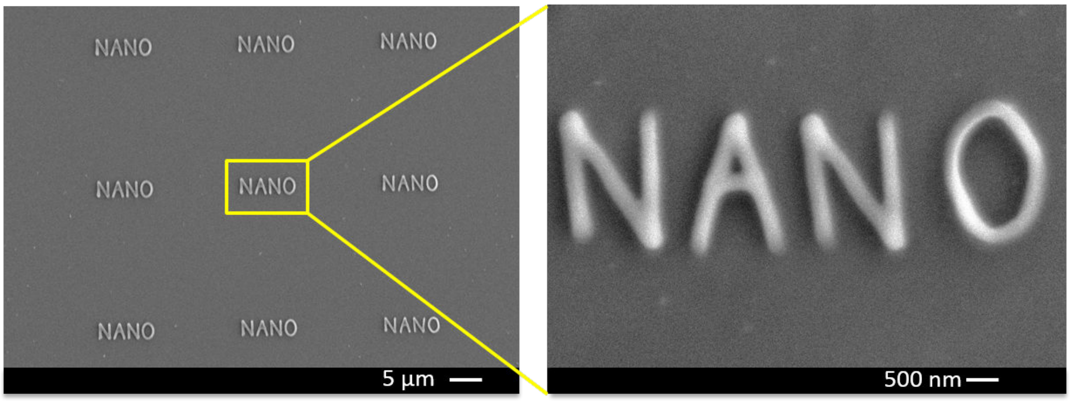

Figure 3.11: A pattern of NANO letter was fabricated by 2 mW and by an average writing speed of 10 μm/s.

lines are very smooth and uniform, and linewidth slightly changes from 200 nm to 230 nm when the period decreases from 600 nm to 300 nm. It is interesting to emphasize that, even with the DLW involved with OPA mechanism, no accumulation effect was observed (structures are uniform even with a very short lattice constant) because there exists a temperature threshold above it the positive photoresist becomes solid. Solidification of structure resulting from photothermal process differs from that of photochemical process in term of accumulation. Furthermore, the induced temperature is not only localized but also temporal, *i. e.*, during the exposure time only. Figure 3.10 shows the integrated light intensity profile resulting from multiple exposures at a 300 nm period (green curve)

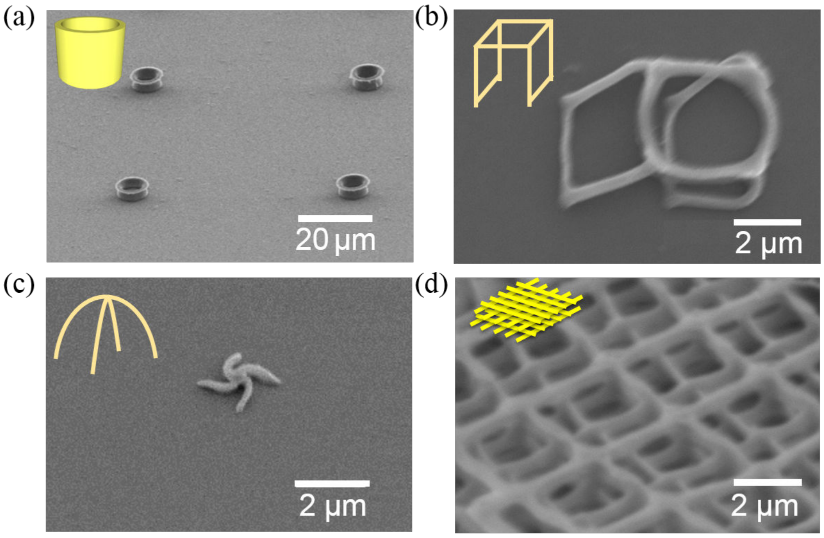

Figure 3.12: SEM images of different 3D structures fabricated by 6 mW in S1818 (thickness = 6 μm). (a) 3D micro-rings fabricated at a scanning velocity of 20 μm/s. (b)-(d) Different 3D structures fabricated with corresponding designs shown in insets. Fabricated structures are quite soft and are easily to be deformed.

and heat profiles generated temporally during each exposure time. Theoretically and experimentally, when exposure doses are close enough (below 400 nm), the integrated light intensity profile will be quasi-flat due to energy accumulation effect. Hence, it is impossible to fabricate separate features where generated heat profiles are still isolated leading to a possibility to create separated features and uniform structures.

Another structure, a pattern of "NANO" letters, was also fabricated with a feature size of 195 nm (figure 3.11) which demonstrated the ability of fabrication of arbitrary features with a high resolution.

3.5.3 Fabrication of 3D structures

In this experiment, different kinds of 3D structures were also fabricated by using the same laser system and with similar fabrication conditions, but with S1818 positive photoresist, whose thickness is about 6 μm. Examples of 3D structures are presented in figure 3.12. We have designed to fabricate 3D micro-rings with a height ranging from 3 μm to 6 μm. The used laser power is at 6 mW and a scanning velocity of 20 μm/s. The results is illustrated in figure 3.12(a). It can be seen that, microrings do not perform as the original design, they get smaller at the middle part and bigger on the top of the structures. It can be explained by a shrinkage of structures with large volume of material. The upper part of the ring gets bigger and tend to fall down due to the soft elastic characteristic of S1818. We also try to fabricate other shapes of 3D structures such as cube box, "cross-rainbows", and woodpile structures as demonstrated in figure 3.12(b-d). However, this phenomenon keeps on happening. Therefore, we sum up that positive photoresist is quite soft and easy to be deformed when fabricating 3D structures. Further studies of this idea are necessary to be carried to have final conclusion for this application. It is important to mention that 3D photonic structures have never been realized before with a positive photoresist. It is the first time, another use of it was exploited to fabricate 3D structures. We also note that if the input optical power and exposure time are too large, heating up materials to above 200°C, the increases of absorption coefficient (μ_{abs}) can raise the induced temperature; the photoresist at focusing region would explode as in case of ablation by laser. In conclusion, it is interesting that we have found down another use of positive photoresist in spite of their limitations. Many prospects are promising with a brand new idea.

Conclusion of chapter 3

In this chapter, we have developed a method for the fabrication of multi-dimensional polymeric positive nanostructures using a positive photoresist. This technique is based on the optically induced local thermal effect at the focusing region of a DLW system employing a green continuous laser. The locally induced high temperature (above glass-transition temperature) allowed solidifying (crosslinking) the positive photoresist, resulting in solid "positive" structures. The main results can be summarized as follows:

The thermal behaviour of the S1805 positive photoresist was investigated for a wide range of temperatures from room temperature to 500°C. Results show that the S1805 photoresist has crosslinking and glass transition thresholds around 156°C. It becomes insoluble in acetone above this threshold. Absorption coefficient dependence on annealing temperature is investigated as a function of temperatures.

We have developed a simple heat model to take into account the heat processes, which happens when the S1805 positive photoresist is strongly excited by a focusing beam at a wavelength of 532 nm.

By optimizing the laser power and the writing speed, nanowires with a feature size of 57 nm have been obtained, 1D structures with period of 300 nm have been achieved. Many 2D structures such as square and hexagonal patterns, arbitrary shape "NANO" letters were realized with a feature size down to 195 nm. A series of 3D structures were also fabricated. These structure can be useful for many applications. In the next chapter, we will use patterned photoresists as templates for producing plasmonic structures.

Chapter 4

Study of surface plasmon resonance in Au nano-holes array

4.1 Introduction

Numerous fabrication methods of plamonic structures have been proposed. For direct writing of metallic structures, focused-ion-beam milling is well-known as the most conventional technique [53,54]. This direct technique is however expensive and complicated. Another simple way is to use a polymeric template followed by the evaporation of a metallic thin film. This indirect method is nowadays commonly used due to its low-cost price and flexibility. The resist templates can be made by various ways, for example, nanoimprint, self-assembly, optical lithography [55–57], etc. The template structure is usually a bilayer with undercut profile to restrict the deposition of the metal covering the sidewall of the photoresist, otherwise, the template will be hardly lifted off. To fulfil this demand, DLW on the S1805 positive photoresist allows us to construct numerous micro and nano structures with arbitrary shapes, which might be excellent candidates for fabricating metal nanostructures by a combination of metal evaporation and lift-off technique.

Many kinds of plasmonic structures have been investigated for a wide range of applications. Among them, Au nano hole array (GNHA) is a potential and promising candidate for optical sensors or filters due to its extraordinary optical property [59,60]. In genearal, incident light on nanometer scale metallic structures can generate surface plasmon resonance (SPR) [61,62]. In filter applications, light incident on a GNHA excites the surface plasmon (SP) band on structural surface, then tunnels through holes that resulting in the increase of the light transmitted efficiency. In sensor applications, the incident light on a metallic film with nanoholes is initially scattered into SPs that penetrate the holes and are again scattered on the other side of the film. The extent of SP generation and the degree of transmission depend on the incident light wavelength, periodicity and material/medium dielectric constants. This phenomenon is highly applicable for fabrication of sensor devices. To date, several groups have demonstrated NHA as SPR-based sensors to detect changes in near surface refractive index [63–66]. The refractive index sensitivity of SPR-based sensor is defined as the change of spectral parameters of SPR with respect to the refractive index of the medium. Tetz et al. demonstrated a sensitivity of 1,022 nm/RIU for measurements in the NIR range [67].

In this chapter, we fabricated Au array structures using polymeric templates and a combination of metal deposition and lift-off processes. The first method is using uncross-linked templates and lift-off by acetone. The second method is using the cross-linked templates and lift-off by ultrasonication. Each method has different advantages and disadvantages. By using finite-difference time domain (FDTD) method, we calculated also the optical properties of fabricated GNHA structures. We finally studied the optical properties of GNHAs and demonstrated that these structures are promising for refractive index sensor application.

4.2 Fabrication of desired Au submicrostructures using uncross-linked S1805 templates

S1805 positive photoresists are used widely for fabricating integrated circuits (IC) and MEMS, owing to the non-shrinkage, developing process with less pollution solvent and easy to be stripped off after the pattern transfer. In this part, we investigated S1805 templates with various shapes, which were fabricated by DLW at low writing power (few microwatts), in order to fabricate desired Au plasmonic structures by a standard lift-off technique.

4.2.1 Fabrication process

As described in chapter 2, we can fabricate submicrostructures with any shape on a S1805 positive photoresist. Hence, we can master the S1805 templates for the fabrication of Au plasmonic structures as desired. The process is demonstrated in figure 4.1. There are four main steps including:

(1) Spincoating S1805 photoresist on pre-treated glass substrates.

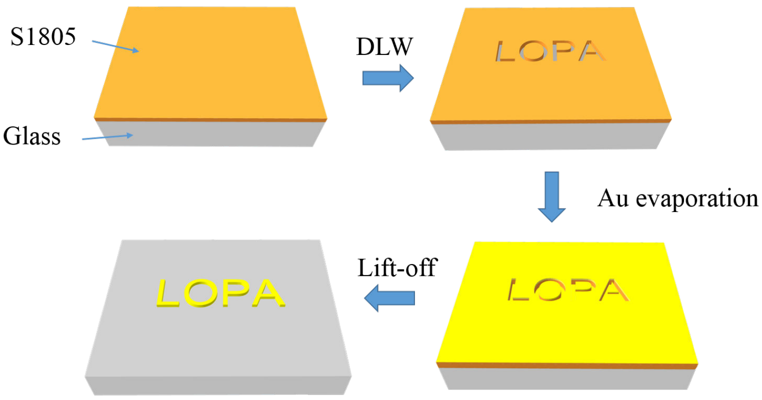

Figure 4.1: Illustration of fabrication process of arbitrary plasmonic structure.

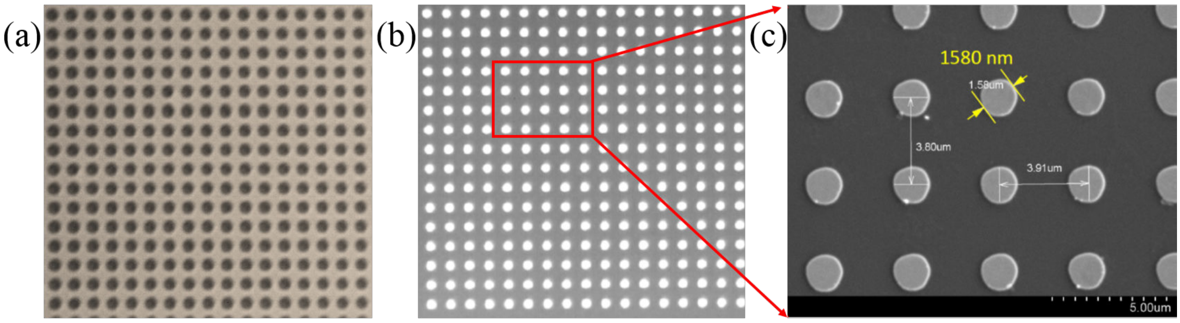

Figure 4.2: (a) Optical microscope image of a polymeric template (2D square structure) used for evaporation of Au film. (b) Periodic array of Au submicrometer disks obtained after lift-off process. (c) A zoom in of Au disks.

(2) Structuring by DLW and developing in AZ 351 developer.

(3) Evaporation of Au film on the top surface of S1805 templates.

(4) Lifting off photoresists in acetone.

After removing of unwanted photoresist parts, the desired Au submicrostructures are left on the glass substrates.

4.2.2 2D arbitrary Au submicrostructures

In this experiment, we use DLW with low laser power to write nano hole arrays on S1805 thin films. The depolymerization only occurs within the focusing spot by a mechanism of photoinduced chemical reaction. After developing the soluble parts, the polymeric template is obtained as shown in figure 4.2(a). The thickness of the S1805 layer is 600 nm,

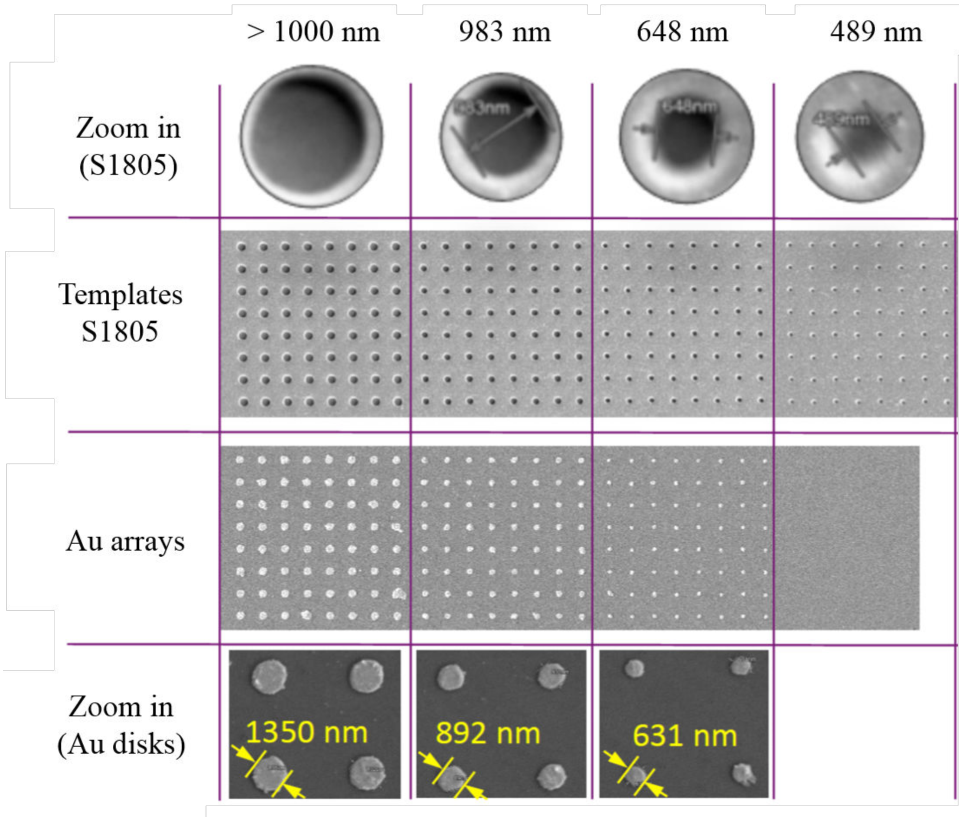

Figure 4.3: SEM images of templates S1805 fabricated at different exposure doses used for evaporation of Au film and corresponding periodic arrays of Au submicrometer disks obtained after lift-off process.

which directly determines the quality of Au structures afterward. If the thickness of the templates is too large (≥1 μm), it will cause some difficulties. Specifically, the soluble parts are hardly removed completely from the submicroholes. As in our case, S1805 monomers remained at the bottom of deep holes. Consequently, the Au layer will be deposited on the residual layer of S1805 instead of on the glass substrate as expected. Therefore, to fabricate submicrometer Au structures, the thickness of template layer should be thin, but of course not as thin as the Au thickness (50 nm). Au material then covered the whole fabricated templates by thermal evaporation method. In this way, Au atoms are sent to the target along one direction which allows them to go deeply inside the holes. The Au isotropic sputtering method is not working in this situation. In the final step, the templates were easily removed by acetone, leaving Au submicrodisks on glass substrate, as shown in figures 4.2(b,c). The shape of 2D Au structure depends on the template design.

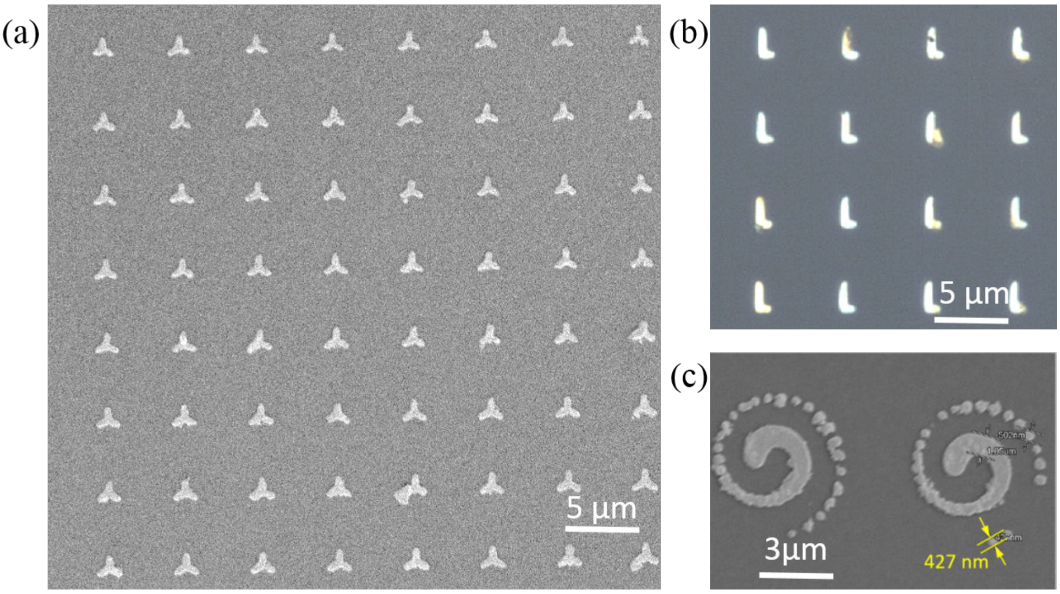

Figure 4.4: (a) Au microscale-star array. (b) Au nano "L" shape arrays. (c) Au spiral structures.

To go further studies on this idea, we fabricated series of templates of polymeric nanohole arrays with different diameters from $\geq$ 1000 nm down to 500 nm. The resulting Au nano disks are usually smaller than the hole-template as demonstrated in figure 4.3. When the polymeric nanoholes have a diameter of 500 nm and a height of 600 nm, Au nano disks were not produced as expected. It can be explained by the above mentioned-difficulties.

As other examples of 2D arbitrary Au structures, we also demonstrated the fabrication of plasmonic star structures with the smallest feature of 500 nm, as shown in figure 4.3(a), and nano "L" shape array and spiral structures, as shown in figures 4.3(b,c). These results have proved that we can fabricate any 2D arbitrary plasmonic structures by using a simple and low-cost method. Any complex structures could be easily obtained thanks to the flexibility of the DLW technique. The fabrication of plasmonic structures realized by this method is very promising for a number of applications. It is important to note that in order to fabricate "negative" plasmonic structures, we should realize "positive" photoresist templates, as demonstrated in chapter 2. However, it requires a lot of times for such structures. This method is mainly used to fabricate "positive" structures. In the next, we will demonstrate an alternative way to obtain "negative" plasmonic structures.

4.3 Fabrication of GNHA structures using cross-linked S1805 templates

Structures of cross-linked S1805 are fabricated by DLW via photoinduced thermal effect as demonstrated in the previous chapter. By using high excitation power, S1805 has a similar role as negative photoresist, which allows us to pattern the "positive" structures such as pillar arrays. With positive photoresist, there exist usually an oxidation effect on the surface of the resist. This phenomenon is called air-borne chemical contamination [68]. This effect seems to be a limitation for some applications, but it is a great advantage for fabrication of templates of plasmonic structures. The pillar structures fabricated by DLW technique behave a "mushroom - like" shape, which is high desirable to prevent the deposition of Au material on the sidewall of photoresist pillars. Comparing to other methods such as bilayer lift-off with undercut structures, this method enables a rapid fabrication of templates in a simple and flexible way. To demonstrate this idea, the GNHA structure is chosen to be designed, calculated and fabricated for further studies.

4.3.1 Design of GNHA structure and simulation of its optical response

GNHA structures have been proved to be potential candidates for applications of filters and sensors. Many theories and calculations have been carried out by a large amount of papers. Earlier theory showed that the spectral peak of the light transmitted through holes is given by [69, 70]:

$$\lambda_{SPP} = \frac{a_0}{\sqrt{i^2 + j^2}} \sqrt{\frac{\varepsilon_m \varepsilon_d}{\varepsilon_m + \varepsilon_d}}, \tag{4.1}$$

and its corresponding optical transmission minimum is given by:

$$\lambda_{SPP} = \frac{a_0}{\sqrt{i^2 + j^2}} \sqrt{\varepsilon_d}, \tag{4.2}$$

where a_0 is the periodicity of the holes, i, j are integers that define the particular order of the Bloch modes, ε_m is the permittivity of the metal, ε_d is the permittivity of the adjacent dielectric material. Based on these relations, we are motivated to design and to fabricate GNHA for further studies on it.

The GNHA can be varied by dozen of parameters such as Au gold layer thickness, diameter of nanohole, structural period and Cr layer thickness, which give different

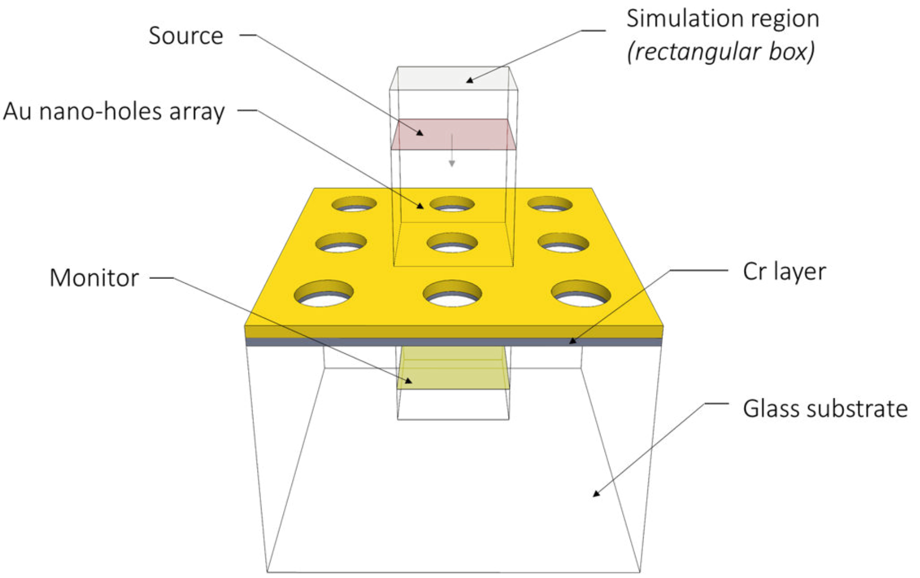

Figure 4.5: Illustration of FDTD model for Au nano-holes array.

optical responses of the whole pattern. To optimize the optical transmission response, we utilize FDTD method for theoretical calculations. In experiments, to track out optical transmission of GNHA, the structures are generally fabricated on a glass substrate. Nevertheless, there is a need for a thin adhesion layer between the glass substrate and Au film. This is usually done by a thin Cr layer of a few nanometers. The simulation model is illustrated in figure 4.5. The simulation parameters were selected and categorized into two groups as described below:

Fixed parameters: GNHA structures with round holes were chosen, because it is the most similar to the structures fabricated by DLW lithography. The optical constants of silica, Au and Cr were taken from [71–73]. The periodicity of GNHAs was fixed at 1000 nm. The net transmission of unpolarized light was calculated using the arithmetic average of the simulation results of individual and orthogonal polarizations [74].

Swept parameters: we swept the thickness of Au layer and Cr layer from $t_{Au} = 10$ to 90 nm and $t_{Cr} = 0$ to 20 nm, respectively. The diameter of the hole was also varied from $d_{hole} = 300$ to 900 nm. In addition, monitors were set within computation domain to analyse transmission spectra along with electromagnetic field distributions. Results were normalized to the transmission spectra obtained from a glass substrate (no GNHA) and evaluated right after each simulation to confine the parameters, with a purpose of the fastest convergence. Note that those values are close to experimental parameters.

Figure 4.6 shows the calculated transmission spectra of GNHA as a function t_{Au},

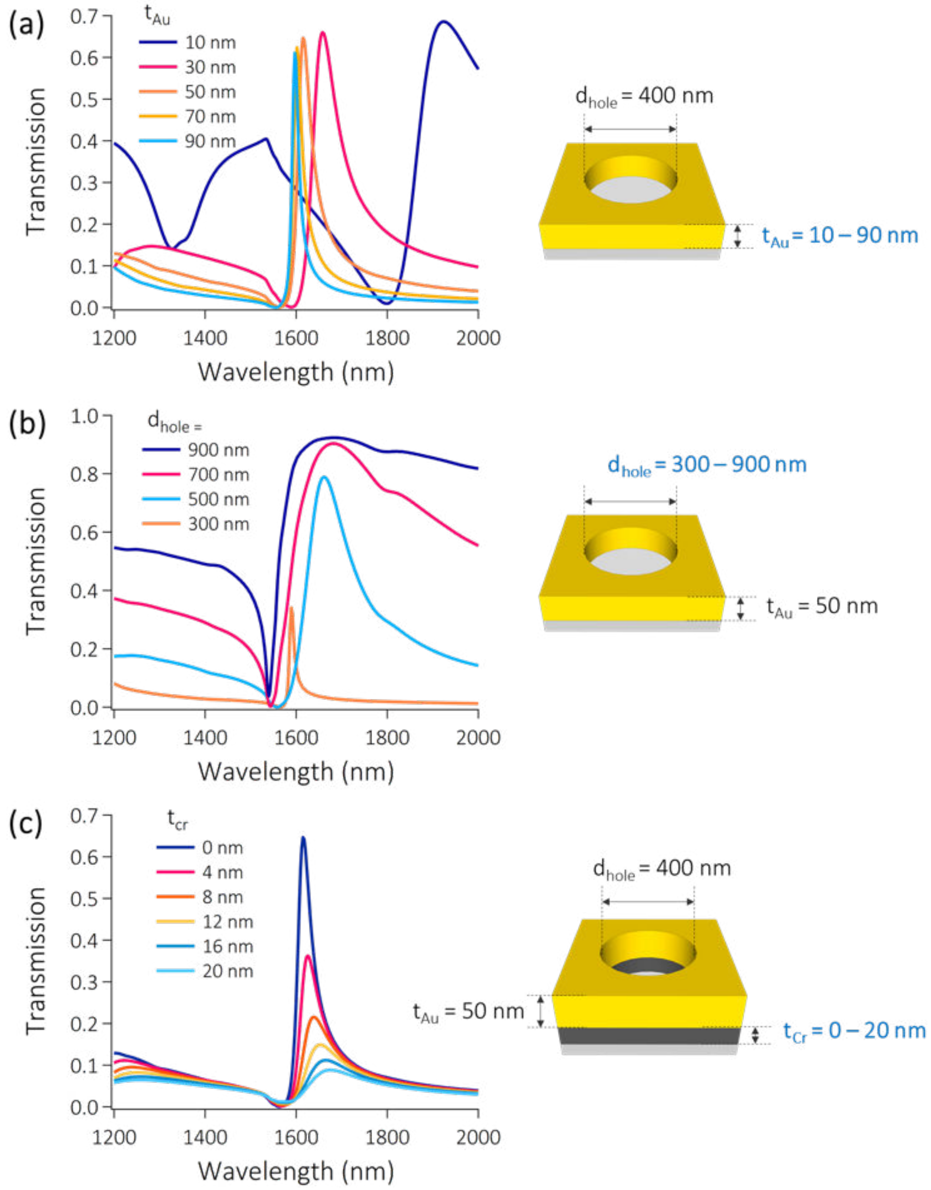

Figure 4.6: Calculated transmission spectra of Au nano-holes array: (a) As a function of Au layer thickness, t_{Au}; the diameter of the nano-hole is fixed at d_{hole} = 400 nm; (b) As a function of nano-hole diameter, d_{hole}; the thickness of the Au layer is fixed at t_{Au} = 50 nm; (c) As a function of Cr layer thickness, t_{Cr}; the thickness of the Au layer and hole diameter are fixed at t_{Au} = 50 nm and d_{hole} = 400 nm, respectively.

t_{Cr}, and d_{hole}. As can be seen in figure 4.6(a), the extraordinary optical transmission (EOT) peak position and width depend strongly on the thickness of GNHA. In details, this peak was blue-shifted and became shaper when we increased the Au thickness. It

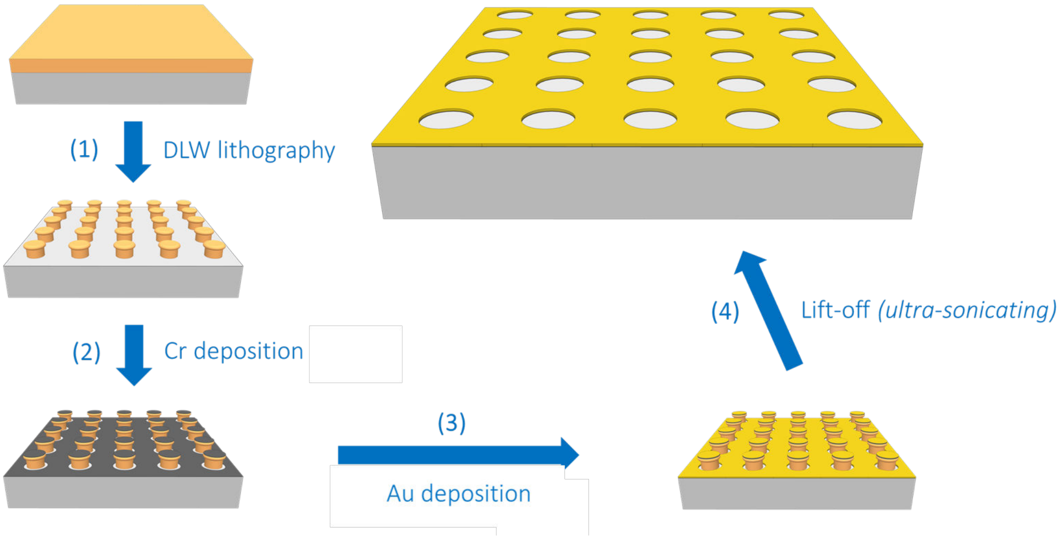

Figure 4.7: Illustration of fabrication process of GNHA structure.

suggests that by manipulating the plasmonic layer thickness, the structure can filter the selected wavelengths from 1600 nm to 1900 nm; when the Au thickness increases, the FWHM becomes narrower. In contrast, an increase of the adhesion Cr layer thickness suppresses the transmission peaks dramatically (figure 4.6(c)). This fact results in a problem that the thinner the Cr layer is, the less stable the Au layer is. If the Au layer does not have good adhesion with glass substrate, it will be easily damaged during the lift-off process. Another parameter which influences greatly the transmission spectrum is hole diameter, d_{hole}. Bigger holes allows higher transmission coefficients, however, band selection is poor. Conversely, smaller holes allows fewer transmission resonance modes, which makes transmission peak shaper but also decrease the transmission coefficients. Specifically, if d_{hole} is in the range of 300-500 nm, the transmission peaks are most appropriately obtained.

4.3.2 Fabrication process of GNHA

Based on this insight along with advantages and disadvantages of our fabrication method, we decided to choose t_{Au} = 50 nm; t_{Cr} = 15 nm; and d_{hole} = 400 nm for the next fabricating steps.

We employed our newly-developed DLW of polymeric nano-structures via optically induced local thermal effect, which has been introduced in the previous chapter [75]. A high illumination intensity laser beam is tightly focused to heat up a selected volume of

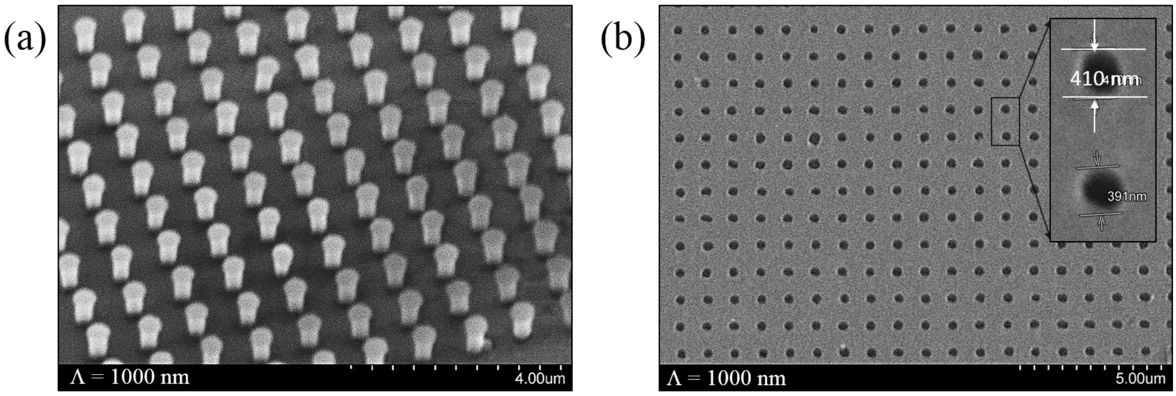

Figure 4.8: (a) Side-view SEM image of pillar arrays fabricated by optically induced local thermal effect DLW lithography. (b) SEM image of Au nano-holes array after lifting-off polymeric template.

photoresist over glass transition temperature (T_g) and resulting in cross-linked polymer. Thanks to advantages of this method, we were able to fabricate a highly uniform and robust polymeric nano-pillars arrays, which then served as templates for GNHAs.

Figure 4.7 illustrates the fabrication process of GNHA by DLW lithography and lift-off technique. After step (1) of DLW lithography, we obtained a polymeric nano-pillars template. Thanks to the oxidation on the surface of S1805 after spincoating and exposing in air [68], these nano-pillars possess a special "mushroom-like" shape, which is especially appropriated for metal sputtering and lift-off method. The umbrella-like head part prevented Cr and Au to be deposited onto the side of nano-pillars. Step (2) is the sputtering of a thin Cr layer. In step (3) templates were covered by a 50 nm-thickness Au layer. Homogeneous Au was evaporated from tungsten boat at 1-3$\times10^{-6}$ Torr at a deposition rate of 0.1 nm/s. The nano-pillars were then lifted-off by ultra-sonicating in the last step, leaving GNHA structures on the glass substrate.

4.3.3 Experimental results of GNHA

We successfully fabricated GNHA structure, with a 15 nm of Cr adhesion layer. This Cr layer is necessary in order to keep the Au structure on the glass substrate during the lift-off process by ultra-sonicating method. Figure 4.8(a) shows a side-viewed SEM image of polymeric pillar arrays (Λ = 1000 nm). The mushroom-like shape of pillars is clearly observed. The corresponding GNHA structure after metal deposition and lift-off is shown in figure 4.8(b). The thicknesses of Au and Cr were controlled to be 50 nm and 15 nm by controlling thermal evaporation rate and time, respectively. The hole diameter

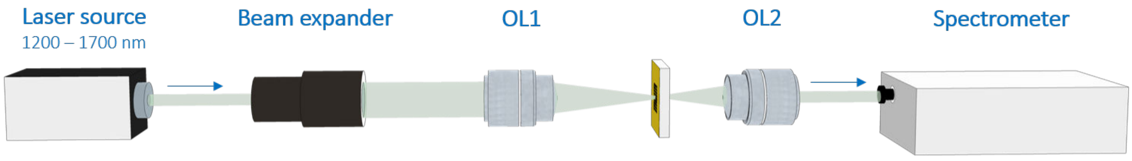

Figure 4.9: Experimental setup of Au nano-holes array transmission measurement.

was tuned by varying the diameter of the pillar template. The hole diameter of this HA structure was obtained around 400 nm as our initial design.

4.3.4 Characterization of fabricated nano-holes array

4.3.4.1 Experimental setup

Another experimental setup was constructed to measure the transmission of GNHA structure. We used a *Supercontinuum* laser (λ = 1200 nm - 1700 nm, unpolarization) as the illumination source. The beam was then expanded and focused through the GNHA structure by an objective lens (OL, NA=0.4). The GNHA was set on a horizontal holder, which is perpendicular to the incident beam. This allows us to change the surrounding media of GNHA easily from air to water or oil by simply casting a drop of the desired medium. The transmission spectrum was collected by another OL and transmitted to a *NIR Quest OceanOptics* spectrometer. The detected transmission spectrum was normalized to the transmission spectrum of glass substrate (without GNHA). Experimental results were then summarized and compared to predicted simulation results.

4.3.4.2 Results and discussions

A remarkable similarity between experimental results and theoretical calculations is emphasized in figure 4.10. From the calculation results, we can observe a transmission dip around 1535 nm, which is consistent with other analytical model for estimating resonance peak position of metallic structures [69]. Figure 4.11(b) shows the near field distributions of the electric field intensity (normalized) at wavelength of 1535 nm. This image confirms that this dip corresponds to the SPR band on the interface of the gold-glass substrate. The experimental transmission spectrum follows the evolution trend of calculation, which predicted to have a transmission peak around 1700 nm. However, due to the limitation of the infrared laser source and spectrometer, we could not fully characterize this transmission band of the GNHA structure.

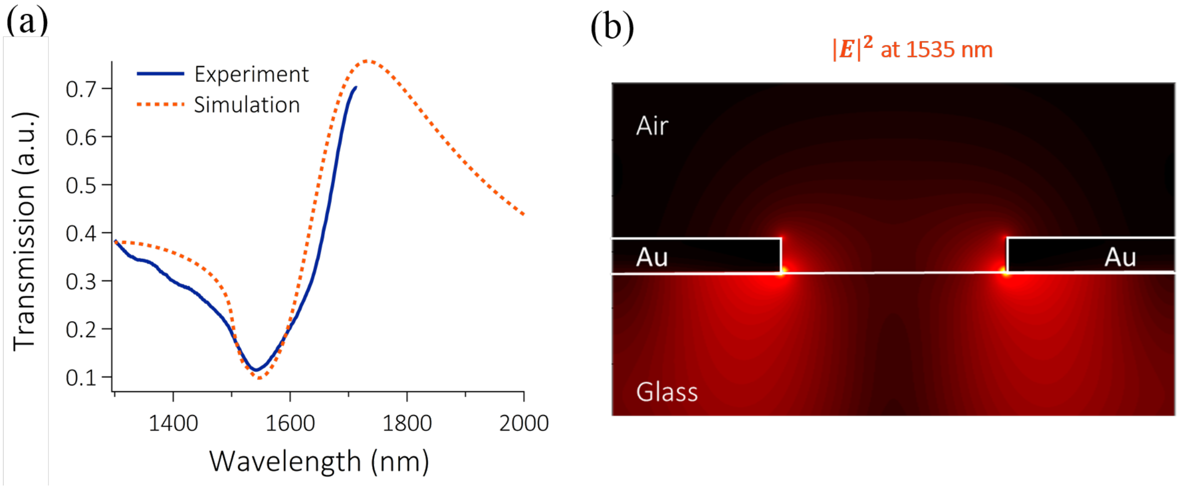

Figure 4.10: (a) Experimental and calculated transmission spectra in air of fabricated Au nano-holes array structures. Parameters for simulation are: $\Lambda = 1000$ nm, $d_{hole} = 400$ nm, $t_{Au} = 50$ nm and $t_{Cr} = 15$ nm. (b) Simulation of the near field distributions of the electric field intensity (normalized) at wavelength of 1535 nm.

We broadened our GNHA transmission experiment from air to different surrounding media, such as water ($n = 1.33$) and oil ($n = 1.51$). From analytical model of [69], we expected a transmission dip approximately close to the wavelength of $\Lambda \times n_d$ with n_d is the refractive index of surrounding media, *i.e.* transmission dips around 1330 nm and 1500 nm for water and oil, respectively.

Indeed, we observed those dips on both experimental and theoretical transmission spectra, as shown in figure 4.11. Experimentally, the transmission dip at $\lambda_G = 1535$ nm (corresponding to SPR at glass-Au interface, in short: glass-mode) was unchanged in all three cases of water, oil and air. Another dip appears at $\lambda_W = 1335$ nm when we embedded GNHA in water, called water-mode. This dip red-shifted to $\lambda_O = 1510$ nm when GNHA was immersed in oil, called oil-mode. By FDTD simulation, the field distribution (figures 4.11(c,d)) show that the resonance of the water-mode (λ_W) has a local maximum intensity at the top of GNHA, which is the interface of water and Au, while the resonance of the oil-mode (λ_O) has a local maximum intensity at the bottom of the GNHA, which is the interface of metal and glass. The obtained results show a strong shift in the SPR of $\triangle\ \lambda = 185$ nm for a refractive index varying between 1.33 and 1.51, which is corresponding to a sensitivity of 1027 nm RIU^{-1}.

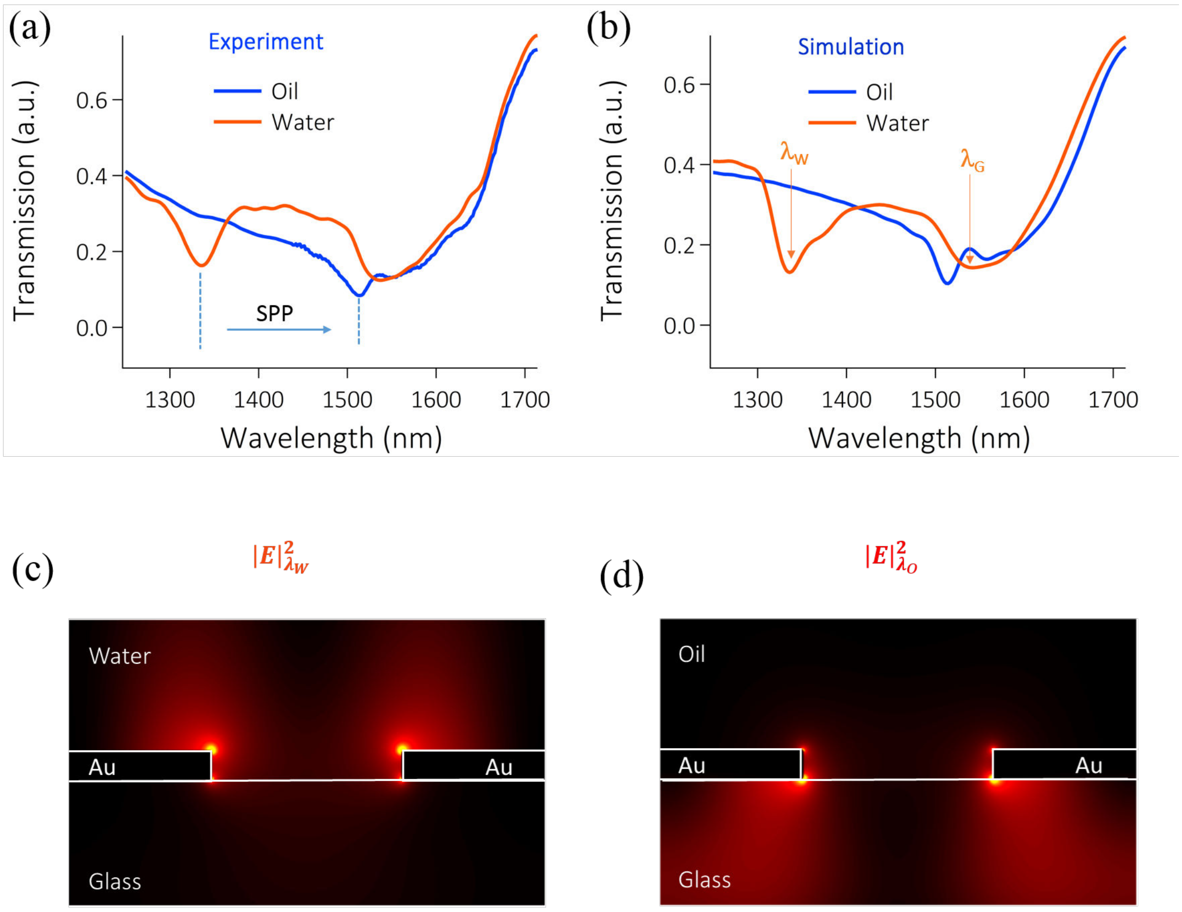

Figure 4.11: (a) Experimental and (b) calculating transmission spectra of fabricated Au nano-holes array structures in different media. Parameters for simulation are: Λ = 1000 nm, d_{hole} = 400 nm, t_{Au} = 50 nm and t_{Cr} = 15 nm. Simulations of the near field distributions of the electric field intensity (normalized) (c) at wavelength of 1335 nm in water and (d) at wavelength of 1510 nm in oil medium.

Conclusions and Perspectives

In this chapter, two methods for fabrication of S1805 templates were demonstrated. The first one is using the uncross-linked templates which were then lifted-off by acetone. The second method is using cross-linked S1805 templates fabricated at high laser power, which were then lifted-off by ultrasonication. In combination with the evaporation technique, each method can create different Au plasmonic structures. Specifically, Au nanodisk, nano star and “L” shape arrays were fabricated by uncross-linked templates, while the GNHA structures were produced by cross-linked templates. The advantages of those methods are their low price and their simplicity. For further studies in sensor application, we investigated in detail design, fabrication and characterization of GNHA structures. The obtained GNHA was characterized by a home-made transmission setup, the transmission of GNHA is in consistent with our initial design and simulation results. We found that surface plasmon polariton bands are specially sensitive to the surrounding medium. A long-shifted wavelength distance of 185 nm (from 1330 nm to 1515 nm) was obtained as the surrounding medium varies from water ($n = 1.33$) to oil ($n = 1.51$) corresponding to 1027 nm RIU^{-1}. This result is very promising for high sensitive refractive index sensors.

Chapter 5

Patterning of 2D Au nanostructures by DLW and thermal dewetting technique

5.1 Introduction

Metallic objects exhibit special optical properties deriving from the excitation by an electromagnetic field [13]. This property is called surface plasmon (SP) and expressed as strong light scattering and absorption. The appearance of SP bands and enhancement of local electromagnetic field depend strongly on the size and shape of metallic structures. These structures are very interesting for various applications, such as sensor [77], photocatalyst [78], filters [79], etc. Different plasmonic structures have been theoretically and experimentally demonstrated in previous chapter.

Besides, gold nano island arrays (GNIA) presents a strong plasmon surface resonance [76]. GNIA can be realized by electron beam or focused ion beam lithography combined with metal evaporation and lift-off techniques [80]. However, these lithography methods have a disadvantage in terms of facility cost and complexity. One of the useful ways for producing the plasmonic structures is metal film dewetting by thermal annealing technique [81–83]. Mechanisms for dewetting are well-known such as heterogeneous nucleation, which starts from a defect located at the film surface or the film-and-substrate interface, homogeneous nucleation, which is involved by a small thermal density fluctuation and may act as a nucleus for hole formation, and spinodal dewetting, which occurs through the amplification of periodical film thickness fluctuations (i.e., capillary wave). At high annealing temperature the metallic films induce self-correlated dewetting patterns, resulting in random monolayer metallic nanoparticles (NPs).

In general, dewetting of metal films is induced by a direct thermal annealing on a hot plate or by radiation of a high energy beam such as laser beam or electron beam [84,85] by which metal films would be ruptured and shrieked. Studies concerning formation of random island structures upon annealing of Au island thin films [86], percolated films [81] and thick films [87] were reported. Annealing temperature close to the glass transition temperature of glass substrate ($T_g = 557°\text{C}$) resulted in slow gradual embedding of Au island in the glass [81]. The influence of the substrate on the formation of Au nano islands was studied for a thickness of 7.5-15 nm of Au film on mica, quartz [88], as well as bare [89] and silanized glass [86]. Furthermore, the formation of periodic structures in dewetting process can be assisted by utilizing nano plastic forming [90], a sacrificial antimony layer [91], or by means of assembly colloidal crystal [92]. These assistances would create the modulated defects generating periodic structures after a heating treatment process.

In this chapter, we first investigate in detail the formation of random Au islands from sputtered Au films at high annealing temperatures. Use of a range of Au thicknesses and different substrates for subsequent high temperature annealing enabled tuning the SP band wavelength of Au island films. Second, we demonstrate a precise control of the formation of GNIA by a combination of DLW lithography and thermal annealing technique. The DLW allows to form periodic polymer structures, which serve as a soft substrate for sputtering Au thin films. The high annealing temperature will remove the polymer substrate leaving a periodic Au nano structure.

5.2 Realization of random Au island monolayers by thermally induced dewetting effect

5.2.1 Experimental procedure and characterization techniques

Au films of various thicknesses were deposited onto pre-treated substrates using an Emitech K650 magnetron sputterer. The deposition conditions were chosen as direct-current Ar plasma, gas purity of 99.995% and discharge current of 50 mA. The sputtering time was controlled from 1 to 10 minutes to obtain the desired Au thickness. To reveal the influence of substrates on the formation of the Au islands films during the annealing process, three different types of substrates were employed: microscope slide glass (Menzel-Glaser), microscope glass coated with indium tin oxide (ITO), and microscope

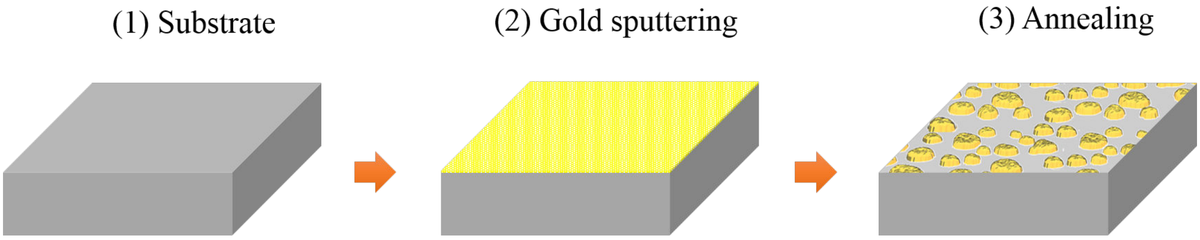

Figure 5.1: Fabrication process of random Au nano islands by thermal annealing method.

glass spin-coated with S1805 photoresist. Thermal annealing treatment was carried out in ambient condition at different temperatures between 25°C and 500°C (accuracy ± 5°C) using a Nabertherm oven. Note that the highest annealing temperature was chosen to be lower than the glass transition temperature of the glass substrate ($T_g = 557$°C). The annealing process involved three consecutive steps: an increasing temperature step from room temperature to the desired temperature at a heating rate of 5°C/min, a constant annealing step at the target temperature for 30 minutes, and a natural cooling down step. The structured morphology of the resulting structures was characterized by atomic force microscopy (AFM) and scanning electron microscopy (SEM). The optical properties of the structures were characterized by optical microscopy and ultraviolet visible (UV-Vis) spectrometer.

5.2.2 Influence of Au film thickness

Au films were sputtered on pretreated glass substrates with various thicknesses. Films below a nominal thickness of 10 nm are initially discontinuous, whereas the as-sputtered 10-16 nm films are percolated, and films above a nominal thickness of 16 nm are fully percolated and thick. The morphology of thin Au films sputtered on glass and annealed for 30 minutes at 500°C was observed by SEM (figures 5.2,5.3) and AFM (figure 5.4). It shows that dewetting films having a thickness of less than 10 nm results discontinuous film to a high density of small Au NPs, whereas annealing of the films with thickness of 10-24 nm results in formation of islands with scalable dimensions. Films produced from the initially sputtered Au films present large, faceted islands with flat top surfaces (figure 5.4). This confirms again that, during the annealing process, the sputtered material was melted and re-crystallized in the form of isolated nanoislands [81]. The islands with average diameters of 65 nm, 200 nm, and 400 nm are generated from sputtered layers with the thickness of 6 nm, 12 nm, and 24 nm, respectively.

Microscope images and transmission UV-Vis of the Au nano-islands prepared from

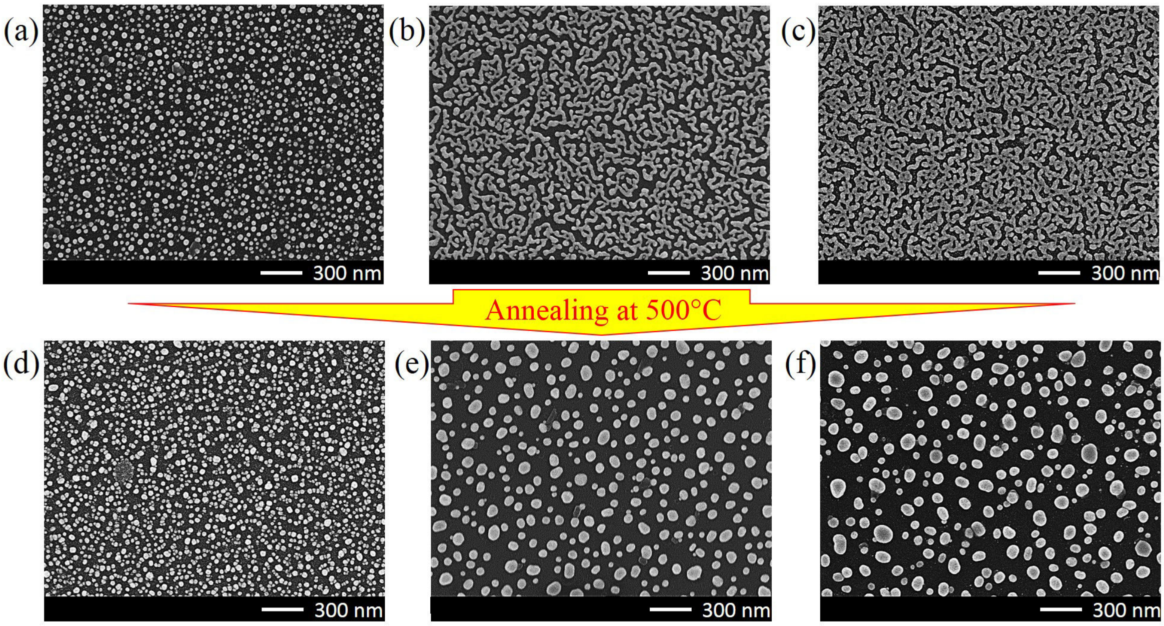

Figure 5.2: SEM images of Au films sputtered on glass substrates (a)-(c) and corresponding films annealed for 30 minutes at 500°C (d)-(f). Nominal thicknesses (in nm): (a), (d) 5; (b), (e) 10; (c), (f) 15.

different sputtered Au layers are shown in figures 5.5(a,b) The optical response of the sputtered Au structures is related to their thickness. It shows that the thicker films become darker. It is obvious that the sputtered Au structures exhibit a substantial difference in the optical properties. The absorbance of the structures remarkably increase with the film thickness. For the sample sputtered with the thickness of 2 nm and 3 nm, the structures exhibit weak absorbance with an observable peak located around 550 nm, which slightly red-shifts with the thicker film. This is a standard signature of the localized surface plasmon resonance (LSPR) absorption of island-film structures that are formed when Au is deposited on glass and many other types of substrates [93,94]. For the films with intermediate thickness, higher absorbance with a dip minimum around 500 nm was found, which is similar to the optical behavior of the bulk form. These finding are well consistent with the previous experimental and theoretical studies [86,93,95].

Figures 5.5(c,d) show the microscopic characterization of the Au nano-island structures prepared on a glass substrate by annealing the sputtered Au layers (various thicknesses) at a temperature of 500°C. An increase of the optical extinction peak with thicker sputtered Au layer was obviously observed. Moreover, the corresponding extinction peak position gradually red-shifts with increasing of film thickness, from 542 to 590 nm. The

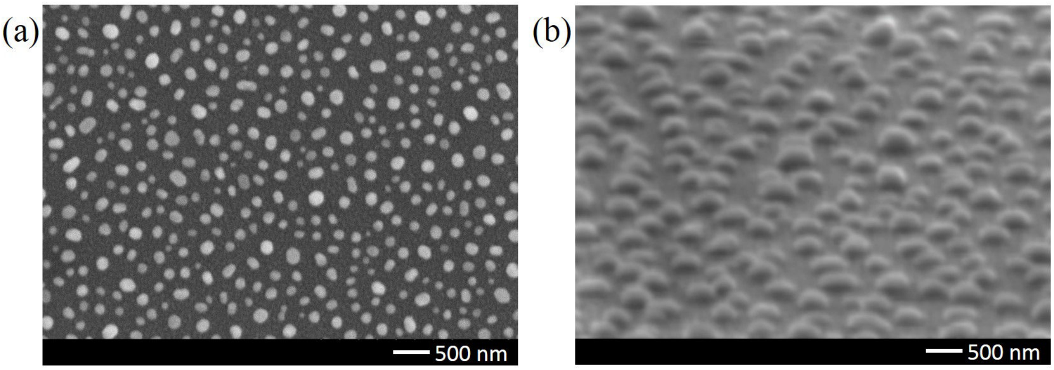

Figure 5.3: SEM image of 12 nm Au island films sputtered on glass substrate and annealed for 30 minutes at 500°C. (a) top view and (b) side view.

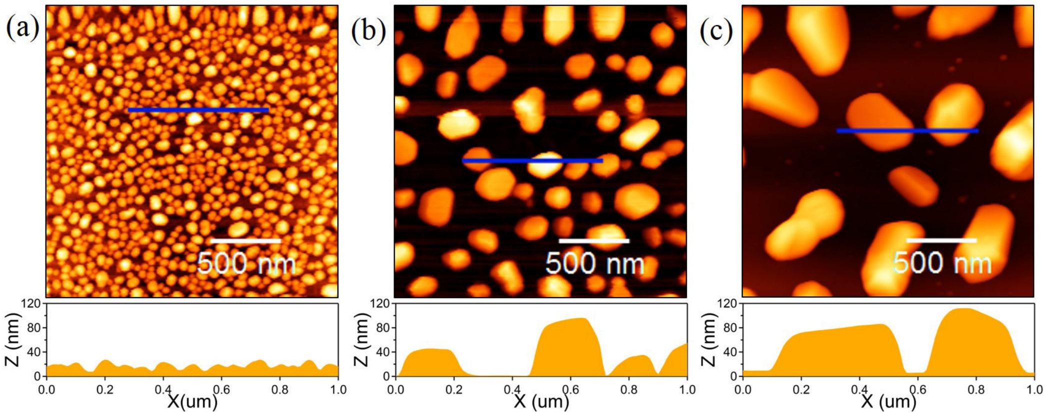

Figure 5.4: AFM images of 6 nm (a), 12 nm (b), and 24 nm (c) Au island films on glass substrates, prepared by Au sputtering on glass followed by 30 minutes annealing at 500°C.

red-shift of the plasmonic resonance is attributed to an increase of the Au nano-islands sizes. Note that the spectral position of the plasmon resonance depends not only on the shape and the height/diameter ratio of the Au nano-islands, but also on the dielectric constant of the surrounding materials. Thus, we have observed a red-shift of the extinction spectrum as a result of multifold effects. However, with the thick film, for example, 24 nm, we do not see high contrast of extinction peak. In this case, extinction peak is extended to the infrared range.

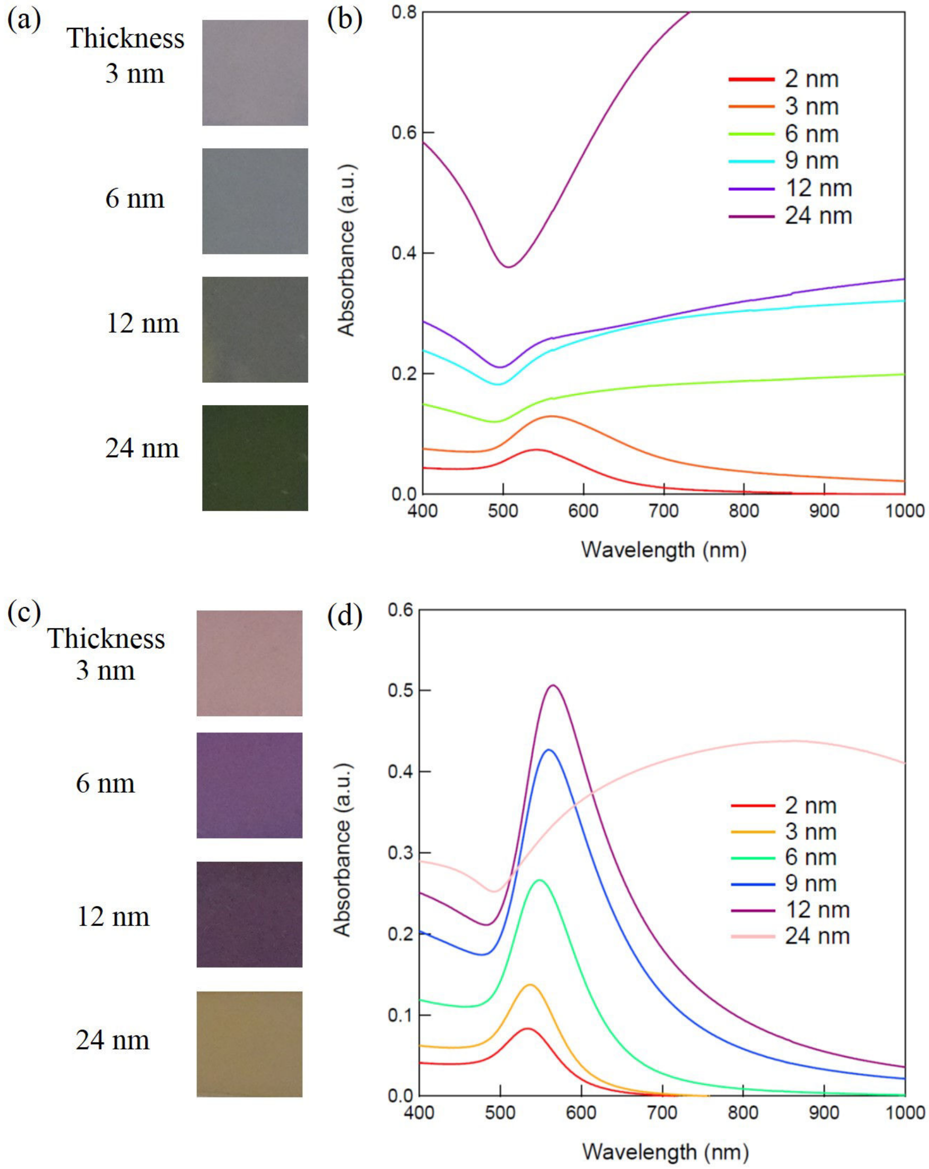

Figure 5.5: Microscope images (a) and UV-VIS spectra (b) of Au films sputtered on glass substrate with different thicknesses. (c) Microscope images and (d) UV-VIS spectra of Au films sputtered on glass substrate with different thicknesses and annealed at 500°C.

5.2.3 Influence of thermal annealing temperature

The surface morphology of the Au films on the glass substrate changed dramatically after the annealing process, as clearly shown by the AFM images in figure 5.6. It is evident that annealing leads to formation of discrete Au nanoislands from the continuous sputtered Au

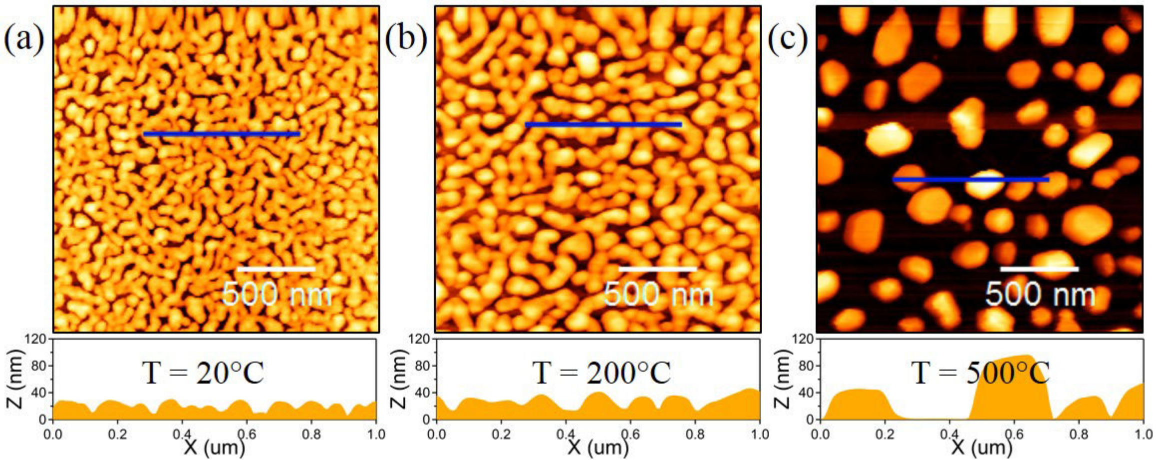

Figure 5.6: AFM images of 12 nm Au island films on glass substrates, prepared by Au sputtering on glass followed by 30 minutes annealing at different temperatures. Annealing temperatures: (a) room temperature; (b) 200°C; (c) 500°C.

layer. The progression of this transformation can be observed by noting the dependence of the sample morphology on the annealing temperature. The sample annealed at 200°C exhibited hillock morphology containing holes, alternately incorporated with Au chains (figures 5.6(b)). Such hillock formation is probably caused by the unidentified thermal expansion of the glass substrate and the coated Au layer. In contrast, by annealing at 500°C, completely isolated nanoislands structure was obtained. It is well known that the melting point of Au nanoplatforms decreases rapidly with reduction of the particle size [96]. Therefore, it is assumed that, during the high temperature annealing period, hillock-form Au layers melted and then coalesced into isolated particles. Furthermore, as clearly observed from figures 5.6(c), the Au islands display flat surfaces, indicating that the molten Au recrystallized during the high annealing temperature period. Figure 5.7 shows microscopy images and UV-Vis spectra of Au samples obtained before and after annealing at different temperatures. The original sputtered film appears in dark blue, whereas all annealed samples exhibit reddish color, a trend that becomes increasingly apparent with higher annealing temperatures. The absorbance spectra of the annealed structures were qualitatively different in terms of both shape and height compared with the initial sputtered film. A strong optical extinction band starts to appear for the sample heated at 200°C and becomes more obvious for the samples annealed at higher temperatures, whereas the original sputtered layer showed a broad optical band. The well localized and remarkably enhanced extinction bands of the annealed samples are attributed to LSPR of Au nanoislands. However, we did not observe a clear shifting trend

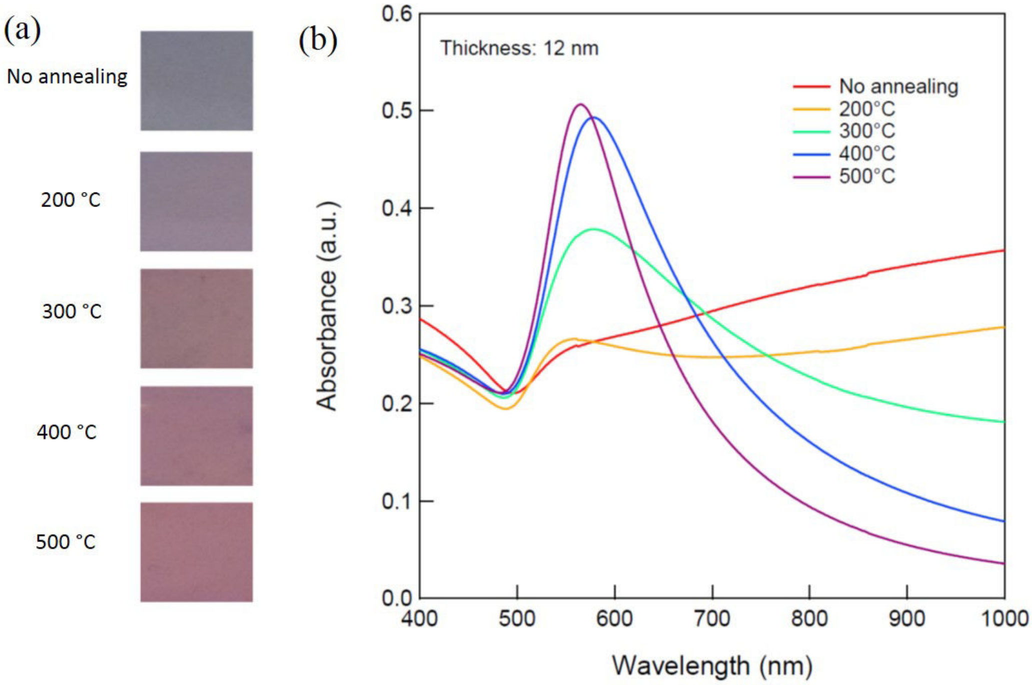

Figure 5.7: Microscope images (a) and UV-VIS spectra (b) of sputtered Au thin films on glass substrate, obtained before and after annealing at different temperatures.

of the resonance peak wavelength of these samples with the optical extinction peaks being located at 560 nm, 575 nm, 578 nm, and 566 nm for annealing temperatures of 200°C, 300°C, 400°C, and 500°C, respectively. This is due to the fact that the particle plasmon resonance depends strongly on the size, shape, and aspect ratio (height/diameter) of the Au nanoislands, as well as on the surrounding medium. As the annealing temperature increases, the structured morphology features of the islands, and consequently the total contact area of the sample with the environment, change in different ways, leading to nonmonotonic variation of the resonance spectrum. In addition, it can be seen that the extinction band of the samples annealed above 400°C did not change significantly with the temperature, as for the samples annealed at intermediate temperatures. This indicates that, in the temperature range below the glass-transition temperature of the glass substrate, 12 nm-thick sputtered Au film shows a high-quality SPR band after annealing at temperatures between 400°C and 500°C.

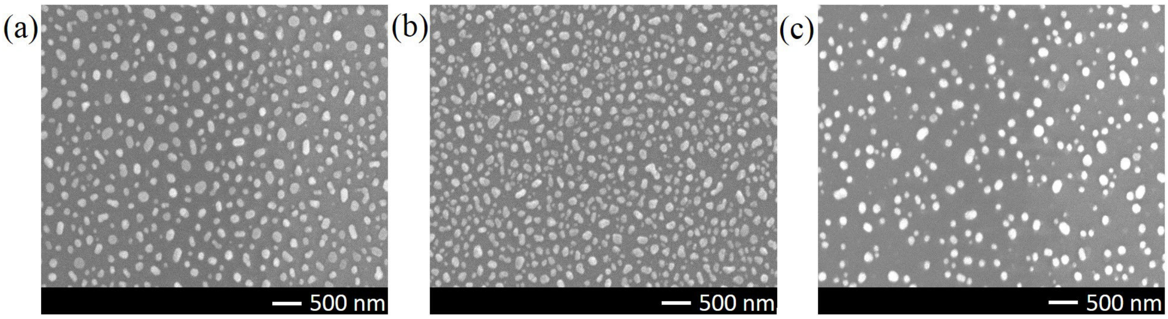

Figure 5.8: SEM images of Au film (thickness = 12 nm) structures obtained by thermally annealing Au film sputtered on different substrates: glass (G), glass coated with ITO (I), and glass initiallly coated with S1805 photoresist (S). The annealing temperature was 500°C.

5.2.4 Influence of substrates

Figure 5.8 shows SEM images of Au islands structures obtained after thermal annealing at 500°C of the metallic layer sputtered on different substrates. It is apparent that the substrate has a remarkably impact on the morphological features of the resulting island films. Au nanoislands with larger average diameter and smaller average height were produced on pure and ITO-coated glass as compared with the substrate coated with S1805. The results presented above show that the sputtered thin film melted and coalesced into isolated nanoislands during the annealing process. Therefore, the nature of the substrate, particularly its surface tension properties, is assumed to be a crucial factor directly impacting on the structured morphology and consequently the optical properties of the final Au island film. The surface tension of the substrate determines the interactions between the substrate and molten Au. Additionally, the thermal expansion of the substrate is also a vital factor affecting the features of the resulting metal structures. It should be noted that, during the thermal annealing, there is a phase transformation processes of the S1805 photoresist, which has a glass-transition temperature of around 160°C and evaporates completely at temperatures above 350°C (see figure 3.3 of chapter 3). Therefore, although the S1805 interlayers disappeared from the final Au sample, they played a crucial role in the formation of Au islands during the annealing period. In contrast, the ITO nanolayer was not modified in the chosen range of annealing temperatures. Figure 5.9 shows optical microscopy images and optical extinction spectra of Au island films on different substrates. The Au sample looks purple on pure glass, dark green on ITO, and light red on the initially photoresist-coated substrate. The corresponding

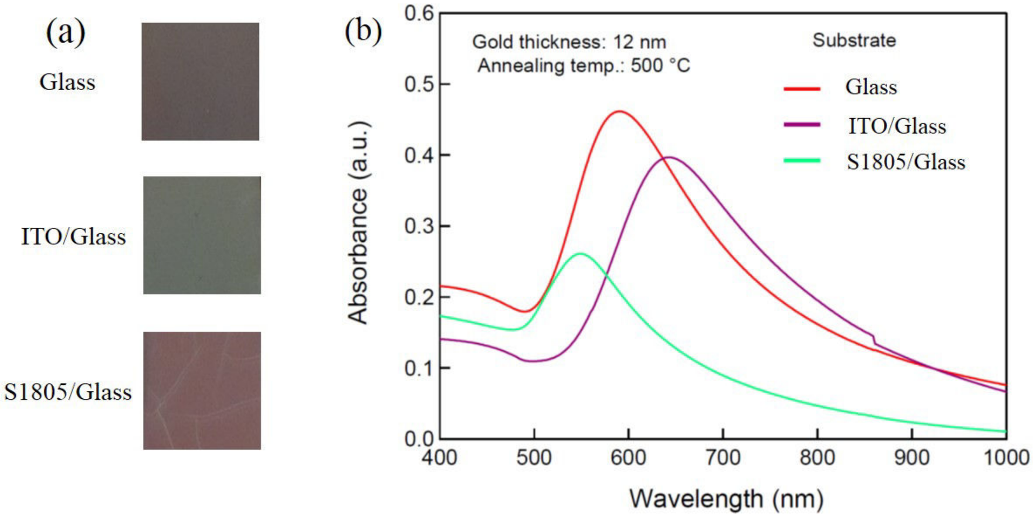

Figure 5.9: (a) Microscope images and (b) UV-VIS spectra of Au film structures obtained by thermally annealing Au film sputtered on different substrates: glass (red), glass coated with ITO (violet), and glass initially coated with S1805 photoresist (green). The annealing temperature was 500°C.

UV-Vis spectra show that particles plasmon induces extinction centered at 643 nm on ITO, 590 nm on pure glass, and 550 nm on the initially S1805-coated glass substrate. Two dominant mechanisms are taken into account for the spectroscopic properties of the Au nanoislands on a substrate: (1) a structure-dependent effect, determined by the size, shape, and separation of the Au islands, and (2) the dependence on the environmental refractive index, with ITO having the largest (1.86) and pure glass the smallest value (1.51) among the substrates used, at 633 nm. Therefore, the spectroscopic properties of the Au structures realized on different substrates are determined by many-fold related mechanisms that require further characterization. However, the supporting substrate has been shown to be an effective element that can be used to tune the optical response of such Au nanoisland films. Interestingly, the use of an interlayer that can be completely eliminated during the annealing process is a promising practical approach to produce the desired metal structures. This concept is demonstrated in the next section.

5.3 Fabrication of Au nano island arrays

In the previous part, we present the dewetting effect of Au nano island films. Random Au nano islands structures are produced by heterogeneous nucleation mechanism due to nonperfect of as-sputtered films. In this part, we present new strategy for fabrication of

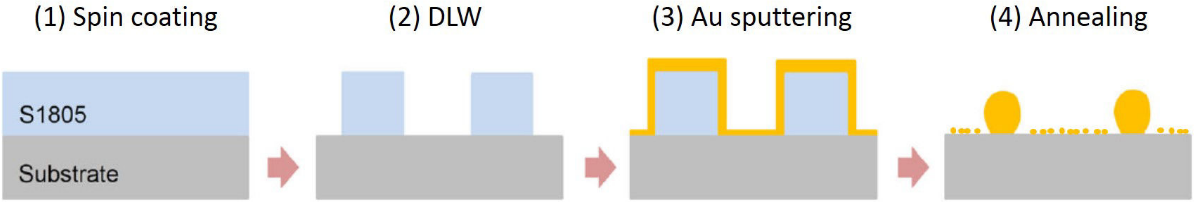

Figure 5.10: Illustration of fabrication process of structured Au arrays by a combination of DLW and thermal annealing.

Au nano island arrays (GNIA). We use a structured S1805 template as a sacrificial layer, which would be removed during the annealing process and resulting in a periodicity of Au nano islands.

5.3.1 Experimental fabrication process

The procedure for fabricating GNIA is shown in figure 5.10 including four steps: (1) preparation of samples, (2) fabrication of S1805 templates by DLW, (3) sputtering an Au layer, and (4) annealing the samples at high temperature to remove the templates and to obtain Au periodic structures.

Samples preparation and fabrication of templates

To fabricate templates, the S1805 photoresist was first coated on pre-treated glass substrates and then pre-baked at 115°C for one minute to remove the residual solvent. Then, polymeric structures were fabricated by the DLW as demonstrated in chapter 2. The templates were fabricated with different periods of 0.6 μm, 0.8 μm, and 1 μm, and with different filling factors.

Preparation of Au layers

The Au films were sputtered on S1805 templates with a thickness ranging from 6 to 24 nm by using an Emitech K650 magnetron sputter. All sputtering conditions are similar to what used and presented in previous section.

Annealing

All samples were annealed at 500°C (accuracy $\pm$ 5°C) using a Nabertherm oven. Note that the S1805 templates would be removed quickly at a temperature higher than 350°C. The annealing process involved three consecutive steps: an increasing temperature step from room temperature to the desired temperature at heating rate of 5°C/min, a constant annealing step at the target temperature for 30 min, and a natural cooling down step.

Morphology characterization

The morphology of polymeric and plasmonic structures was observed using scanning electron microscopy (SEM) and optical microscopy.

5.3.2 Results and discussion

5.3.2.1 Formation mechanism

Figures 5.11(a-b) show SEM images of Au structures. The corresponding S1805 template (period = 1 μm) sputtered by an Au layer of 10 nm before annealing is presented in the inset of image (figure 5.11(b)). It is evident that, after the annealing process, the photoresist was removed and the Au material remained on the substrate in the form of a periodic array. Note that small Au NPs remaining around the Au islands array are due to the dewetting of Au area in contact with glass substrate whereas the array of larger Au NPs are obtained at the same position of S1805 in template lattice. The mechanism explaining the formation of Au arrays is illustrated in figure 5.11(c). After sputtering process, a thin Au layer was anisotropically deposited onto the top and side-walls of the S1805 pillars and the blank areas of the glass surface. Au film thickness at the top of pillars is thicker than that of side-walls and blank areas. During the annealing process, when the temperature was increased to above 350°C, the Au layer started to melt and broke down into segments, allowing the S1805 to evoparate gradually, as demonstrated by the dotted blue arrows. The loss of S1805 due to evaporation led to an aggregation of gold (bold red arrows). At high temperature of around 500°C, the S1805 evaporated completely and the Au initially coated on S1805 aggregated and coalesced into localized and well arranged dots.

5.3.2.2 Influence of Au layer thickness on the formation of GNIA

Different samples of S1805 templates (period = 0.8 μm) were fabricated in the same conditions on 100 × 100 (μm) areas. SEM images of these templates are shown in insets of figure 5.12. The templates were sputtered by Au layers with a thickness ranging from 6 nm to 24 nm and annealed at 500°C for 30 minutes. Figure 5.12 shows SEM images of the fabricated GNIAs. It is evident that the Au covering S1805 lattices aggregated and coalesced into arrays of Au islands after an annealing step at high temperature. The average diameter of patterned islands are 180 nm, 270 nm, and 360 nm, corresponding to the thickness of sputtered Au layer of 10 nm, 18 nm and 24 nm, respectively, whereas, the remaining part (without covering S1805) was dewetted into random Au islands with much smaller size. The average island diameter and the interparticle distance show a

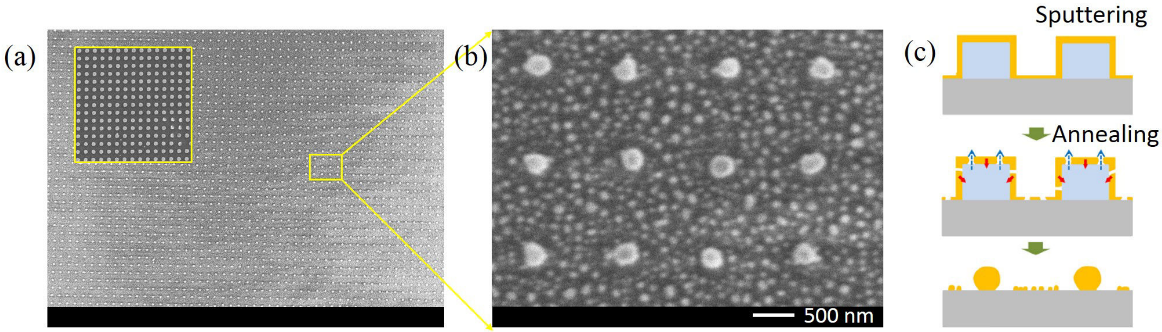

Figure 5.11: (a), (b): SEM images of Au structure fabricated by a combination of DLW and thermal annealing. Inset in (a) shows a SEM image of corresponding photoresist template coated with a sputtered Au layer. (c) Illustration of mechanism explaining the formation of Au arrays.

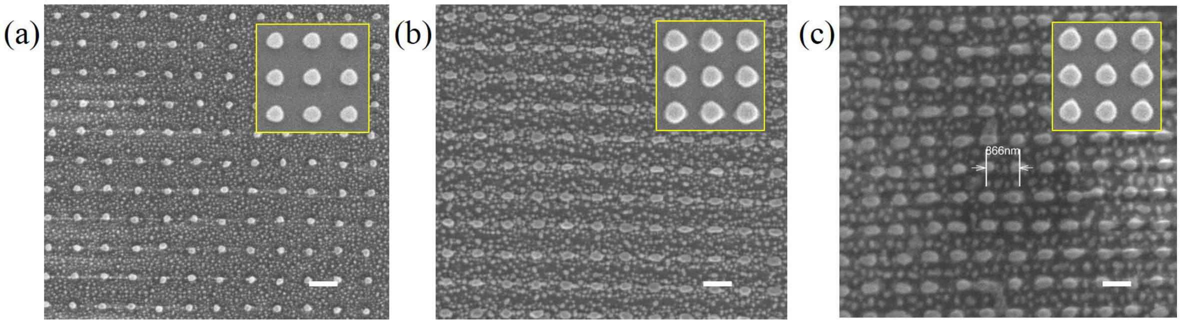

Figure 5.12: SEM images of GNIAs fabricated by thermal annealing of S1805 templates sputtered Au layers of various thicknesses: (a) 10 nm, (b) 18 nm, (c) 24 nm. Insets show the S1805 templates. The scale bar is 0.8 μm.

general tendency to increase as the Au thickness become larger, while the fraction of the area covered by islands and the number of particles per unit area decrease. That suggests to control the thickness of sputtered Au layer in order to control the number of Au NPs per a unit cell of lattice.

5.3.2.3 Influence of template filling factor on the formation of GNIA

The samples of the S1805 templates with a period of 0.6 μm were fabricated with different doses on the area of 100 × 100 (μm) for each. SEM images of these templates are shown in figures 5.13(a-d). The templates were then covered by Au layers with a thickness of 10 nm and annealed at 500°C. Figures 5.13(e-h) show SEM images of GNIAs obtained after annealing of as-sputtered templates (figures 5.13(a-d)), respectively. It is confirmed again that the S1805 nodes were converted into GNIAs. As we see in figures 5.13(e-h),

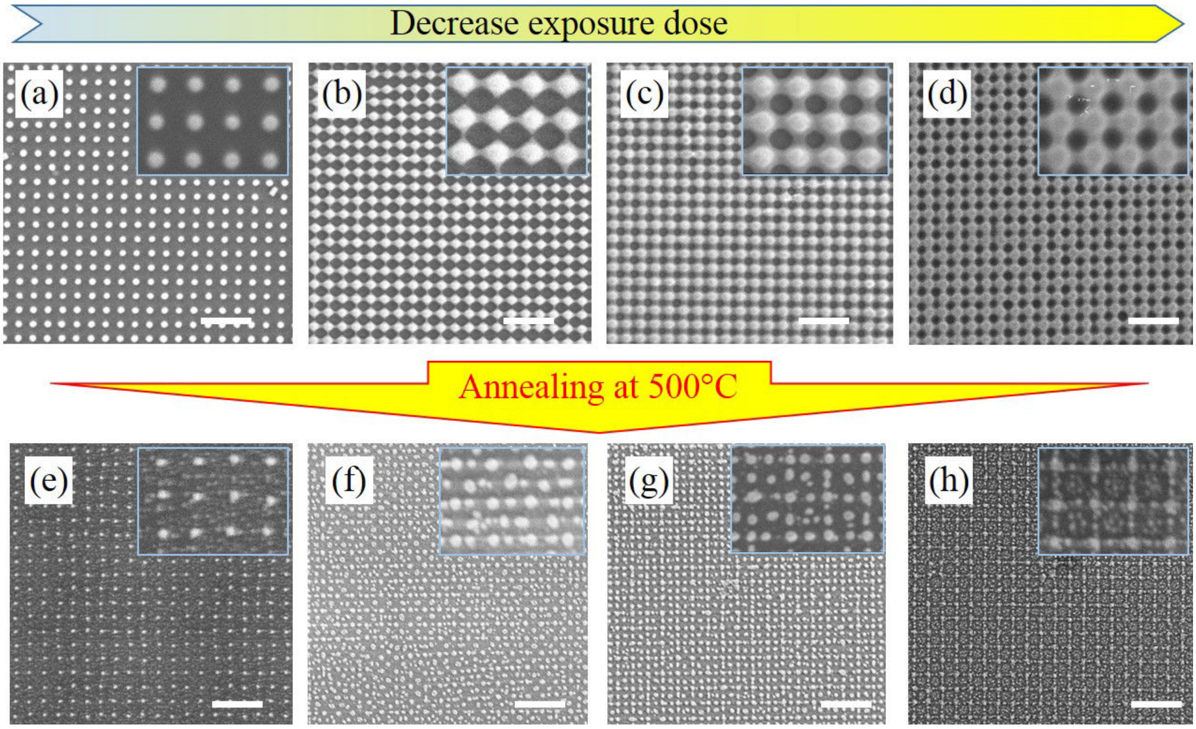

Figure 5.13: (a)-(d) SEM images of template structures (period = 0.6 μm) fabricated with various filling factors and sputtered with a 10 nm Au layer. (e)-(h) Corresponding GNIA structures obtained after annealing at 500°C. The scale bar is 2 μm.

GNIAs are well arranged at the same positions of S1805 in figures 5.13(a-d). The S1805 template leads to the larger Au nano-islands sizes. When S1805 nodes are connected together (figure 5.13(d), Au nano-islands are also jointed in a similar way. In particular, at a certain filling factor of the S1805 templates (figures 5.13(c)), we obtained GNIAs with a periodicity of a half of that of the S1805 template (figures 5.13(g)). This result is very interesting in order to fabricate plasmonic structure with very small periodicity, which is usually limited by the diffraction limit of the optical system.

Conclusion

In this chapter, we have demonstrated a method for producing Au features at nanometer scale. We first fabricated unpatterned Au NPs on the glass substrate by the conventional thermal annealing process. The experimental characterizations show that the high temperature annealing process melted the sputtered Au films, leading to the formation of isolated Au nano-islands, which exhibit enhanced plasmonic resonance with respect to the initial sputtered films. The factors impacting the properties of Au nano-islands have been reported, they are the substrate, the annealing temperature, and the thickness of the initial sputtered film. In more details, we have seen a moderate red shift of SP band, from 542 nm to 590 nm, when increasing Au thickness from 2 nm to 12 nm. SP bands of a 12 nm Au film are narrower with respect to the increase of annealing temperatures from room temperature to 500°C. Secondly, a novel method combining the DLW lithography, sputtering, and thermal annealing processes for patterning plasmonic Au structures has been proposed. The patterned S1805 photoresist templates were sputtered by Au nanolayers with thicknesses varying from 10 nm to 24 nm, and were then thermally annealed to obtain the final plasmonic structures, Au nano islands being formed at the same position of S1805 of templates resulting in a periodic Au nanostructure. In particular, by controlling the filling factor of S1805 templates, GNIA having a very small periodicity can be obtained. Our approach shows many obvious advantages such as low cost, simplicity, and high-throughput fabrication in comparison with conventional methods. Generally, by using the proposed technique, we are able to fabricate various Au structures in periodic, quasiperiodic, or arbitrary networks with controllable lattice parameters.

Chapter 6

Direct laser writing of desired Au nanostructures via photoinduced thermal effect

6.1 Introduction

Control of SP band wavelength is very important for applications, such as color printing, where tuning of SP band to the visible region is crucial for providing real images [97]. Tuning the SP band of metallic nanostructures has been obtained by various techniques. For example, e-beam lithography and focus ion beam milling provide a good control of the feature size, shape of metallic nanoparticles. However, these techniques are quite complicated and expensive. In contrast, as demonstrated in previous chapters, thermal annealing dewetting method is an excellent way for creation of controllable plasmonic structures. We have presented the tuning of SP wavelength from 540 nm to 590 nm by annealing Au films in an oven at 500°C for 30 minutes. Following the idea of dewetting Au by thermal effect, laser-induced dewetting method has been proposed in recent works [82,85]. This method used a high-power laser to generate heating effect in absorbing metals. The induced temperature can exceed 700K with a pulsed laser [98], which allows the melting of Au film in illuminated areas. This is equivalent to what obtained by the conventional thermal annealing method. The laser dewetting method shows more advantages because it allows creating nanostructures in a selective area, which is unachievable by heating the whole samples in the oven.

In this chapter, we demonstrate a one-step method for fabrication of plasmonic struc-

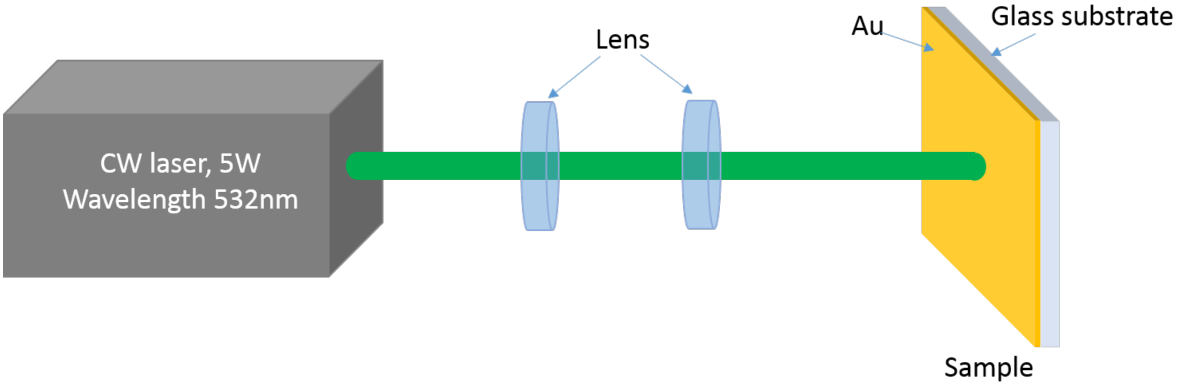

Figure 6.1: Experimental set up of dewetting Au films using a high power cw laser.

tures of Au nanoislands with tunable SP band wavelength by photo-thermal induced DLW technique. We first study Au films annealed by a high power and large laser beam. Then, we investigate the tuning of the SP band of Au structures fabricated by scanning a focused laser beam. Finally, we demonstrate some possibilities of applications, such as data storage and color printing.

6.2 Dewetting of Au film using a 5W cw laser beam

To study the thermal effect generated by the laser-induced dewetting method, we employed a collimated high power laser beam with wavelength of 532 nm. Figure 6.1 depicts the setup of dewetting Au films using a cw high power laser. A 5W cw beam is expanded using two lenses to illuminate the sample of 6 nm-thickness Au thin-film sputtered on a glass substrate. The generated heat induced by strong absorption of illuminated areas melts the Au layer resulting in Au nanoislands with the desired feature size. The morphology transformation leads to a plasmonic band shifting, which was observed by the color change of the Au sample. Initially, the as-sputtered area has a conventional discontinuous morphology, which was well-described in thin film growth Volmer-Weber model for initial growing stages, and exhibits a dark blueish color (figure 6.2(b)). The transmission of as-sputtered area is shown in figure 6.2(d) (black curve). After 30 minutes of exposure to a collimated laser beam, the color of Au thin film changed significantly from blueish to reddish as can be easily seen from the microscope images (figure 6.2(a)). In details, the illuminated structures possessing the reddish color imply the appearance of one or more distinct absorption bands, which is confirmed by UV-Vis spectroscopy measurement shown in figure 6.2(d) (dot-orange curve). This result indicates that the

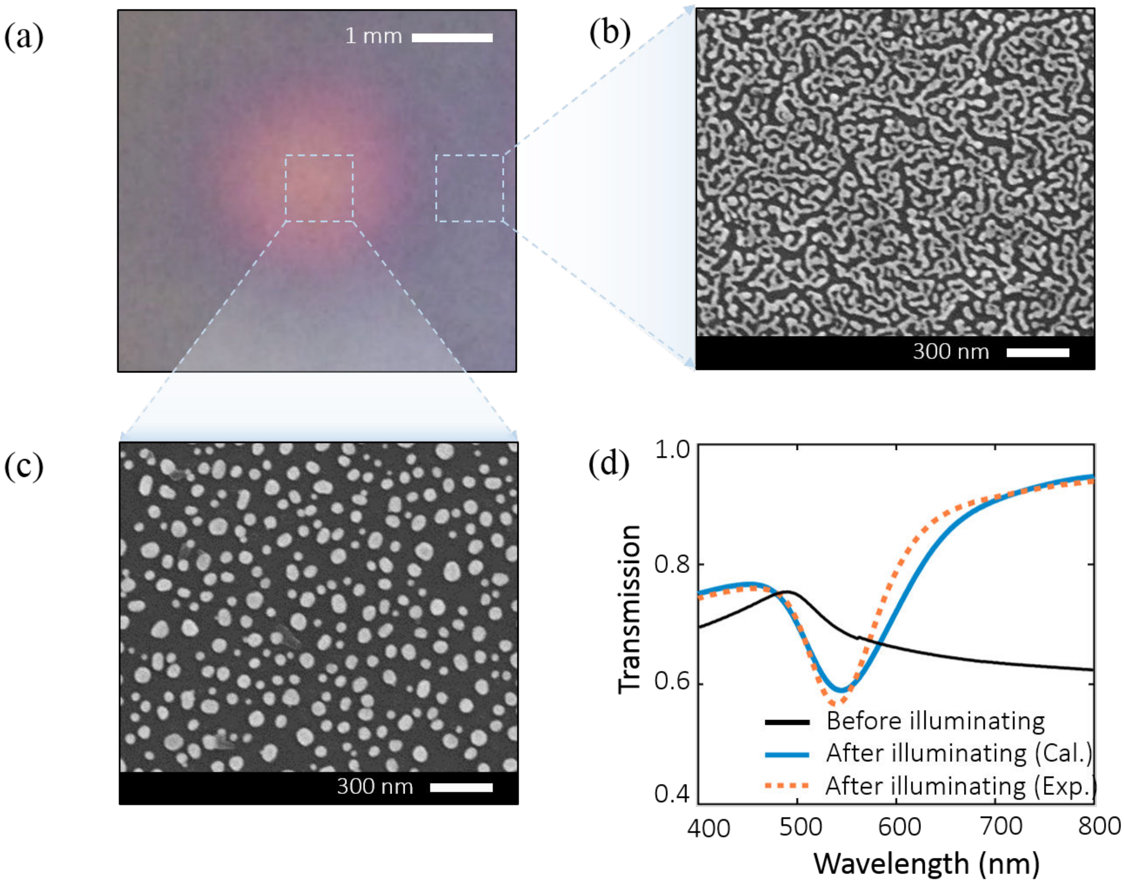

Figure 6.2: Optical microscope (a), and SEM (b-c) images of 6 nm Au island films, sputtered on glass substrate (b) and exposed by 30 minutes with a 5W laser beam (c). (d) Optical transmission of 6 nm Au thin film: no exposure (black); theoretical calculation of exposed area (blue) and experimental measurement of exposed area (dot-orange) of optical transmission of a Au nano island film.

optical response of the sputtered Au structures can be manipulated by laser dewetting process. This great enhancement of plasmonic behavior of exposed samples can be explained by the formation of larger and isolated hummock-like nano-islands (figure 6.2(c)). The measured transmission spectrum is consistent with simulation result performed by finite-difference time domain (FDTD) method (blue curve). The detail of this simulation is reported in Appendix C. In general case, the absorption (Abs) spectra are calculated by measuring the transmission (Tr), reflection (Ref) and scattering (Sc) components as:

$$Abs(\%) = 100 - Ref(\%) - Tr(\%) - Sc(\%). \tag{6.1}$$

Literature reports indicate that, for Au islands with a major axis smaller than 50 nm, the extinction is dominated by the absorption, where the reflection and scattering are ignored [99, 100]. Thus, a 6-nm-Au-thin film dewetted by a high power laser beam possesses SP bands, which are dominated by the absorbance and similar to thermal annealing technique. In next sections, instead of using a large laser beam with high power, we will investigate the dewetting of Au thin films using DLW technique with a focused beam, which allows scalable and precise fabrications of Au nanostructures.

6.3 Direct fabrication of desired Au nanostructures using DLW technique

6.3.1 Fabrication process

To fabricate Au nanostructures by DLW, all samples were prepared in the same way as in previous experiments in chapter 5. Au films were deposited on clean glass substrates (2×2 cm) by magnetron sputtering technique. The thickness of the material layer was highly selected to provide significant surface coverage and to enable the Au dewetting. Two types of Au thin-films with thicknesses of 6 nm and 12 nm were used in this experiment. The samples were moved by a translation stage allowing to realize desired structures. Figure 6.3 illustrates the experimental set up of the dewetting technique using DLW method. In this setup, an air OL (NA = 0.9) and a high power cw laser (λ=532 nm) are used to locally dewet Au films. The focusing laser beam has a diameter of about 350 nm. The translation stage was programmable to control and perform arbitrary trajectories, so specific areas would be dewetted as desired.

6.3.2 Theoretical model of optically induced thermal effect in Au material

In chapter 3, we have shown a simple calculation model of optically induced thermal effect for polymer materials. Similarly, in this chapter, we investigated the heat profile for Au material using the same simulation model. With the high exposure power and the strong absorption of Au material at λ=532 nm, the theoretical calculation of light intensity distribution at the focal region of a high NA OL and the corresponding heat distribution inside material were realized along the x- and y–axes. Optically induced thermal effect on Au materials is a short thermalization effect, which mainly determines the

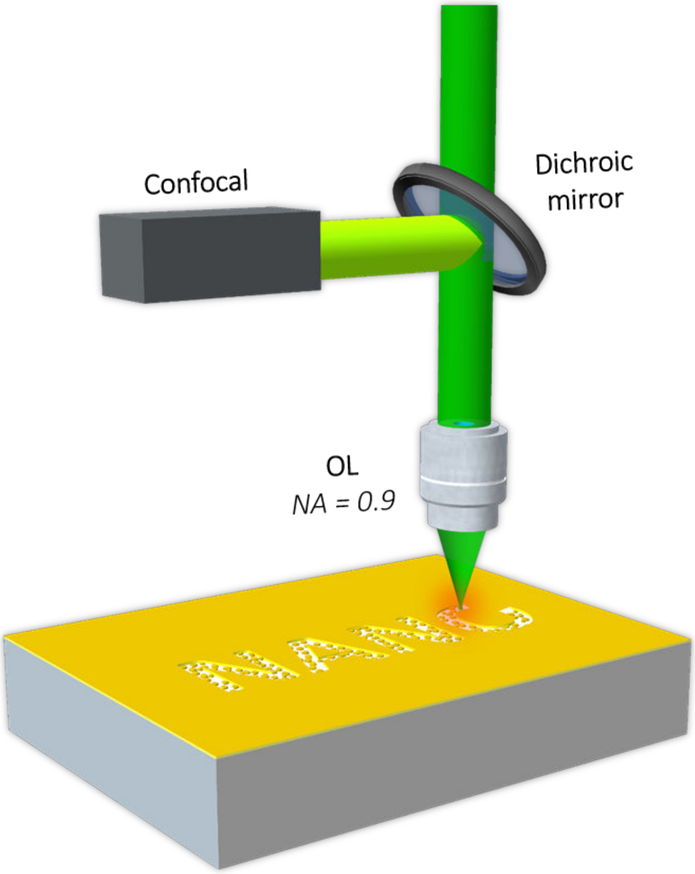

Figure 6.3: Experimental set up of DLW technique used to directly create Au nanostructures by local dewetting effect.

throughput in further applications. Figure 6.4 shows a simulation result of the temporal evolution of the temperature induced in an Au film when irradiated by a laser power of 40 mW. The surface temperature increases instantaneously upon irradiation, and quickly saturates after 100 ps. The result suggests that there is no delay in the writing process allowing a rapid formation of desired plasmonic structures. The optical distribution and the corresponding induced temperature became stable after 100 ps of exposure time. As can be seen in figure 6.5(a), the peak temperature can reach approximately 500°C with an excitation laser power of 40 mW. This high temperature can significantly change the morphologies and optical responses of the Au-thin film [36]. By moving the focusing spot following a desired trajectory, it is possible to create an arbitrary pattern, such as the "NANO" letter shown in figure 6.5(b). Obviously, writing the programmed trajectories by this method is extremely useful for the fabrication of plasmonic micro-devices as

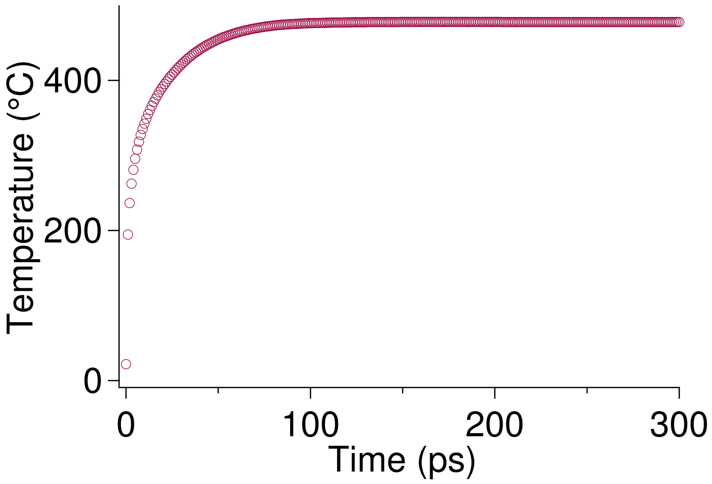

Figure 6.4: Theoretical calculation of the temporal evolution of optically induced temperature for an Au thin film. The laser is on at t = 0 (ps).

compared to annealing the whole sample in an oven [36].

6.3.3 Controlling the morphology of Au nanostructures

In this experiment, we varied some fabrication parameters that have impact on the formation of Au structures, such as scanning velocities. Decreasing the scanning velocity allows to increase the total energy density on illuminated areas resulting in the formation of Au nanoislands with different sizes. First, when the exposure dose was increased, the induced temperature increased accordingly, leaded to the formation of well-separated-Au NPs. However, if the exposure dose increased strongly, the formed-Au NPs were exploded, resulting in very small Au NPs. Figure 6.6 illustrates the dependence of the formation of Au NPs on the exposure dose. The thickness of the sputtered-Au film was 12 nm and the exposure power was 40 mW. The exposure dose was then controlled by the scanning speed of the PZT system. The irradiation at a scanning velocity of 40 μm/s transformed a continuous Au film (before fabrication) into an interconnected network of “nanowires” with an average linewidth of below 100 nm (figure 6.6(a)). When the scanning speed decreased to 20 μm/s, these nanowires were broken up and aggregated into larger but rough and discontinuous structures (figure 6.6(b)). Using scanning velocities lower than 5 μm/s, the experimental results showed the formation of the individual NPs in the spherical or elliptical shape with an average size of about 150 nm. Decreasing the scanning velocity to 2 μm/s induced a micro-explosion of Au NPs into very small individual NPs.

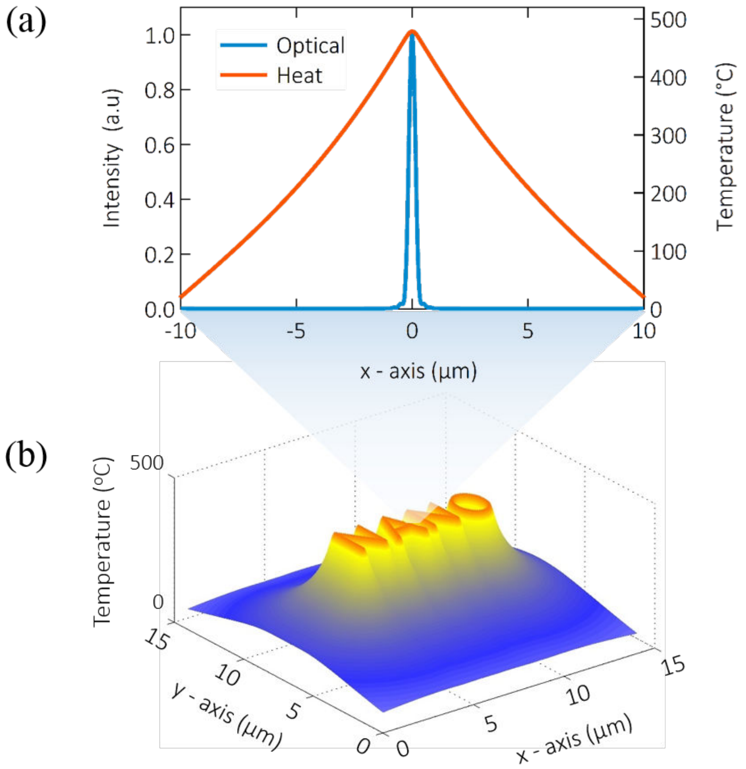

Figure 6.5: Theoretical calculation of light intensity distribution at the focal region of a high NA OL and corresponding heat distribution inside excited material. (a) The simulations were realized along the x–axes with following parameters: $\rho = 0.0193$ kg.m^{-3}, $C_p = 129$ J.kg^{-1}.K^{-1}, $k = 61.9$ W.m^{-1}.K^{-1}, $R_c = 0$, $\mu_{\text{abs}} = 8.83 \times 10^7$ m^{-1}, $S \approx 1.7 \times 10^{17} I_{\text{OPA}}$ W.m^{-3} corresponding to a laser power of 40 mW, and initial temperature of material is 20°C. (b) Simulation of heat distribution in three dimensions for writing a Au film following a trajectory of a "NANO" letter.

This phenomenon was even more pronounced when the scanning velocity was further decreased to 0.5 μm/s. Big Au NPs were almost exploded into small ones with an average size of 20 nm (see in figure 6.6(e)). This phenomenon is explained by the evaporation of Au at their boiling point and their instantaneous reunion after the heat loss. The morphological transformation of Au nanostructures is illustrated in figure 6.6, below each SEM image, respectively. When further decreasing the Au-thin-film thickness to 6 nm, we have obtained Au NPs with smaller size with the same illuminated doses. By manipulating the thickness of Au film and controlling the fabrication parameters, we have fully studied the morphology of Au nanostructures by the DLW technique which are important for further development of this method in correlated applications such as

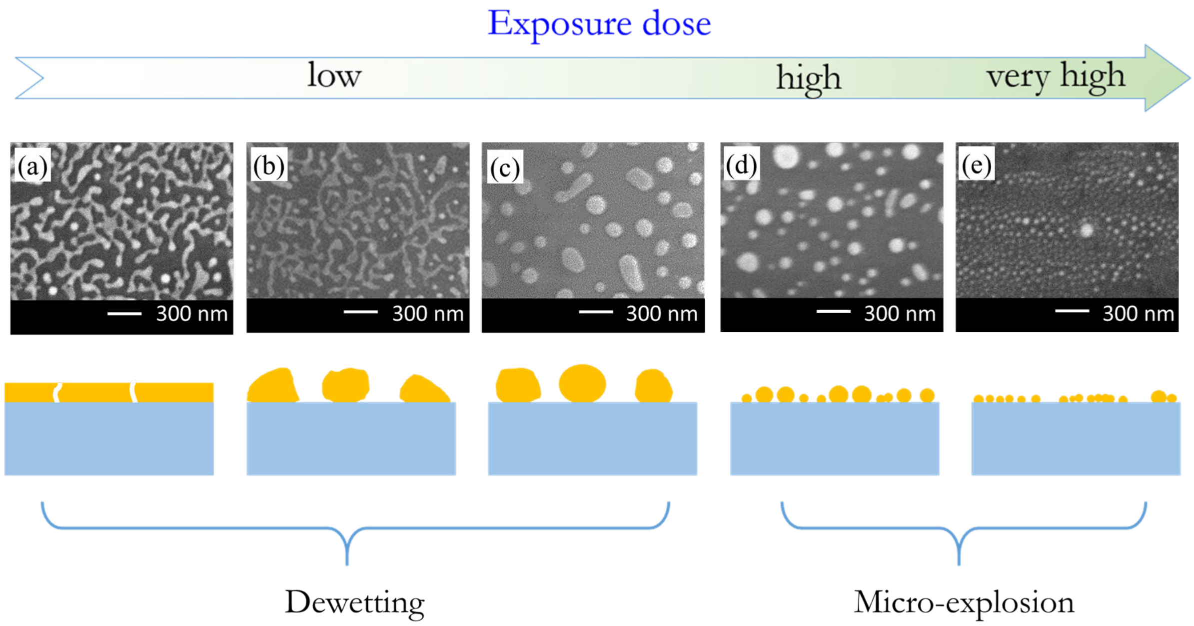

Figure 6.6: Top: SEM images of 12 nm Au island films, sputtered on glass substrate and written by a focused laser beam with 40 mW and different scanning velocities of 40 μm/s (a), 20 μm/s (b), 5 μm/s (c), 2 μm/s (d), and 0.5 μm/s (e). Bottom: Illustrations of Au film morphological transformation as a function of exposure dose.

the tuning of SP band wavelength and color printing.

6.3.4 Tunable SP band of Au nanoisland structures

In the previous part, we have demonstrated the formation of dewetting of Au NPs using the DLW technique. The morphology of fabricated structures has been systematically investigated by manipulating the exposure dose. In this section, we studied the SP band of fabricated Au structures and the ability to tune the SP band within visible range for some specific applications.

To demonstrate the influence of the exposure time on the optical response of fabricated structures, series of Au 6 nm-thickness patterns were written by scanning the laser beam with various time durations. The film thickness of 6 nm was chosen due to its better optical response. Actually, it shows a higher transmission rate as compared to that obtained with the Au sample of 12-nm thickness. Figure 6.7 shows the microscope images (a) and optical transmission spectra (b) of Au island structures obtained by different exposure times of 50 s, 65 s, 80 s, and 100 s, respectively. The transmission spectra

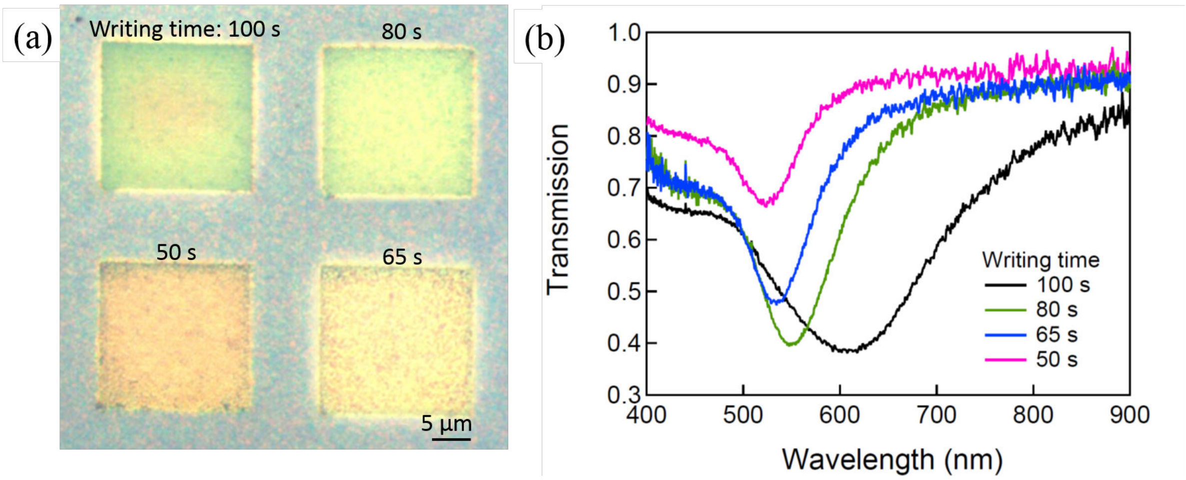

Figure 6.7: Optical microscope image (a) and optical transmission spectra (b) of Au island films (6 nm-thickness), sputtered on glass substrate and written at laser power of 40 mW on the areas of 20×20 μm at different exposure times: 100 s, 80 s, 65 s, and 50 s.

were obtained with a homemade setup, in which the light was guided to transmit through the structures by an objective lens and collected by a spectrometer. Au patterns with different colors are originating from Au NPs with various sizes and different distributions within illuminated areas. The Au nanoislands having smaller size result in the stronger induced LSPR enhancement.

In our case, all fabricated structures show the enhancement of absorption peaks comparing with original as-sputtered-Au layer. The longer exposure time leads to a higher absorption rate and accordingly a lower transmission. Furthermore, we found that those peaks corresponding to different fabrication parameters are remarkable red-shifted, which clarifies the change of the samples color. In particular, when NPs are small and close enough to each other (less than 10 nm), due to the high exposure dose, they start to have mutual interactions. These interactions are generally associated to multipolar effects causing the shift of the SPR to the red and/or to increase the absorption in the infrared part of the spectrum. Its mechanism related to mutual interactions are well-defined in literature [104–106]. In this experiment, when we increased the exposure time from 50 s to 100 s, the SP peaks shifted considerably from 521 nm to 613.4 nm. This result proves that by simply controlling the exposure time, it is possible to tune the SP bands of the plasmonic structures, which can be interesting for a number of applications.

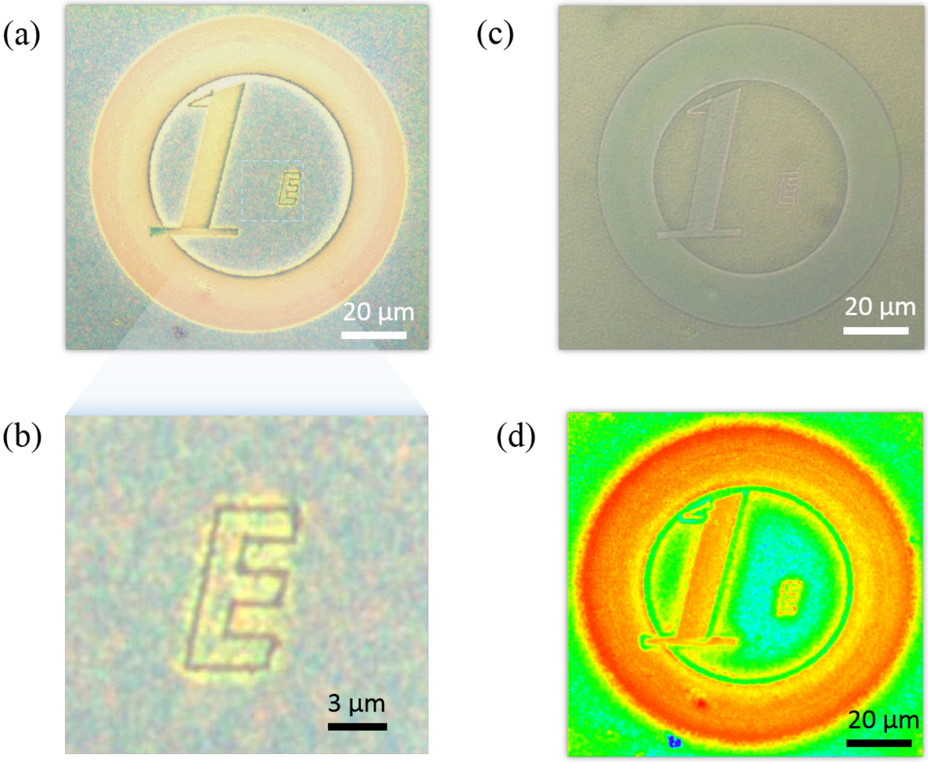

Figure 6.8: Optical microscopic images (a) reflection, (b) zoom in of E letter, (c) transmission. (d) Scanning photoluminescent image.

6.3.5 Color printing and data storage applications

Recently, color printing at microscale has been received a great attention to produce images with better quality. Hence, it is interesting to decrease the size of image sensors and color pixels to the micrometer scale. The current technology still presents some limitations such as shrinking in pixel size and low resolution [20]. Plasmonic color is now a novel solution for imaging technologies. For that, a specific arrangement of metal NPs can form an area of desired color. By using plasmonic effect, pixel size can reach submicroscale, which is interesting for further development of color printing and data storage applications.

Thanks to the flexibility and versatility of the laser induced local thermal dewetting method, it is possible to write structures at high level of complexities. To demonstrate this idea, we realized an example of "1-euro" coin pattern (see figure 6.8(a)). By this way, stereoscopic images can be encoded in the nanostructures and potentially used as elements for data storage applications, even though the resolution of the read-out equipment would ultimately limit their storage capacity. The stored data can be coded

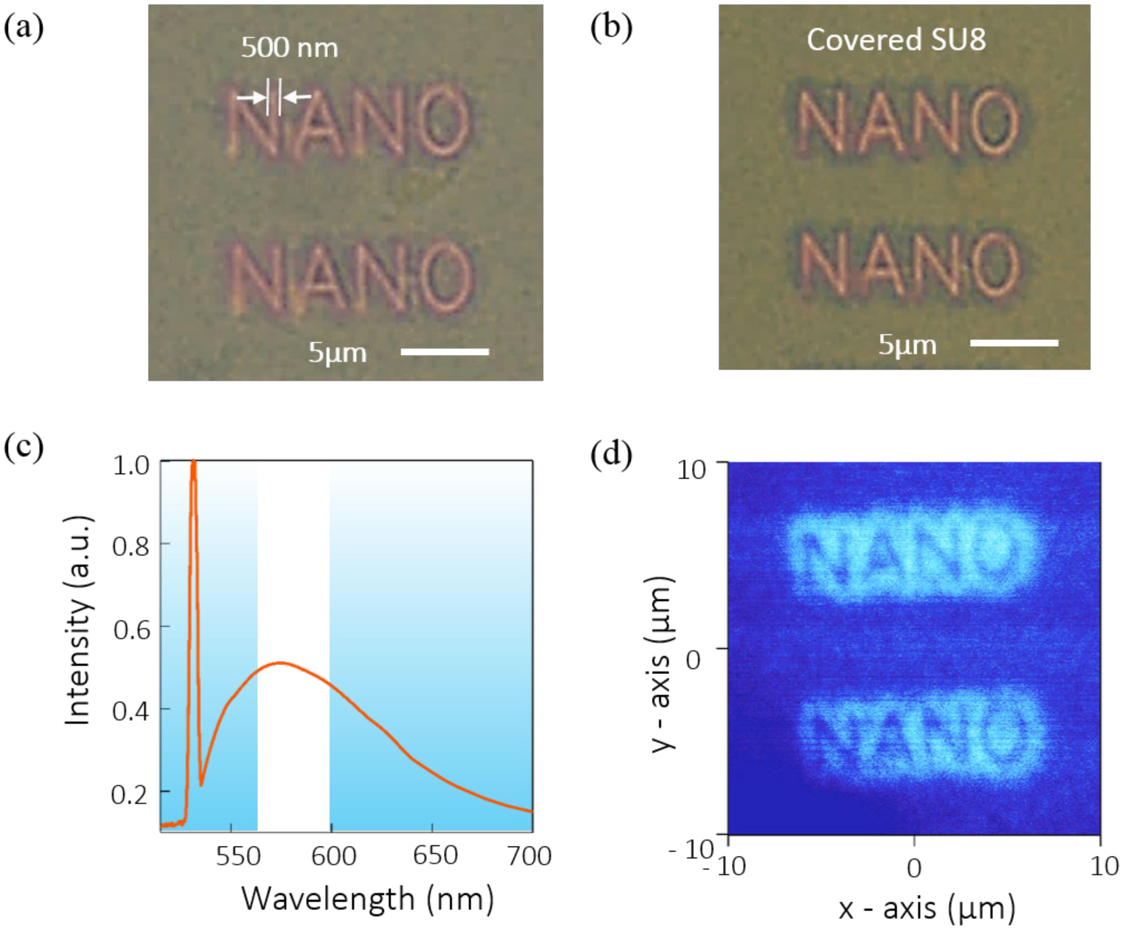

Figure 6.9: Images of a plasmonic pattern of NANO letters before (a) and after (b) protected by SU8 negative photoresist. (c) The fluorescent spectrum of Au NPs with the size of 50 nm. (d) Scanning fluorescent image of a pattern of "NANO" letters.

(binary code, alphabet letter, etc.) and programmed into the trajectory of laser scanning, so that to directly write data on metallic materials. Figure 6.8(b) demonstrates a letter "E" at microscale as an example of writing data on Au layer.

There are many strategies to retrieve the written data stored on Au layer. The simplest method is using optical microscopy techniques. By using transmission/reflection optical microscopes, we can easily track out the information embedded as the shape and the color of patterns (figures 6.8(a-c)). Another reading scheme is collecting photoluminescence of Au nanostructures using the confocal setup, which can be readily combined with DLW setup (figure 6.3). The photoluminescent image of "1 euro" coin is shown in figure 6.8(d).

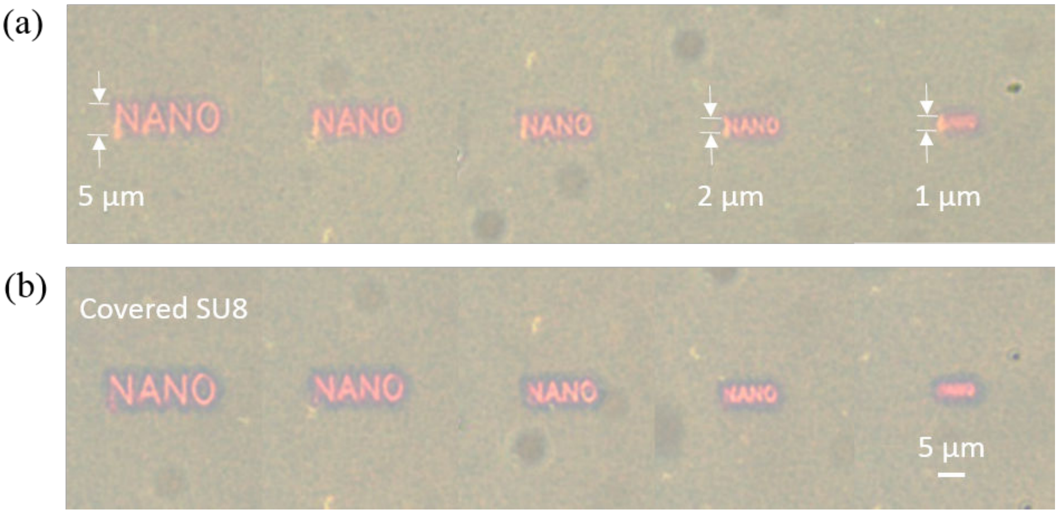

Figure 6.10: Optical microscope transmission images of Au letter structures (a) without covering SU8 and (b) with covering SU8. The NANO letter was written with an average velocity of 5 μm/s and by a laser power of 40 mW , Au film thickness is 6 nm.

As a result of the alteration of sizes and shapes between unwritten and written patterns, Au nanostructures in corresponding areas exhibit different fluorescence signals and spectra [107]. A typical 50 nm-size Au grain was pumped at λ= 532 nm, then emitted spectrum as shown in figure 6.9(c). Hence, by pumping with much lower laser intensity (than in the writing process) and using an appropriated dichroic mirror, we can scan the whole structures and map the emitted rate at every point. This mapping process allowed us not only to reconstruct the patterns, but also provided quantitative knowledge of grain sizes and density of Au constituents, which cannot be accessed by optical microscopy. For example, figure 6.9(d) shows fluorescent mapping of the same structures in figure 6.9(a). The black fringe around the written "NANO" has a level significantly lower than of emitting light. This phenomenon can be explained by the material ablation of laser, in which the materials in the center are expelled in two sides and left smaller grains which have an absorption peak out of the excitation range. Nevertheless, it still exists difficulties to track out the information from small fabricated structures (below diffraction limit of the OL) by the same confocal system. This limitation can be partly improved by using a higher NA OL.

In order to improve the robustness and stability, we spin-coated a thin layer of SU8 photoresist on top of written structures. This layer acts as protective layer that isolates the Au pattern from chemical and mechanical agents, meanwhile it does not affect the optical readout scheme due to its transparency (figure 6.9(b)). The most interesting aspect of data storage applications is its capacity, which directly relates to the smallest feature size of encrypted data. In a previous part, we had demonstrated the writing process of a “NANO” letter onto Au-thin film. In this section, we show an example of written structures, characterized by a transmission optical microscope. Experimentally, by optimizing the writing speed and time, we achieved a well-shaped micro-scale of “NANO” letter, with feature size down to 500 nm corresponding to the focusing spot size. The exposed and unexposed areas are very clear and recognizable by their different optical responses: the written line shows a reddish color, which is in high contrast with dark background color of unwritten areas. To prove the potentiality of high capacity, series of “NANO” letters were written with different feature sizes to examine the readable smallest structures. Figure 6.10 demonstrates that the smallest letter that could be readable is about of 2 μm in each dimension.

Conclusion of chapter 6

In this chapter, we have investigated a one-step method for the fabrication of plasmonic structures of Au nanoisland films by DLW technique. The optical induced thermal effect is systematically studied by calculating the heat distribution and thermalization time of material. The morphological formation of 6 nm Au film after exposure to a collimated cw 5W laser beam was analysed to demonstrate the great enhancement of plasmonic behaviour. SP peaks appear and show a high contrast compared with unilluminated films. The illuminated structure possesses a reddish color, which is confirmed by a SP band at 545 nm. Then, we demonstrated thermal annealing by a focusing laser beam. Au patterns of 20×20 μm were written at a power of 40 mW at different exposure times of 100 s, 80 s, 65 s, 50 s resulting in the SP peaks at 613.4 nm, 548.5 nm, 530.2 nm, and 521 nm, respectively. The resulting long-shifted SP band wavelength is the prominent outcome of this experiment. The turning of SP band of structures leads to interesting applications, for instance, color printing. Specifically, some structures are color-printed such as “1 Euro” coin, square patterns. Furthermore, we have also considered this technique for data storage applications. With a linewidth of 500 nm, we expect to further study high capacity density data storage applications. Samples were then protected by a layer of SU8, which does not affect the reading process. Series of “NANO” letters were written with different feature sizes to examine the smallest readable structures. These letters as well as data or images can be tracked out by high resolution CCD camera or photofluorescent scanning technique. It is emphasized that writing on Au film by DLW is a nature-friendly and low-cost method. This tuning SP band as well as plasmonic colors open a number of possibility in wide range of applications such as image sensors, pixel color filters in super-resolution cameras or high density data storage [20, 79].

Conclusion and Prospects

In summary, in this work, two classes of artificial structures, PhCs and plasmonics, have been fabricated via LOPA-based DLW for numerous applications.

First, by using low writing intensity (few micro watts/μm^2), the photochemical process deriving from one-photon absorption (OPA) mechanism is dominant whereas the photothermal process is ignored. The structures from negative (air-holes) to positive (polymeric cylinders) forms were theoretically and experimentally demonstrated by using a confocal laser scanning setup employing a continuous-wave laser at $\lambda = 532$ nm and an objective lens with NA $= 0.9$. Many kinds of lattices such as hexagonal, honeycomb and assembled multirings were fabricated. Their photonic band gaps (PBGs) are calculated for low refractive index contrast ($n = 1.6$) using FDTD method. The simulation results showed that TM band gaps exist in lattices consisting of air holes in a polymeric background (honeycomb lattices) or in lattices of air-rings in a polymeric background (assembled multirings lattices). TE band gaps exist in lattices consisting of polymeric cylinders in an air background (honeycomb lattice) or in lattices of polymeric rings in an air background (assembled multirings lattices). As compared with honeycomb lattices, assembled multirings structures were shown to possess larger PBGs. The theoretical results also showed that fabricated polymeric PhCs can exhibit a strong reflection peak in the infrared range, which is very useful for application in telecommunication domain. We believe that our results are important for the fabrication of PhCs based on low dielectric constant materials. Besides, fabricated structures could be used as templates for producing PhCs of higher refractive index materials or plasmonic structures.

Second, by using high writing intensity (few milliwatts/μm^2), the focusing spot induced a local high temperature, above glass-transition temperature, which then thermally activates the crosslinking process of the positive photoresist. The material becomes hardened and unable to be dissolved in a common developer or even in acetone. We have therefore developed a method for the fabrication of multi-dimensional polymeric positive nanostructures using a positive photoresist. This technique is based on the optically induced local thermal effects at the focusing region of the DLW system employing a green continuous laser. The locally induced high temperature (above glass-transition temperature) allowed solidifying (crosslinking) the positive photoresist, resulting in solid "positive" structures. In oder to understand the optically induced thermal effect, the thermal behaviour of S1805 positive photoresist was investigated by using a hotplate for a wide range of temperatures, from room temperature to 500°C. Results showed that S1805 has a crosslinking and glass transition threshold at around 156°C. It becomes insoluble in acetone above this threshold. For optically induced thermal effect, we have also developed a simple heat model to account for heat processes, which occur when S1805 positive photoresist is strongly excited by a focusing laser beam. Experimentally, by optimizing the laser power and the writing speed, a feature size of 57 nm was obtained and 1D structures with a period of 300 nm were achieved. Many 2D structures such as cylinder patterns and "NANO" letters were realized with a feature size down to 195 nm. A series of different 3D structures were also fabricated for the first time with a positive photoresist. These fabricated structures pave the way for many interesting applications.

Third, S1805 templates were used in combination with evaporation techniques to create desired metallic structures. The fabrication processes are described as follows: (1) fabrication of polymeric structures by DLW lithography; (2) an Au layer is then deposited on the polymeric templates by thermal evaporation; (3) the photoresist is removed to obtain metallic structures by lift-off technique (templates fabricated at low writing intensity) or by ultra-sonicating process (templates fabricated at high writing intensity). Many Au nanostructures were fabricated, for example, arrays of Au nanodisks, arrays of Au nanostars. In particular, we investigated in detail the design, fabrication and characterization of Au nano-holes arrays (GNHAs) for refractive index sensor application. The GNHA was first designed and theoretically investigated by FDTD simulation. We then fabricated GNHAs with desired parameters. Namely, patterned photoresists (period = 1 μm, diameter = 400 nm) were fabricated at a high writing intensity via DLW. Then, photoresist templates were covered by a Cr layer of 15 nm and followed by thermal evaporation step to create a Au layer of 50 nm. The samples are stripped off by an ultrasonicating procedure. The transmission of GNHA was measured by a home-made transmission setup, resulted in transmission spectrum consistent with our initial design. We found that surface plasmon polariton bands are particularly sensitive to the surrounding medium. A long-shifted wavelength distance of 185 nm (from 1330 nm to

1515 nm) was obtained as the surrounding media varies from water ($n = 1.33$) to oil ($n = 1.51$), corresponding to 1027 nm RIU^{-1}. This result is very promising for highly sensitive refractive index sensors.

Fourth, we introduced a method for producing Au structures at the nanometer scale. We first fabricated unpatterned Au nanoparticles on the glass substrate by a conventional thermal annealing process. Experimental characterizations show that the high temperature annealing process melted the sputtered Au films, leading to the formation of isolated Au nano-islands, which exhibit plasmonic-enhanced resonance with respect to the initial sputtered films. The factors impacting on the properties of Au nano-islands have been reported, which are the substrate material, the annealing temperature, and the thickness of the sputtered film. For more details, we have seen a moderate red-shift of SP band, from 542 nm to 590 nm, when increasing Au thickness from 2 nm to 12 nm. Secondly, a novel method combining DLW lithography, sputtering, and thermal annealing processes for patterning plasmonic Au structures has been proposed. The patterned S1805 photoresist templates were sputtered with Au nano-layers with a thickness varying from 10 nm to 24 nm. The samples were then thermally annealed to obtain the final plasmonic structures. In particular, by controlling the filling factor of S1805 templates, we obtained a plasmonic structure having a periodicity that is equal to half of that of S1805 template. It was demonstrated that the proposed fabrication method would be very reliable and promising.

Fifth, we have investigated a one-step method for fabricating plasmonic structures of Au nanoisland films by photothermal effect induced by DLW technique. We first demonstrated thermal annealing of a 6 nm Au film by a high power continuous-wave laser beam (beam size = 2 mm). The illuminated metallic area possesses a reddish color, which is confirmed by a SP band at 545 nm. Then we demonstrated a local thermal annealing by a focusing laser beam (beam size = 300 nm). Au patterns of 20×20 (μm) were written at a power of 40 mW at different exposure times of 100 s, 80 s, 65 s, 50 s having the SP peaks at 613.4 nm, 548.5 nm, 530.2 nm, and 521 nm, respectively. We have shown that the control of SP bands can be used for a number of interesting applications. Some color-printed structures, such as "one Euro" coin and square patterns were demonstrated. Furthermore, we have also considered this technique for data storage application, for that we wrote a series of "NANO" letters with different feature sizes and covered them by a SU8-protected layer. These letters were read by a high resolution CCD camera and by a photofluorescent scanning technique. It is emphasized that writing on Au film is nature-friendly and these Au films could be recycled.

Outlooks

The future work can be separated into two directions: optimization of fabrication technique and application of fabricated structures.

For the fabrication of nanostructures: i) By using thermal annealing, metallic structures with a half-period of polymeric templates could be obtained. That allows high-resolution fabrication of plasmonic structure overcoming optical diffraction of the DLW technique. 1D and 2D plasmonic structures should be fabricated and investigated carefully for desired optical properties. ii) We primarily limit our laser fabrication to a positive photoresist and gold materials. However, it is possible to use other materials such as silver or copper as well as hybrid materials (inorganic-polymer, magnetic-polymer composite). Expanding the range of materials will also offer more potential applications. iii) The flexibility of DLW allows not only for printing on the most commonly used glass substrates, but also on optical fibres. Fabrication of photonic structures on an optical fibre may be important for sensors, filters, or optical lens applications.

For applications, further optimization of GNHAs is required to increase the sensitivity for refractive index sensor application. Silver materials should be used for full-color printing because silver has SP bands covering the visible wavelength range. 1D, 2D and 3D PhC structures need to be optimized for application in optics such as mirrors and microcavities.

Appendices

Appendix A

The PSF of high NA OLs

The point spread function (PSF) properties were calculated for an air OL, (NA=0.9) and an oil OL (NA=1.3) based on vectorial Debye approximation [35]. The results are shown in figure A.1.

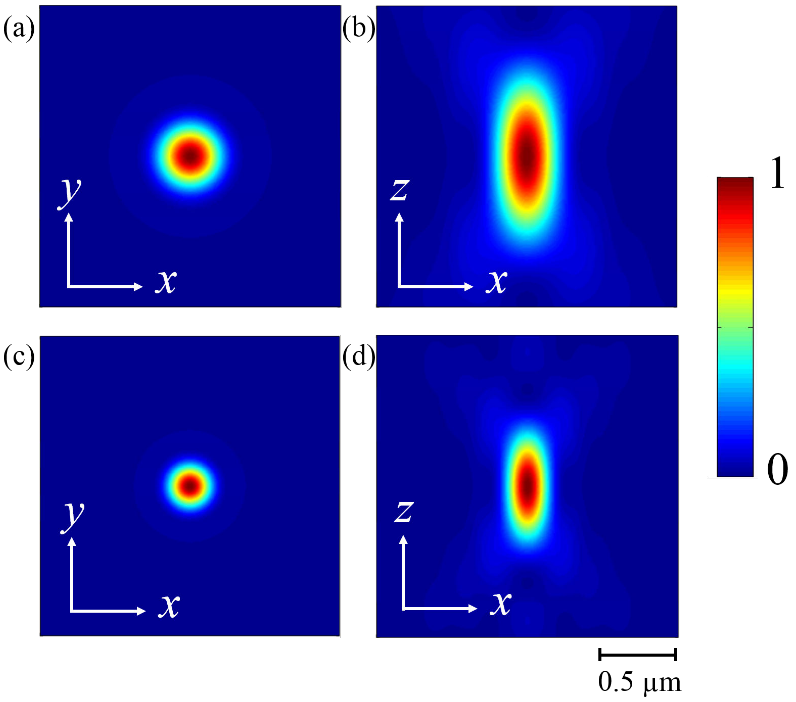

Figure A.1: *The intensity distributions in the focusing region of high NA OL. Results are obtained with* λ *=532 nm. (a,b): OL, NA = 0.9 (air-immersion); (c,d): OL, NA = 1.3 (oil-immersion).*

Appendix B

The calculation of local thermal effect induced by a focused laser beam

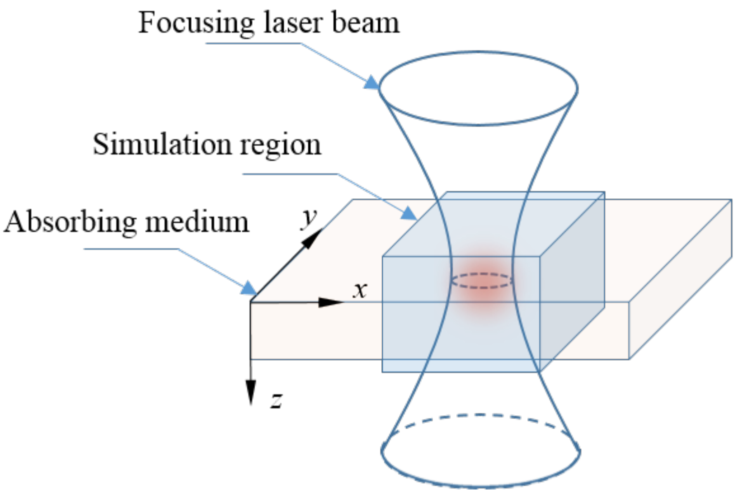

Figure B.1: *Simulation model used to calculate the thermal distribution induced by a focused laser beam inside an absorbing medium.*

Matlab example for simulation of heat intensity distribution inside an absorbing medium.

```
function [Zdata] = pdemodel

[pde_fig,ax]=pdeinit;
pdetool('appl_cb',9);
```

```
set(ax,'DataAspectRatio',[1 1 1]);
set(ax,'PlotBoxAspectRatio',[832 506.25 15892897959.183657]);
set(ax,'XLimMode','auto');
set(ax,'YLim',[-8.6325953417441067e-08 7.7689467766846696e-08]);
set(ax,'XTickMode','auto');
set(ax,'YTickMode','auto');
pdetool('gridon','on');

% Geometry description:
pderect([-5.0000000000000004e-06 5.0000000000000004e-06 5.0000000000000004e-06 -5.0000000000000004e-06],'R1');
pdeellip(0,0,1e-08,1e-08,...
0,'E1');
set(findobj(get(pde_fig,'Children'),'Tag','PDEEval'),'String','R1+E1')

% Boundary conditions:pdetool('changemode',0)
pdesetbd(4,...
'dir',...
1,...
'0',...
'20')
pdesetbd(3,...
'dir',...
1,...
'0',...
'20')
pdesetbd(2,...
'dir',...
1,...
'0',...
'20')
pdesetbd(1,...
'dir',...
1,...
'0',...
'20')

% Mesh generation:
setappdata(pde_fig,'Hgrad',1.3);
setappdata(pde_fig,'refinemethod','regular');
setappdata(pde_fig,'jiggle',char('on','mean',''));
setappdata(pde_fig,'MesherVersion','preR2013a');
pdetool('initmesh')
pdetool('refine')
pdetool('refine')

% PDE coefficients:
pdeseteq(2,...
'k_function(x,y)!k_function(x,y)',...
'0!0',...
'(1e15*heatfunction(x,y))+(0).*(0.0)!(1e15*heatfunction(x,y))+(0).*(0.0)',...
'(1200).*(1200)!(1200).*(1200)',...
'logspace(-2,-1,10)',...
'20',...
```

```
'0.0',...
'[0 100]')
setappdata(pde_fig,'currparam',...
['1200!1200                                    ';...
'1200!1200                                    ';...
'k_function(x,y)!k_function(x,y)              ';...
'1e15*heatfunction(x,y)!1e15*heatfunction(x,y)';...
'0!0                                          ';...
'0.0!0.0                                      '])

% Solve parameters:
setappdata(pde_fig,'solveparam',...
char('0','31056','10','pdeadworst',...
'0.5','longest','0','1E-4','','fixed','Inf'))

% Plotflags and user data strings:
setappdata(pde_fig,'plotflags',[1 1 1 1 1 1 6 1 0 0 0 10 1 0 1 0 0 1]);
setappdata(pde_fig,'colstring','');
setappdata(pde_fig,'arrowstring','');
setappdata(pde_fig,'deformstring','');
setappdata(pde_fig,'heightstring','');

% Solve PDE:
pdetool('solve')

% Change mesh of solutions
[p,e,t,u]=getpetu;
x=linspace(-5e-6,5e-6,10001);y=0;
Zdata = tri2grid(p,t,u(:,10),x,y);

plot(Zdata)
%close all force
```

Appendix C

Theoretical calculation of optical response of Au nanoislands structures

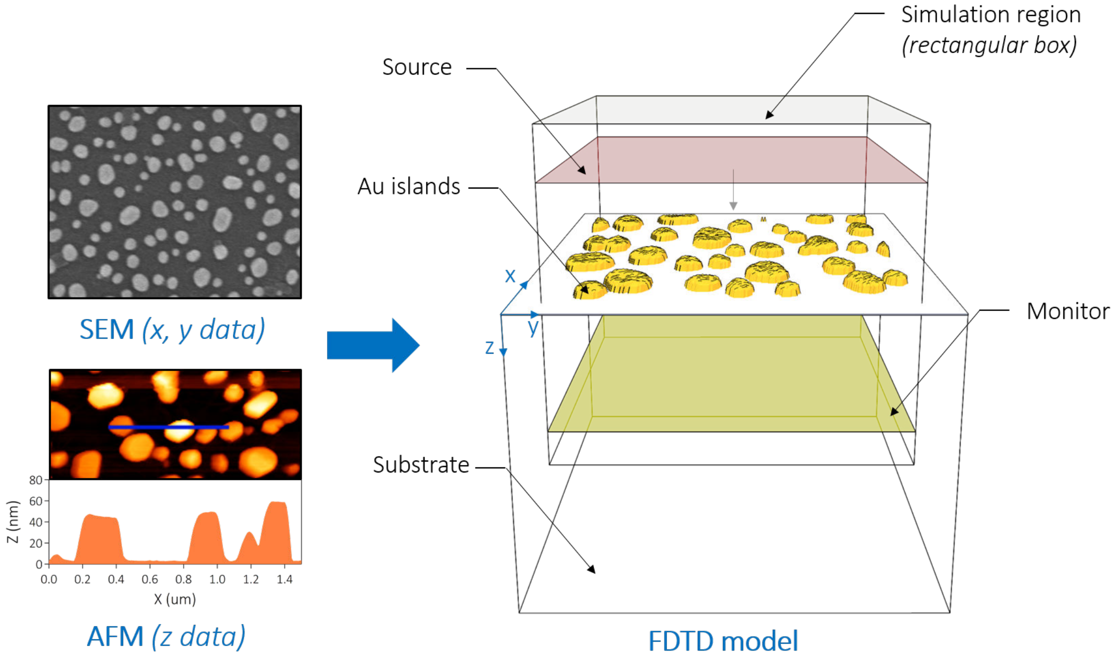

Figure C.1: *FDTD model of Au nano-islands on glass substrate. The Au nano-islands are reconstructed by SEM and AFM data. SEM images provide a large-scale (x,y) data, whilist AFM data is used to estimate the average height of nano-islands.*

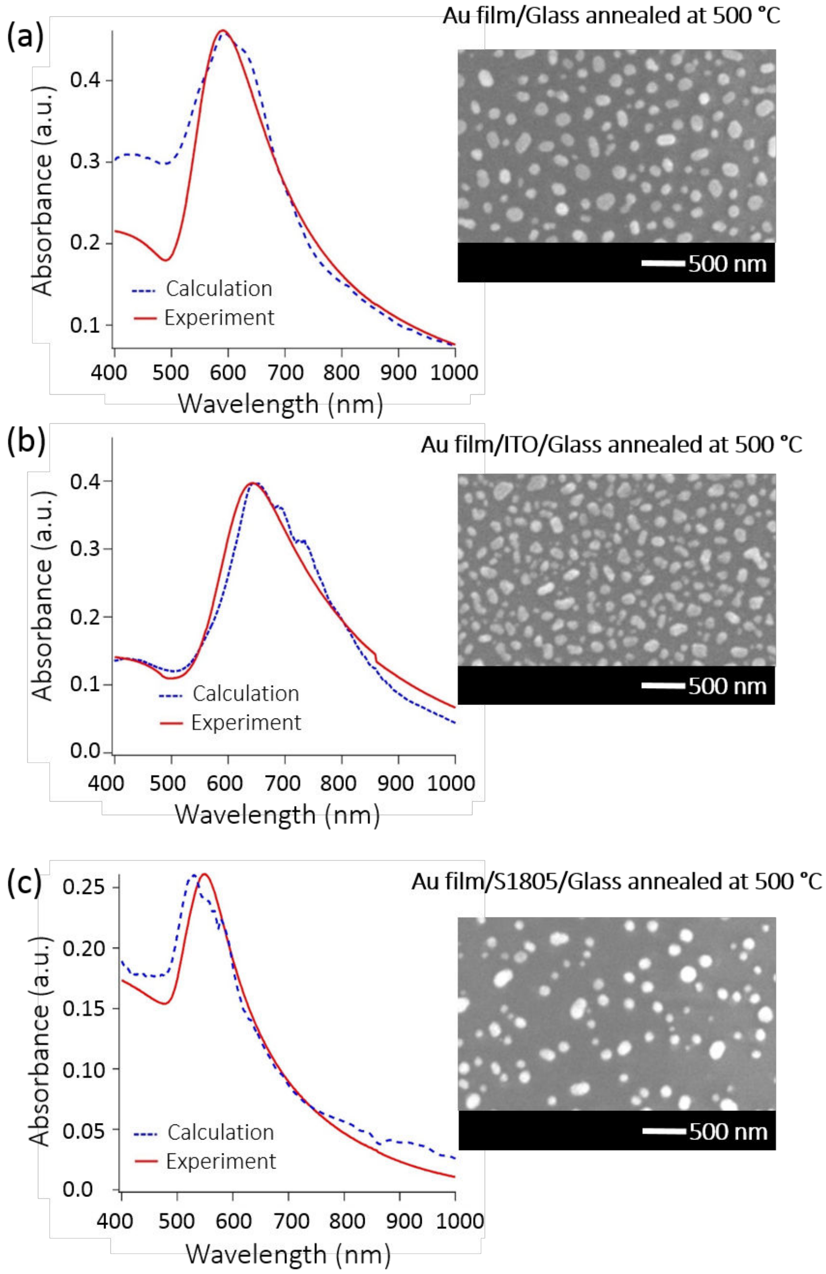

Figure C.2: *Experimental and simulation results of absorbance spectra of Au film structures obtained by thermally annealing Au film sputtered on different substrates: (a) glass, (b) glass coated with ITO, and (c) glass initially coated with S1805 photoresist. The annealing temperature was 500° C.*

Figure C.1 demonstrates the reconstruction of randomly distributed Au NIs in FDTD model. This process required only a SEM image and a AFM image. A 3×4 μm^2 SEM image was utilized to extract the top-view sizes/shapes and (x, y) position coordinates of NIs. This 2D map was then imported and extruded to 3D surface with the estimated height from AFM data. Other FDTD model parameters were set as close to characterization conditions: the optical properties of materials were taken from [71] (SiO_2 substrate) and [72] (Au thin films). The simulation area is bounded in $x-$ and $y-$directions by parallel planes in which periodical boundary conditions are defined, while top and bottom boundaries apply PML BCs to prevent any reflections. The absorbance spectra were calculated from Fourier transform time-dependent transmission monitor.

The experimental and simulation results of absorbance spectra of Au film structures annealed at 500°C with respect to with on different substrates are shown in figure C.2.

Bibliography

[1] Decoopman, T., Tayeb, G., Enoch, S., Maystre, D., and Gralak, B., "Photonic Crystal Lens: From Negative Refraction and Negative Index to Negative Permittivity and Permeability," *Physical Review Letters* **97**, 073905 (Aug. 2006).

[2] Solli, D. R., McCormick, C. F., Chiao, R. Y., and Hickmann, J. M., "Photonic crystal polarizers and polarizing beam splitters," *Journal of Applied Physics* **93**, 9429–9431 (June 2003).

[3] Russell, P., "Photonic Crystal Fibers," *Science* **299**, 358–362 (Jan. 2003).

[4] Kosaka, H., Kawashima, T., Tomita, A., Notomi, M., Tamamura, T., Sato, T., and Kawakami, S., "Superprism phenomena in photonic crystals," *Physical Review B* **58**, R10096–R10099 (Oct. 1998).

[5] Koshiba, M., "Wavelength Division Multiplexing and Demultiplexing With Photonic Crystal Waveguide Couplers," *Journal of Lightwave Technology* **19**, 1970 (Dec. 2001).

[6] Kim, S., Hadzialic, S., Sudbo, A. S., and Solgaard, O., "Reflectivity and polarization dependence of polysilicon single-film broadband photonic crystal micro-mirrors," *Optics Express* **20**, 6306 (Mar. 2012).

[7] Vahala, K. J., "Optical microcavities," *Nature* **424**, 839–846 (Aug. 2003).

[8] Walther, H., Varcoe, B. T., Englert, B.-G., and Becker, T., "Cavity quantum electrodynamics," *Reports on Progress in Physics* **69**(5), 1325 (2006).

[9] Purcell, E. M., "Spontaneous emission probabilities at radio frequencies," *Physical Review* **69**, 681 (1946).

[10] Painter, O., Lee, R. K., Scherer, A., Yariv, A., O'brien, J. D., Dapkus, P. D., and Kim, I., "Two-dimensional photonic band-gap defect mode laser," *Science* **284**(5421), 1819–1821 (1999).

[11] Soref, R. A. and Little, B. E., "Proposed N-wavelength M-fiber WDM crossconnect switch using active microring resonators," *IEEE Photonics Technology Letters* **10**, 1121–1123 (Aug. 1998).

[12] Chu, S. T., "An eight-channel add-drop filter using vertically coupled microring resonators over a cross grid," *IEEE Photon. Tech. Lett.* **15**, 998–1005 (1997).

[13] Elghanian, R., Storhoff, J. J., Mucic, R. C., Letsinger, R. L., and Mirkin, C. A., "Selective Colorimetric Detection of Polynucleotides Based on the Distance-Dependent Optical Properties of Gold Nanoparticles," *Science* **277**, 1078–1081 (Aug. 1997).

[14] Atwater, H. A. and Polman, A., "Plasmonics for improved photovoltaic devices," *Nature Materials* **9**, 205–213 (Mar. 2010).

[15] Hirsch, L., Stafford, R. J., Bankson, J. A., Sershen, S. R., Rivera, B., Price, R. E., Hazle, J. D., Halas, N. J., and West, J. L., "Nanoshell-mediated near-infrared thermal therapy of tumors under magnetic resonance guidance," *Proceedings of the National Academy of Sciences* **100**(23), 13549–13554 (2003).

[16] Kim, B.-H., Cho, C.-H., Mun, J.-S., Kwon, M.-K., Park, T.-Y., Kim, J. S., Byeon, C. C., Lee, J., and Park, S.-J., "Enhancement of the External Quantum Efficiency of a Silicon Quantum Dot Light-Emitting Diode by Localized Surface Plasmons," *Advanced Materials* **20**, 3100–3104 (Aug. 2008).

[17] Yang, K. Y., Choi, K. C., and Ahn, C. W., "Surface plasmon-enhanced spontaneous emission rate in an organic light-emitting device structure: Cathode structure for plasmonic application," *Applied Physics Letters* **94**, 173301 (Apr. 2009).

[18] Cao, L., Barsic, D. N., Guichard, A. R., and Brongersma, M. L., "Plasmon-Assisted Local Temperature Control to Pattern Individual Semiconductor Nanowires and Carbon Nanotubes," *Nano Letters* **7**, 3523–3527 (Nov. 2007).

[19] Xie, Z., Yu, W., Wang, T., Zhang, H., Fu, Y., Liu, H., Li, F., Lu, Z., and Sun, Q., "Plasmonic Nanolithography: A Review," *Plasmonics* **6**, 565–580 (Sept. 2011).

[20] Dean, N., "Colouring at the nanoscale," *Nature Nanotechnology* **10**, 15–16 (Jan. 2015).

[21] Anker, J. N., Hall, W. P., Lyandres, O., Shah, N. C., Zhao, J., and Van Duyne, R. P., "Biosensing with plasmonic nanosensors," *Nature materials* **7**(6), 442–453 (2008).

[22] Rai-Choudhury, P., [*Handbook of microlithography, micromachining, and microfabrication: microlithography*], vol. 1, Iet (1997).

[23] Hohmann, J. K., Renner, M., Waller, E. H., and von Freymann, G., "Three-Dimensional micro-Printing: An Enabling Technology," *Advanced Optical Materials* **3**, 1488–1507 (2015).

[24] Maruo, S. and Fourkas, J., "Recent progress in multiphoton microfabrication," *Laser & Photonics Reviews* **2**, 100–111 (Apr. 2008).

[25] Sekkat, Z. and Kawata, S., "Laser nanofabrication in photoresists and azopolymers," *Laser & Photonics Reviews* **8**, 1–26 (Jan. 2014).

[26] Mueller, P., Thiel, M., and Wegener, M., "3d direct laser writing using a 405 nm diode laser," *Optics Letters* **39**, 6847–6850 (Dec. 2014).

[27] Fischer, B. J., Mueller, J., Quick, S. A., Kaschke, J., Barner-Kowollik, C., and Wegener, M., "Exploring the Mechanisms in STED-Enhanced Direct Laser Writing," *Adv. Optical Mater.* **3**, 221–232 (2015).

[28] Do, M. T., Nguyen, T. T. N., Li, Q., Benisty, H., Ledoux-Rak, I., and Lai, N. D., "Submicrometer 3d structures fabrication enabled by one-photon absorption direct laser writing," *Optics Express* **21**(18), 20964–20973 (2013).

[29] Spagnolo, B., Brunetti, V., Leménager, G., De Luca, E., Sileo, L., Pellegrino, T., Paolo Pompa, P., De Vittorio, M., and Pisanello, F., "Three-dimensional cage-like microscaffolds for cell invasion studies," *Scientific Reports* **5**, 10531 (2015).

[30] Bagheri, S., Weber, K., Gissibl, T., Weiss, T., Neubrech, F., and Giessen, H., "Fabrication of Square-Centimeter Plasmonic Nanoantenna Arrays by Femtosecond Direct Laser Writing Lithography: Effects of Collective Excitations on SEIRA Enhancement," *ACS Photonics* **2**(6), 779–786 (2015).

[31] Del Campo, A. and Arzt, E., "Fabrication Approaches for Generating Complex Micro- and Nanopatterns on Polymeric Surfaces," *Chemical Reviews* **108**(3), 911–945 (2008).

[32] "3d printing on the micrometer scale - Nanoscribe GmbH."

[33] Do, M. T., Li, Q., Nguyen, T. T. N., Benisty, H., Ledoux-Rak, I., and Lai, N. D., "High aspect ratio submicrometer two-dimensional structures fabricated by one-photon absorption direct laser writing," *Microsystem Technologies* **20**(10-11), 2097–2102 (2014).

[34] Cao, H.-Z., Zheng, M.-L., Dong, X.-Z., Jin, F., Zhao, Z.-S., and Duan, X.-M., "Two-photon nanolithography of positive photoresist thin film with ultrafast laser direct writing," *Applied Physics Letters* **102**(20), 201108 (2013).

[35] Li, Q., Do, M. T., Ledoux-Rak, I., and Lai, N. D., "Concept for three-dimensional optical addressing by ultralow one-photon absorption method," *Optics Letters* **38**(22), 4640 (2013).

[36] Do, M. T., Tong, Q. C., Luong, M. H., Lidiak, A., Ledoux-Rak, I., and Lai, N. D., "Fabrication and Characterization of Large-Area Unpatterned and Patterned Plasmonic Gold Nanostructures," *Journal of Electronic Materials* (Jan. 2016).

[37] Kitagawa, J., Kodama, M., and Kadoya, Y., "Design of Two-Dimensional Low-Dielectric Photonic Crystal and Its Terahertz Waveguide Application," *Japanese Journal of Applied Physics* **51**, 062201 (May 2012).

[38] Matthews, A., Wang, X.-H., Kivshar, Y., and Gu, M., "Band-gap properties of two-dimensional low-index photonic crystals," *Applied Physics B* **81**, 189–192 (July 2005).

[39] Fischer, J. and Wegener, M., "Three-dimensional optical laser lithography beyond the diffraction limit," *Laser & Photonics Reviews* **7**, 22–44 (Jan. 2013).

[40] Sakellari, I., Kabouraki, E., Gray, D., Purlys, V., Fotakis, C., Pikulin, A., Bityurin, N., Vamvakaki, M., and Farsari, M., "Diffusion-Assisted High-Resolution Direct Femtosecond Laser Writing," *ACS Nano* **6**, 2302–2311 (Mar. 2012).

[41] Gan, Z., Cao, Y., Evans, R. A., and Gu, M., "Three-dimensional deep sub-diffraction optical beam lithography with 9 nm feature size," *Nature Communications* **4** (June 2013).

[42] Fischer, J., von Freymann, G., and Wegener, M., “The Materials Challenge in Diffraction-Unlimited Direct-Laser-Writing Optical Lithography,” *Advanced Materials* **22**, 3578–3582 (Aug. 2010).

[43] Brown, M. S. and Arnold, C. B., “Fundamentals of laser-material interaction and application to multiscale surface modification,” in [*Laser Precision Microfabrication*], 91–120, Springer (2010).

[44] Bäuerle, D. W., [*Laser Processing and Chemistry*], Springer Science & Business Media (June 2013).

[45] Juodkazis, S., Nishimura, K., Misawa, H., Ebisui, T., Waki, R., Matsuo, S., and Okada, T., “Control over the Crystalline State of Sapphire,” *Advanced Materials* **18**, 1361–1364 (June 2006).

[46] Wu, R., Qiu, X., Zhang, T., Fu, K., and Yang, X., “Atomistic Molecular Insight into the Time Dependence of Polymer Glass Transition,” *The Journal of Physical Chemistry. B* **119**, 9959–9969 (July 2015).

[47] Tillet, G., Boutevin, B., and Ameduri, B., “Chemical reactions of polymer crosslinking and post-crosslinking at room and medium temperature,” *Progress in Polymer Science* **36**, 191–217 (Feb. 2011).

[48] Ebewele, R. O., [*Polymer science and technology*], CRC Press, Boca Raton (2000).

[49] Kuwahara, M., Mihalcea, C., Atoda, N., Tominaga, J., Fuji, H., and Kikukawa, T., “Thermal lithography for 0.1 µm pattern fabrication,” *Microelectronic Engineering* **61–62**, 415–421 (July 2002).

[50] Usami, Y., Watanabe, T., Kanazawa, Y., Taga, K., Kawai, H., and Ichikawa, K., “405 nm Laser Thermal Lithography of 40 nm Pattern Using Super Resolution Organic Resist Material,” *Applied Physics Express* **2**, 126502 (Nov. 2009).

[51] Grupen, M. and Kearfott, K., “Numerical analysis of infrared laser heating in thermoluminescent material layers,” *Journal of Applied Physics* **64**(3), 1044–1049 (1988).

[52] Weiner, A., [*Ultrafast optics*], vol. 72, John Wiley & Sons (2011).

[53] Tseng, A. A., “Recent developments in micromilling using focused ion beam technology,” *Journal of Micromechanics and Microengineering* **14**(4), R15 (2004).

[54] Hicks, E. M., Zou, S., Schatz, G. C., Spears, K. G., Van Duyne, R. P., Gunnarsson, L., Rindzevicius, T., Kasemo, B., and Käll, M., "Controlling Plasmon Line Shapes through Diffractive Coupling in Linear Arrays of Cylindrical Nanoparticles Fabricated by Electron Beam Lithography," *Nano Letters* **5**, 1065–1070 (June 2005).

[55] Guo, L. J., "Recent progress in nanoimprint technology and its applications," *Journal of Physics D: Applied Physics* **37**, R123–R141 (June 2004).

[56] Barbillon, G., Hamouda, F., Held, S., Gogol, P., and Bartenlian, B., "Gold nanoparticles by soft UV nanoimprint lithography coupled to a lift-off process for plasmonic sensing of antibodies," *Microelectronic Engineering* **87**, 1001–1004 (May 2010).

[57] Henzie, J., Lee, J., Lee, M. H., Hasan, W., and Odom, T. W., "Nanofabrication of Plasmonic Structures *," *Annual Review of Physical Chemistry* **60**, 147–165 (May 2009).

[58] Menezes, J. W., Ferreira, J., Santos, M. J. L., Cescato, L., and Brolo, A. G., "Large-Area Fabrication of Periodic Arrays of Nanoholes in Metal Films and Their Application in Biosensing and Plasmonic-Enhanced Photovoltaics," *Advanced Functional Materials* **20**, 3918–3924 (Nov. 2010).

[59] Ebbesen, T. W., Lezec, H. J., Ghaemi, H. F., Thio, T., and Wolff, P. A., "Extraordinary optical transmission through sub-wavelength hole arrays," *Nature* **391**, 667–669 (Feb. 1998).

[60] Martín-Moreno, L., García-Vidal, F. J., Lezec, H. J., Pellerin, K. M., Thio, T., Pendry, J. B., and Ebbesen, T. W., "Theory of Extraordinary Optical Transmission through Subwavelength Hole Arrays," *Physical Review Letters* **86**, 1114–1117 (Feb. 2001).

[61] Barnes, W. L., Dereux, A., and Ebbesen, T. W., "Surface plasmon subwavelength optics," *Nature* **424**(6950), 824–830 (2003).

[62] Genet, C. and Ebbesen, T. W., "Light in tiny holes," *Nature* **445**, 39–46 (Jan. 2007).

[63] Tu, M. H., Sun, T., and Grattan, K. T. V., "Optimization of gold-nanoparticle-based optical fibre surface plasmon resonance (SPR)-based sensors," *Sensors and Actuators B: Chemical* **164**, 43–53 (Mar. 2012).

[64] Iga, M., Seki, A., and Watanabe, K., “Gold thickness dependence of SPR-based hetero-core structured optical fiber sensor,” *Sensors and Actuators B: Chemical* **106**, 363–368 (Apr. 2005).

[65] Slavík, R. and Homola, J., “Ultrahigh resolution long range surface plasmon-based sensor,” *Sensors and Actuators B: Chemical* **123**, 10–12 (Apr. 2007).

[66] Sharma, A. K., Jha, R., and Gupta, B. D., “Fiber-Optic Sensors Based on Surface Plasmon Resonance: A Comprehensive Review,” *IEEE Sensors Journal* **7**, 1118–1129 (Aug. 2007).

[67] Tetz, K. A., Pang, L., and Fainman, Y., “High-resolution surface plasmon resonance sensor based on linewidth-optimized nanohole array transmittance,” *Optics Letters* **31**(10), 1528–1530 (2006).

[68] MacDonald, S. A., Clecak, N. J., Wendt, H. R., Willson, C. G., Snyder, C. D., Knors, C. J., Deyoe, N. B., Maltabes, J. G., Morrow, J. R., McGuire, A. E., and others, “Airborne chemical contamination of a chemically amplified resist,” in [*Advances in Resist Technology and Processing VIII*], 2–12, International Society for Optics and Photonics (1991).

[69] Maier, S. A., [*Plasmonics: fundamentals and applications*], Springer Science & Business Media (2007).

[70] Najiminaini, M., Vasefi, F., Kaminska, B., and Carson, J. J. L., “Nano-hole array structure with improved surface plasmon energy matching characteristics,” *Applied Physics Letters* **100**, 043105 (Jan. 2012).

[71] Palik, E. D., [*Handbook of optical constants of solids*], vol. 3, Academic press (1998).

[72] Johnson, P. B. and Christy, R.-W. *Physical review B* **6**(12), 4370 (1972).

[73] Smith, D., Shiles, E., Inokuti, M., and Palik, E. *Handbook of Optical Constants of Solids* **1**, 369–406 (1985).

[74] Solutions, F., “Lumerical solutions,” *Inc., Vancouver, BC, Canada* (2003).

[75] Tong, Q. C., Nguyen, D. T. T., Do, M. T., Luong, M. H., Journet, B., Ledoux-Rak, I., and Lai, N. D. *Applied Physics Letters* **108**(18), 183104 (2016).

[76] Ozbay, E., “Plasmonics: Merging Photonics and Electronics at Nanoscale Dimensions,” *Science* **311**, 189–193 (Jan. 2006).

[77] Stewart, M. E., Anderton, C. R., Thompson, L. B., Maria, J., Gray, S. K., Rogers, J. A., and Nuzzo, R. G., “Nanostructured Plasmonic Sensors,” *Chemical Reviews* **108**, 494–521 (Feb. 2008).

[78] Yu, J., Dai, G., and Huang, B., “Fabrication and Characterization of Visible-Light-Driven Plasmonic Photocatalyst Ag/AgCl/TiO $_2$ Nanotube Arrays,” *The Journal of Physical Chemistry C* **113**, 16394–16401 (Sept. 2009).

[79] Yokogawa, S., Burgos, S. P., and Atwater, H. A., “Plasmonic Color Filters for CMOS Image Sensor Applications,” *Nano Letters* **12**, 4349–4354 (Aug. 2012).

[80] Kojima, Y. and Kato, T., “Nanoparticle formation in Au thin films by electron-beam-induced dewetting,” *Nanotechnology* **19**, 255605 (June 2008).

[81] Tesler, A. B., Chuntonov, L., Karakouz, T., Bendikov, T. A., Haran, G., Vaskevich, A., and Rubinstein, I., “Tunable Localized Plasmon Transducers Prepared by Thermal Dewetting of Percolated Evaporated Gold Films,” *The Journal of Physical Chemistry C* **115**, 24642–24652 (Dec. 2011).

[82] Rodríguez, C., Peláez, R., Afonso, C., Riedel, S., Leiderer, P., Jimenez-Rey, D., and Font, A. C., “Plasmonic response and transformation mechanism upon single laser exposure of metal discontinuous films,” *Applied Surface Science* **302**, 32–36 (May 2014).

[83] Günendi, M. C., Tanyeli, r., Akgüç, G. B., Bek, A., Turan, R., and Gülseren, O., “Understanding the plasmonic properties of dewetting formed Ag nanoparticles for large area solar cell applications,” *Optics Express* **21**, 18344 (July 2013).

[84] Favazza, C., Kalyanaraman, R., and Sureshkumar, R., “Robust nanopatterning by laser-induced dewetting of metal nanofilms,” *Nanotechnology* **17**, 4229–4234 (Aug. 2006).

[85] Berean, K. J., Sivan, V., Khodasevych, I., Boes, A., Della Gaspera, E., Field, M. R., Kalantar-Zadeh, K., Mitchell, A., and Rosengarten, G., “Laser-Induced Dewetting for Precise Local Generation of Au Nanostructures for Tunable Solar Absorption,” *Advanced Optical Materials* (May 2016).

[86] Doron-Mor, I., Barkay, Z., Filip-Granit, N., Vaskevich, A., and Rubinstein, I., "Ultrathin Gold Island Films on Silanized Glass. Morphology and Optical Properties," *Chemistry of Materials* **16**, 3476–3483 (Sept. 2004).

[87] Golan, Y., Margulis, L., and Rubinstein, I., "Vacuum-deposited gold films," *Surface Science* **264**, 312–326 (Mar. 1992).

[88] Kalyuzhny, G., Vaskevich, A., Schneeweiss, M. A., and Rubinstein, I., "Transmission Surface-Plasmon Resonance (T-SPR) Measurements for Monitoring Adsorption on Ultrathin Gold Island Films," *Chemistry – A European Journal* **8**, 3849–3857 (Sept. 2002).

[89] Karakouz, T., Holder, D., Goomanovsky, M., Vaskevich, A., and Rubinstein, I., "Morphology and Refractive Index Sensitivity of Gold Island Films," *Chemistry of Materials* **21**, 5875–5885 (Dec. 2009).

[90] Ishikawa, T., Mori, K.-i., Ueno, T., Terano, M., and Yoshino, M., "11th International Conference on Technology of Plasticity, ICTP 2014, 19-24 October 2014, Nagoya Congress Center, Nagoya, JapanTemplated Thermal Dewetting Process by Utilizing Nano Plastic Forming Technology," *Procedia Engineering* **81**, 1469–1474 (Jan. 2014).

[91] Farzinpour, P., Sundar, A., Gilroy, K. D., Eskin, Z. E., Hughes, R. A., and Neretina, S., "Altering the dewetting characteristics of ultrathin gold and silver films using a sacrificial antimony layer," *Nanotechnology* **23**, 495604 (Dec. 2012).

[92] Müller, C. M., Mornaghini, F. C. F., and Spolenak, R., "Ordered arrays of faceted gold nanoparticles obtained by dewetting and nanosphere lithography," *Nanotechnology* **19**, 485306 (Dec. 2008).

[93] Siegel, J., Lyutakov, O., Rybka, V., Kolská, Z., and Švorčík, V., "Properties of gold nanostructures sputtered on glass," *Nanoscale Research Letters* **6**, 96 (Jan. 2011).

[94] Lansåker, P. C., Gunnarsson, K., Roos, A., Niklasson, G. A., and Granqvist, C. G., "Au thin films deposited on SnO2:In and glass: Substrate effects on the optical and electrical properties," *Thin Solid Films* **519**, 1930–1933 (Jan. 2011).

[95] Axelevitch, A., Apter, B., and Golan, G., "Simulation and experimental investigation of optical transparency in gold island films," *Optics Express* **21**, 4126 (Feb. 2013).

[96] Couchman, P. R. and Jesser, W. A., "Thermodynamic theory of size dependence of melting temperature in metals," *Nature* **269**, 481–483 (Oct. 1977).

[97] Kumar, K., Duan, H., Hegde, R. S., Koh, S. C. W., Wei, J. N., and Yang, J. K. W., "Printing colour at the optical diffraction limit," *Nature Nanotechnology* **7**, 557–561 (Aug. 2012).

[98] Henley, S. J., Carey, J. D., and Silva, S. R. P., "Pulsed-laser-induced nanoscale island formation in thin metal-on-oxide films," *Physical Review B* **72**, 195408 (Nov. 2005).

[99] Bohren, C. F. and Huffman, D. R., [*Absorption and Scattering of Light by Small Particles*], John Wiley & Sons (Sept. 2008).

[100] Langhammer, C., Kasemo, B., and Zorić, I., "Absorption and scattering of light by Pt, Pd, Ag, and Au nanodisks: Absolute cross sections and branching ratios," *The Journal of Chemical Physics* **126**, 194702 (May 2007).

[101] Hodak, J., Martini, I., and Hartland, G. V., "Ultrafast study of electron–phonon coupling in colloidal gold particles," *Chemical Physics Letters* **284**, 135–141 (Feb. 1998).

[102] Takami, A., Kurita, H., and Koda, S., "Laser-Induced Size Reduction of Noble Metal Particles," *The Journal of Physical Chemistry B* **103**, 1226–1232 (Feb. 1999).

[103] Hashimoto, S., Uwada, T., Hagiri, M., Takai, H., and Ueki, T., "Gold Nanoparticle-Assisted Laser Surface Modification of Borosilicate Glass Substrates," *The Journal of Physical Chemistry C* **113**, 20640–20647 (Dec. 2009).

[104] Jain, P. K. and El-Sayed, M. A., "Surface Plasmon Coupling and Its Universal Size Scaling in Metal Nanostructures of Complex Geometry: Elongated Particle Pairs and Nanosphere Trimers," *The Journal of Physical Chemistry C* **112**, 4954–4960 (Apr. 2008).

[105] Rechberger, W., Hohenau, A., Leitner, A., Krenn, J., Lamprecht, B., and Aussenegg, F., "Optical properties of two interacting gold nanoparticles," *Optics Communications* **220**, 137–141 (May 2003).

[106] Krishna, H., Sachan, R., Strader, J., Favazza, C., Khenner, M., and Kalyanaraman, R., "Thickness-dependent spontaneous dewetting morphology of ultrathin Ag films," *Nanotechnology* **21**(15), 155601 (2010).

[107] Gu, Y., Huang, L., Martin, O. J. F., and Gong, Q., "Resonance fluorescence of single molecules assisted by a plasmonic structure," *Physical Review B* **81** (May 2010).

université
PARIS-SACLAY

ÉCOLE DOCTORALE
Physique et ingénierie : électrons, photons, sciences du vivant (EOBE)

Titre : Étude théorique et réalisation de nanostructures polymères et métalliques par l'écriture directe du point chaud induit optiquement.

Mots clefs : écriture directe par laser, nanostructures, cristal photonique, plasmon de surface, effet thermique photoinduit

Résumé : Ce travail consiste à l'utilisation de la technique d'écriture directe par laser par absorption à un photon pour fabriquer des nanostructures polymères et métalliques en vue d'applications en photonique et en plasmonique. Il est démontré que la température du matériau est augmentée localement et temporellement grâce à une excitation locale d'un laser continue dont la longueur d'onde se situe dans la bande d'absorption du matériau. Un modèle théorique simple a été étudié pour expliquer l'effet photothermique local et temporel, qui est déterminé par le spot de focalisation du système d'écriture directe par laser. En utilisant une résine photosensible positive, il a été démontré que les structures photoniques 1D et 2D peuvent être réalisées avec une taille aussi petite que 57 nm et avec une périodicité aussi courte que 300 nm, ceux qui sont beaucoup plus petites par rapport à la limite de diffraction du système optique utilisé. Les structures photoniques 3D ont également été fabriquées pour la première fois avec une photorésine positive, permettant d'envisager de nombreuses nouvelles applications. Les structures polymères fabriquées ont été démontrées très utiles pour obtenir des nanostructures plasmoniques par soit une combinaison de la méthode d'évaporation thermique d'un film d'or et le procédé lift-off, ou par une combinaison de la méthode de pulvérisation cathodique d'une couche d'or et la méthode de recuit thermique. Les nanostructures d'or fabriquées ont été caractérisées expérimentalement et leurs propriétés optiques ont été théoriquement confirmées par des calculs FDTD. En outre, il a été démontré que les nanostructures d'or, avec les tailles et formes contrôlables, peuvent être réalisées en une seule étape par la technique d'écriture directe par laser grâce à l'effet thermique optiquement induit. Certaines applications de ces nanostructures métalliques sont proposées et étudiées, par exemple, le capteur d'indice de réfraction, le stockage des données et l'impression couleur.

Title : Direct laser writing of polymeric and metallic nanostructures via optically induced local thermal effect

Keywords : direct laser writing, photonic crystal, plasmonic structures, thermal effect, polymer materials

Abstract : This work focuses on the investigation of direct laser writing technique for fabrication of desired nanostructures on positive photoresist and metallic materials. The photothermal and photochemical processes deriving from one-photon absorption mechanism, which occurs when materials are excited by a green continuous-wave laser, enabled a scalable and practical approach for producing nanostructures on demand. A simple heat model was proposed to explain the local and temporal thermal effect, induced by a tiny focusing spot of the direct laser writing system. Using a positive photoresist, it was demonstrated that 1D and 2D photonic structures can be realized with a feature size as small as 57 nm and with a periodicity as short as 300 nm, which are much smaller than the diffraction limit of the used optical system. 3D photonic structures were also fabricated for the first time with a positive photoresist, paving the way to numerous applications. The fabricated polymeric structures have been demonstrated as excellent templates to obtain plasmonic nanostructures by a combination of thermal evaporation of gold film and lift-off process and/or by a combination of the sputtering of a thin gold layer and thermal annealing methods. Fabricated gold nanoarrays were experimentally characterized and their optical properties were theoretically confirmed by FDTD calculations. Furthermore, it was demonstrated that any gold nanostructure, with controllable size and shape, can be realized in one-step by direct laser writing technique thanks to the optically induced thermal effect. Some applications of these metallic nanostructures are proposed, for instance, refractive index sensor, data storage, and color printing.

Université Paris-Saclay
Espace Technologique / Immeuble Discovery
Route de l'Orme aux Merisiers RD 128 / 91190 Saint-Aubin, France

NNT : 2016SACLN073

SYNTHESE EN FRANCAIS DU MANUSCRIT DE THESE

PRÉPARÉE A
L'ECOLE NORMALE SUPERIEURE PARIS-SACLAY

LE LABORATOIRE DE PHOTONIQUE QUANTIQUE ET MOLÉCULAIRE

par

M. Quang Cong TONG

Étude théorique et réalisation de nanostructures polymères et métalliques par l'écriture directe du point chaud induit optiquement.

Thèse présentée et soutenue à ENS Cachan, 13 décembre 2016.

Composition du Jury :

M. BRUNEL Marc	Professeur, Univisité de Rennes 1	Examinateur
M. COOLEN Laurent	MCF HDR, UPMC	Rapporteur
M. SOPPERA Olivier	Directeur de recherche CNRS, Mulhouse	Rapporteur
M. LAI Ngoc Diep	MCF HDR, ENS Cachan	Directeur de thèse
Mme. LEDOUX-RAK Isabelle	Professeur, ENS Cachan	Co-encadrant
M. JOURNET Bernard	MCF, ENS Cachan	Co-encadrant

université
PARIS-SACLAY

ÉCOLE DOCTORALE
Physique et ingénierie :
électrons, photons,
sciences du vivant (EOBE)

Titre : Étude théorique et réalisation de nanostructures polymères et métalliques par l'écriture directe du point chaud induit optiquement.

Keywords : écriture directe par laser, cristaux photoniques, structures plasmoniques, effet thermique, matériaux polymères

Résumé : Ce travail consiste à l'utilisation de la technique d'écriture directe par laser par absorption à un photon pour fabriquer des nanostructures polymères et métalliques en vue d'applications en photonique et en plasmonique. Il est démontré que la température du matériau est augmentée localement et temporellement grâce à une excitation locale d'un laser continue dont la longueur d'onde se situe dans la bande d'absorption du matériau. Un modèle théorique simple a été étudié pour expliquer l'effet photothermique local et temporel, qui est déterminé par le spot de focalisation du système d'écriture directe par laser. En utilisant une résine photosensible positive, il a été démontré que les structures photoniques 1D et 2D peuvent être réalisées avec une taille aussi petite que 57 nm et avec une périodicité aussi courte que 300 nm, ceux qui sont beaucoup plus petites par rapport à la limite de diffraction du système optique utilisé. Les structures photoniques 3D ont également été fabriquées pour la première fois avec une photorésine positive, permettant d'envisager de nombreuses nouvelles applications. Les structures polymères fabriquées ont été démontrées très utiles pour obtenir des nanostructures plasmoniques par soit une combinaison de la méthode d'évaporation thermique d'un film d'or et le procédé lift-off, ou par une combinaison de la méthode de pulvérisation cathodique d'une couche d'or et la méthode de recuit thermique. Les nanostructures d'or fabriquées ont été caractérisées expérimentalement et leurs propriétés optiques ont été théoriquement confirmées par des calculs FDTD. En outre, il a été démontré que les nanostructures d'or, avec les tailles et formes contrôlables, peuvent être réalisées en une seule étape par la technique d'écriture directe par laser grâce à l'effet thermique optiquement induit. Certaines applications de ces nanostructures métalliques sont proposées et étudiées, par exemple, le capteur d'indice de réfraction, le stockage des données et l'impression couleur.

ÉCOLE DOCTORALE
Physique et ingénierie : électrons, photons, sciences du vivant (EOBE)

Title : Direct laser writing of polymeric and metallic nanostructures via optically induced local thermal effect

Keywords : direct laser writing, photonic crystal, plasmonic structures, thermal effect, polymer materials

Abstract : This work focuses on the investigation of direct laser writing technique for fabrication of desired nanostructures on positive photoresist and metallic materials. The photothermal and photochemical processes deriving from one-photon absorption mechanism, which occurs when materials are excited by a green continuous-wave laser, enabled a scalable and practical approach for producing nanostructures on demand. A simple heat model was proposed to explain the local and temporal thermal effect, induced by a tiny focusing spot of the direct laser writing system. Using a positive photoresist, it was demonstrated that 1D and 2D photonic structures can be realized with a feature size as small as 57 nm and with a periodicity as short as 300 nm, which are much smaller than the diffraction limit of the used optical system. 3D photonic structures were also fabricated for the first time with a positive photoresist, paving the way to numerous applications. The fabricated polymeric structures have been demonstrated as excellent templates to obtain plasmonic nanostructures by a combination of thermal evaporation of gold film and lift-off process and/or by a combination of the sputtering of a thin gold layer and thermal annealing methods. Fabricated gold nanoarrays were experimentally characterized and their optical properties were theoretically confirmed by FDTD calculations. Furthermore, it was demonstrated that any gold nanostructure, with controllable size and shape, can be realized in one-step by direct laser writing technique thanks to the optically induced thermal effect. Some applications of these metallic nanostructures are proposed, for instance, refractive index sensor, data storage, and color printing.

Université Paris-Saclay
Espace Technologique / Immeuble Discovery
Route de l'Orme aux Merisiers RD 128 / 91190 Saint-Aubin, France

Titre : Étude théorique et réalisation de nanostructures polymères et métalliques par l'écriture directe du point chaud induit optiquement.

Mots clés : écriture directe par laser, cristaux photoniques, structures plasmoniques, effet thermique, matériaux polymères

Ce travail est consacré à l'étude d'une technique d'écriture directe par laser qui est destinée à la fabrication de nanostructures à la demande, sur résine photosensible et sur matériau métallique. Cette technique s'est basée sur les effets photo-thermiques et photochimiques provenant d'un mécanisme d'absorption à un photon qui a lieu quand les matériaux sont excités par un faisceau laser vert continu. De nombreuses structures polymères sont fabriquées et caractérisées. Ces structures ont un degré de symétrie élevé, permettant d'obtenir une bande interdite photonique, même en cas de faible contraste de l'indice de réfraction. Ces structures polymères sont également démontrées très utiles comme masques/moules pour obtenir des nanostructures plasmoniques par combinaison d'évaporation d'un film d'or et d'un procédé de lift-off et/ou par combinaison de pulvérisation de film d'or et de méthode de recuit thermique. Les nanostructures en or ont été caractérisés après fabrication, et leurs propriétés optiques ont pu être confirmées par simulation FDTD. Par ailleurs il a été démontré que de nombreuses nanostructures

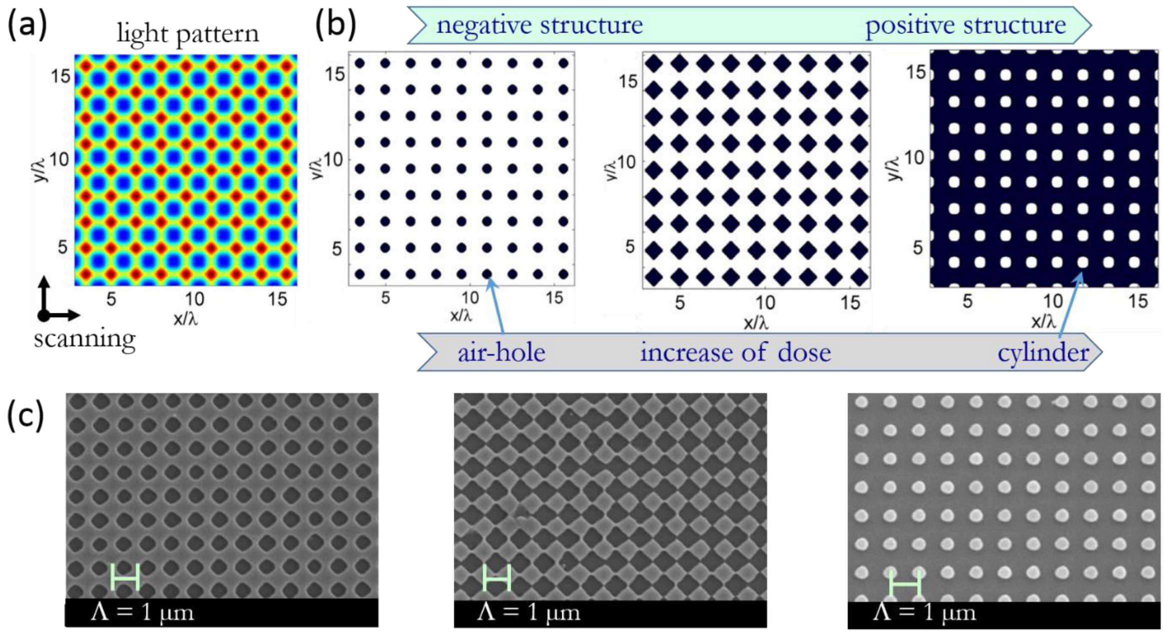

Figure 1. *Fabrication de structures photoniques dans une photorésine positive par la méthode d'écriture directe par laser (NA = 0.9, λ = 532 nm). (a) Modèle théorique d'une structure carrée obtenue par déplacement du spot de focalisation suivant l'axe x et l'axe y. (b) Prédiction théorique des structures ayant de taux de remplissage différents. (c) Images au MEB des structures carrées 2D (période = 1 μm) fabriquées par une puissance fixée à 15 μW et avec des vitesses de déplacement du spot de focalisation différentes, à 10 μm/s, 6 μm/s, et 3 μm/s, respectivement.*

métalliques, de taille et de forme réglable, peuvent être réalisées en une seule étape par une technique d'écriture directe par laser grâce à un effet thermique induit optiquement et localement. Quelques applications de ces nanostructures métalliques sont proposées comme par exemple, des capteurs d'indice de réfraction, le stockage de données et l'impression couleur.

Les résultats principaux sont détaillés comme suit.

En premier lieu, lors d'une écriture directe par un laser continue de faible puissance et à la longueur d'onde λ = 532 nm (figure 1), le processus photochimique provenant de l'absorption à un photon (noté OPA pour "one photon absorption") de la photorésine S1805 (ou S1818) est prépondérant alors que le processus photothermique est négligeable. Les structures quelles soit de type négatif (trous d'air) ou positif (piliers en polymères) ont été démontrées à la fois théoriquement et expérimentalement. Plusieurs types de structures souhaitées, telles que hexagonal, nid d'abeille et multi-anneaux assemblés, ont été fabriqués. Leurs bandes interdites photoniques (PBGs pour "photonic band gaps") ont été calculées pour une valeur faible de l'indice de réfraction (*n* = 1,6) par une méthode FDTD. La simulation montre que des bandes interdites TM existent dans des structures de type trous d'air dans une matrice de polymère (nid d'abeille) ou dans des structures de type anneaux d'air (réseaux multi-anneaux). La figure 2 montre un exemple de structures qui a été fabriquée, ainsi que les résultats du calcul théorique des PBGs pour une structure en nid d'abeille et de type réseau multi-anneaux. Les bandes interdites de type TE existent dans les réseaux constitués de piliers cylindriques en polymères entourés d'air ou dans des réseaux multi-anneaux constitués d'anneaux de polymères entourés

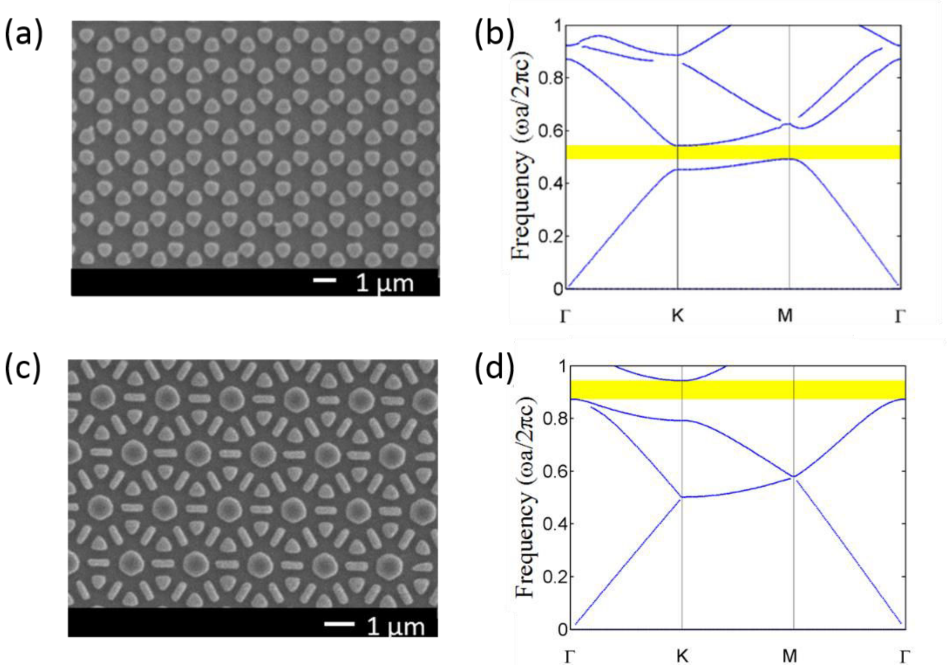

Figure 2. *(a) Image au MEB d'une structure en nid d'abeille (période = 1.5 µm) et (b) résultat théorique de la bande photonique (mode TM) de cette structure, calculé pour le cas du rapport r/a = 0.35, où r est le rayon du pilier polymère et a est la période de la structure. (c) Image au MEB d'une structure d'anneaux assemblés (période = 2 µm) et (d) résultat théorique de la bande photonique (mode TM) de cette structure, calculé pour les paramètres suivants : le rayon de l'anneau r = 1.18 µm, la période de la structure a = 1.5 µm, la largeur de l'anneau = 300 nm. Pour tous les calculs, l'indice de réfraction du matériau est n = 1.6.*

d'air. Il a été montré que les réseaux multi-anneaux ont une bande interdite plus large que les réseaux en nids d'abeille. Nous pensons que nos résultats sont importants quant à la fabrication de cristaux photoniques sur des matériaux à faible indice de réfraction. De plus les structures ainsi fabriquées peuvent être utilisées comme base pour produire des cristaux photoniques à plus fort indice de réfraction ou des structures plasmoniques.

En deuxième lieu, lors d'une écriture directe avec une forte intensité (quelques milliwatts/µm^2), la température induite au point de focalisation devient élevée, supérieure à la température de transition vitreuse, et enclenche le processus de réticulation au sein de la résine photosensible positive. Le matériau durcit et ne peut pas être dissous dans un solvant ordinaire voire dans l'acétone. C'est pourquoi nous avons mis au point une méthode de fabrication de nanostructures polymères multidimensionnelles à partir d'une résine photosensible positive. Cette méthode est basée sur l'effet thermique induit optiquement et localement au point de focalisation par le système d'écriture directe par laser, utilisant un laser continu. La température localement élevée (supérieure au point de transition vitreuse) entraîne la solidification (réticulation) de la résine photosensible créant par là des structures de type positives. Plus précisément le comportement thermique de la photo-résine S1805, a été étudié sur une plage large de la température ambiante jusqu'à 500°C. Les résultats obtenus montrent que la résine S1805 présente une transition

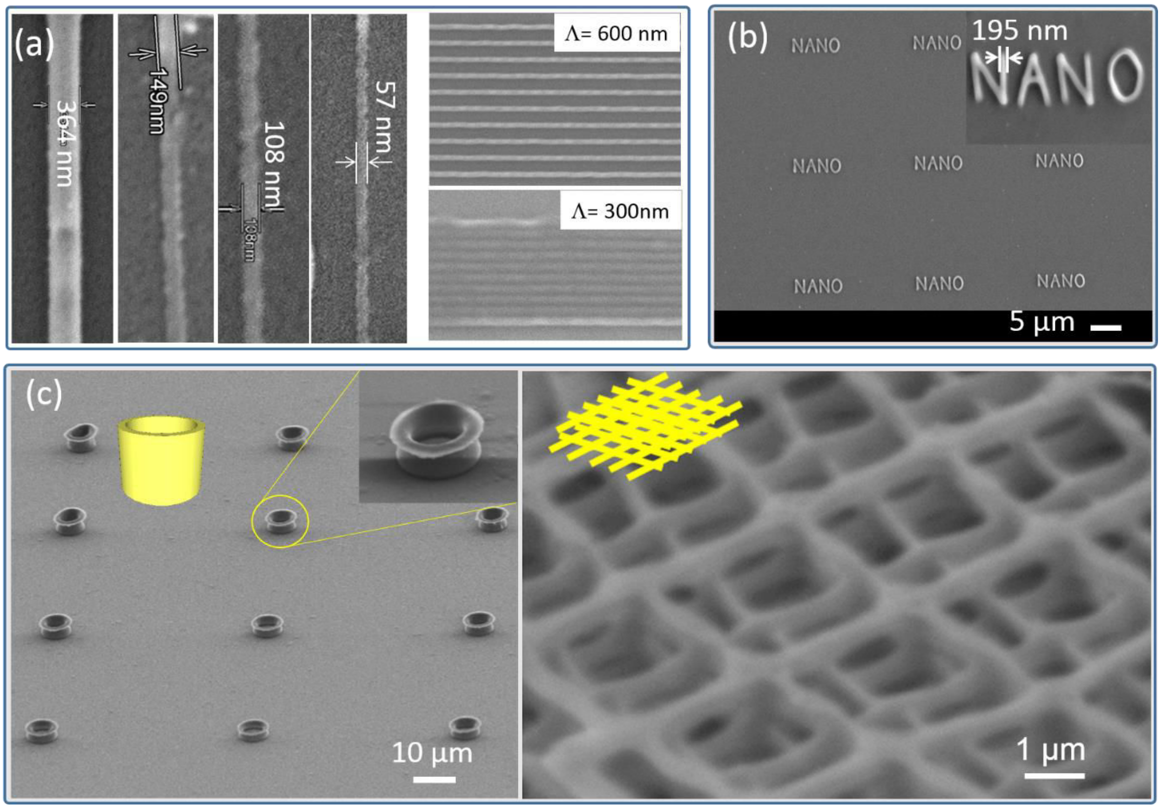

Figure 3. *(a) A gauche : Images au MEB des lignes fabriquées par des puissances différentes: 4, 3, 2.5, et 2 (mW) et par la même vitesse de balayage, 10 µm/s. A droite : Images au MEB des structures 1D ayant des périodes différentes, 0.6 µm et 0.3 µm, respectivement, fabriquées par une puissance de 2 mW et une vitesse de balayage de 5 µm/s. (b) Lettres « NANO » fabriquées par une puissance de 2 mW et une vitesse de balayage 10 µm/s. (c) Images au MEB de structures 3D fabriquées dans la photorésine S1818 (épaisseur = 6 µm). L'encart indique les designs des structures fabriquées.*

vitreuse (réticulation) à environ 156°C. Il devient alors impossible de la dissoudre dans l'acétone. Nous avons donc développé un modèle thermique simple pour prendre en compte ce qui se produit quand la photo-résine positive S1805 est fortement excitée par le faisceau laser bien focalisé. Après optimisation de la puissance du laser et de la vitesse d'écriture, une taille de motifs de 57 nm a été obtenue et des structures 1D d'une périodicité de 300 nm ont été réalisées (figure 3a). Plusieurs structures 2D comme des motifs cylindriques ainsi que les lettres "NANO" ont pu être réalisés avec une taille de 195 nm (figure 3b). Une série de différentes structures 3D a aussi été fabriquée (figure 3c). Ces structures ainsi obtenues ouvrent la voie à beaucoup d'applications intéressantes.

En troisième lieu, les matrices S1805 ont été utilisées en combinaison avec des techniques d'évaporation pour créer des structures métalliques particulières. Le processus de fabrication est décrit ci-dessous.

(1) Fabrication de structures polymères par lithographie écriture laser directe
(2) Une couche d'or est déposée sur la structure polymère par évaporation thermique
(3) La résine photosensible est enlevée par lift-off pour obtenir une structure métallique. Dans le cas d'une structure polymère obtenue par écriture à faible puissance, le lift-off est réalisé par l'immersion de l'ensemble de la structure dans l'acétone. Alors que pour les structures polymères obtenues par écriture à forte puissance, le lift-off est réalisé par la méthode ultrasonique.

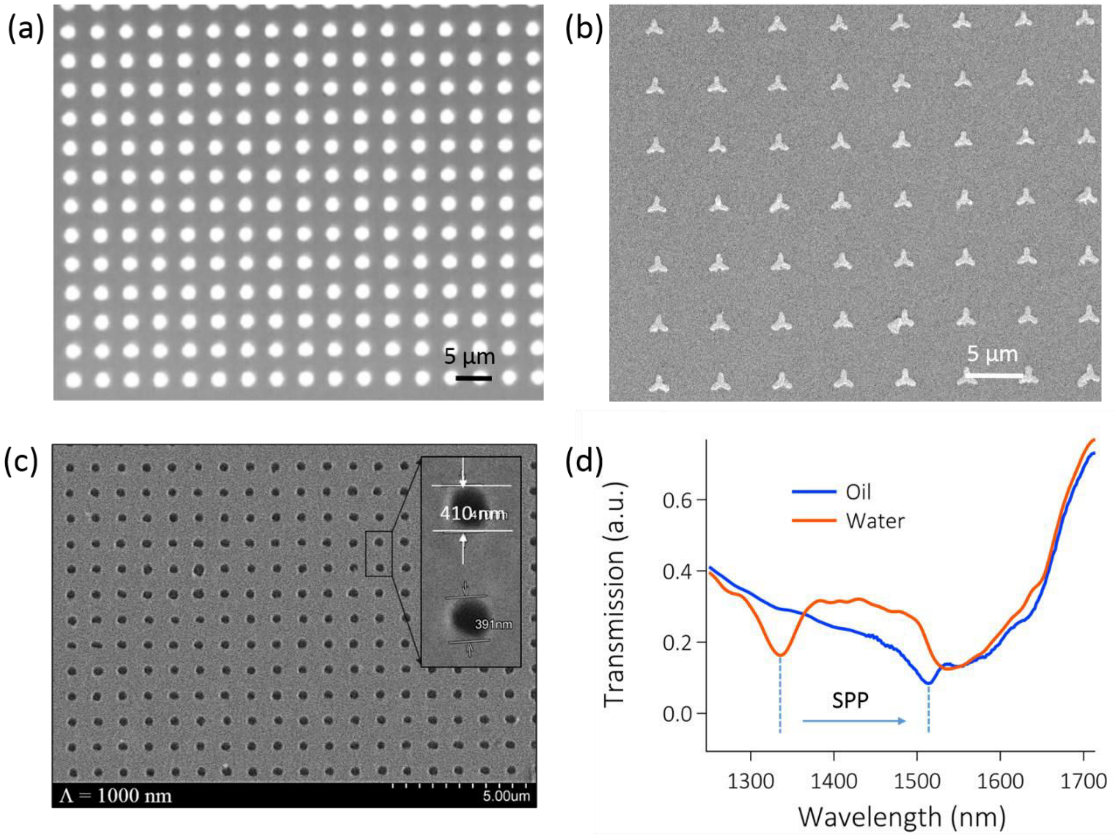

Figure 4. *(a) Image au MEB d'un réseau de disques en or. (b) Image au MEB d'un réseau d'étoiles en or. (c) Image au MEB d'un réseau de nano-trous en or. (d) Spectres de transmission d'une structure GNHA en différents milieux.*

Beaucoup de nanostructures métalliques ont été fabriquées, comme par exemple des réseaux de nano-disques ou de nano-étoiles en or (figures 4a, b). Nous avons en particulier étudié en détail la conception, la fabrication et la caractérisation de réseaux de nano-trous en or (GNHAs pour gold nano holes arrays) destinés à des applications de capteurs d'indice de réfraction. Nous avons tout d'abord conçu et étudié les GNHA par simulation FDTD. Puis nous les avons fabriquées en fonction de ces études préliminaires. Plus précisément les motifs, de période 1 µm et de diamètre 400 nm, ont été écrit avec une intensité élevée (DLW) (figure 4c). Les structures en résine ont tout d'abord été recouvertes d'une couche de chrome de 15 nm pour augmenter l'adhésion entre le film d'or et la substrat. Puis une couche d'or de 50 nm a été déposée par évaporation thermique. Finalement, les structures polymères ont été prélevées par la méthode ultrasonique. La mesure de transmission de telles structures métalliques a été réalisée conduisant à un résultat cohérent avec la première conception. Nous avons observé que les bandes d'absorption de polariton de plasmon de surface étaient très sensibles à l'environnement. Un décalage en longueur d'onde de 185 nm (de 1330 nm à 1515 nm) a été obtenu pour un milieu environnant allant de l'eau ($n = 1.33$) à l'huile ($n = 1{,}51$), correspondant à 1027 nm.RIU^{-1} (figure 4d). Ce résultat est très prometteur pour des applications de capteurs d'indice de réfraction.

En quatrième lieu, nous avons introduit une nouvelle méthode pour produire des nanostructures en or. Tout d'abord nous avons fabriqué des nanoparticules en or distribués aléatoirement sur un substrat de verre par une méthode de recuit thermique conventionnelle. Les caractérisations expérimentales montrent que la température élevée du processus de recuit a fait fondre les films d'or, obtenues par pulvérisation, conduisant à la formation de nano-îlots d'or qui présentent des résonances plasmoniques (figures 5a, b). Les propriétés de ces nano-

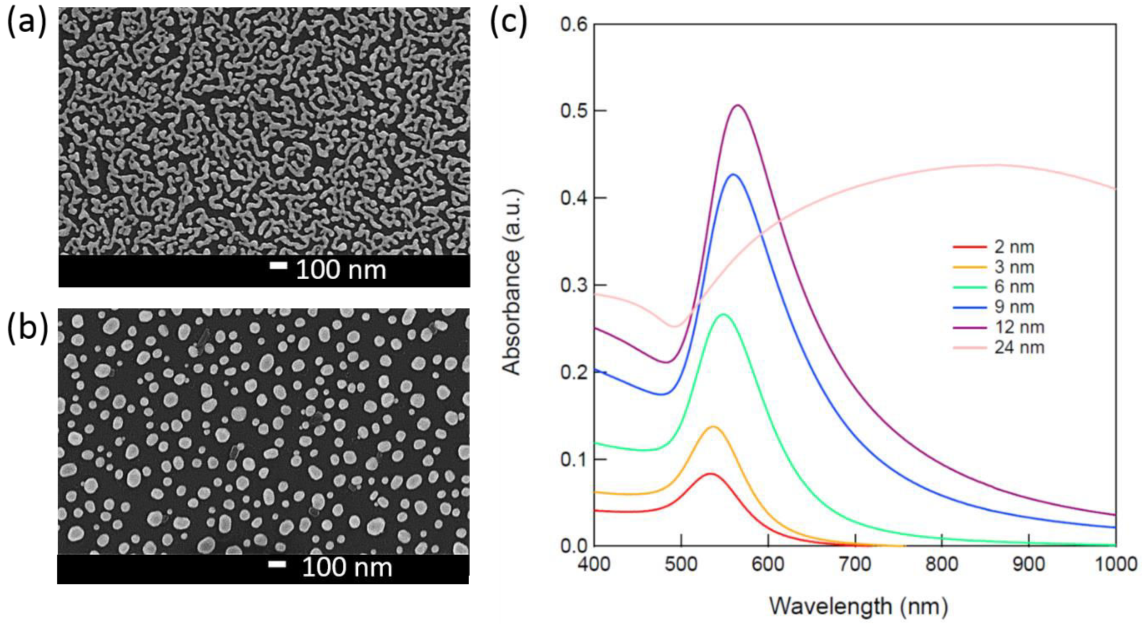

Figure 5. *(a) Images au MEB d'un film d'or de 10 nm obtenu par pulvérisation sur substrat de verre. (b) Le film correspondant après réticulation de 30 minutes à 500°C. (c) Spectres UV-VIS de films d'or de différentes épaisseurs, après pulvérisation sur substrat de verre et réticulation à 500°C.*

îlots d'or dépendent bien de plusieurs paramètres, tels que le matériau du substrat, la température de recuit et l'épaisseur du film d'or qui avait été pulvérisé. Plus précisément nous avons observé un léger décalage vers le rouge de la bande SP, de 542 nm à 590 nm lorsque l'épaisseur du film d'or augmente de 2 nm à 12 nm (figure 5c). En deuxième lieu, une nouvelle méthode combinant l'écriture directe par laser, la pulvérisation et le recuit thermique est proposée pour obtenir des motifs plasmoniques en or à la demande (voir figure 6a). La résine photosensible S1805 est recouverte par pulvérisation de nano-couches d'or d'épaisseur variant de 10 nm à 24 nm. Les échantillons sont ensuite recuits thermiquement pour obtenir les structures plasmoniques. En particulier, en jouant sur le facteur de remplissage des structures de S1805, nous avons obtenu une structure métallique ayant une période qui est égale à la moitié de celle de la structure de S1805 (voir figure 6c). Il a été prouvé que cette méthode de fabrication était fiable et prometteuse pour l'obtention de structures plasmoniques.

En cinquième lieu, nous avons démontré une nouvelle méthode à une seule étape pour fabriquer des structures plasmoniques de nano-îlots en or par effet photo-thermique induit local par le système d'écriture directe par laser. Tout d'abord, nous avons mis en évidence le recuit-thermique d'un film de 6 nm d'or obtenu à partir d'un grand faisceau laser (diamètre 2 mm) de forte puissance (5 W). La zone métallique illuminée présente une couleur rougeâtre ce qui est confirmé par l'existence d'une bande SP à 545 nm. Puis nous avons réalisé un recuit thermique local, en focalisant le faisceau laser de faible puissance, dont le diamètre est de l'ordre de 300 nm. En fixant la puissance du laser à 40 mW et variant le temps d'exposition, à savoir 100 s, 80 s, 65 s et 50 s, nous avons obtenu des nanoparticules d'or qui donnent respectivement à des pics SP de 613,4 nm, 548,5 nm, 530,2 nm et 521 nm. Nous avons ainsi montré que le contrôle des bandes SP pouvait être utilisé dans plusieurs applications intéressantes. Pour cela, nous avons fabriqué une pièce de "un Euro" avec une contrôle de dose permettant obtenir des couleurs différentes. De plus, nous avons pu ainsi écrire des mots "NANO" avec de taille

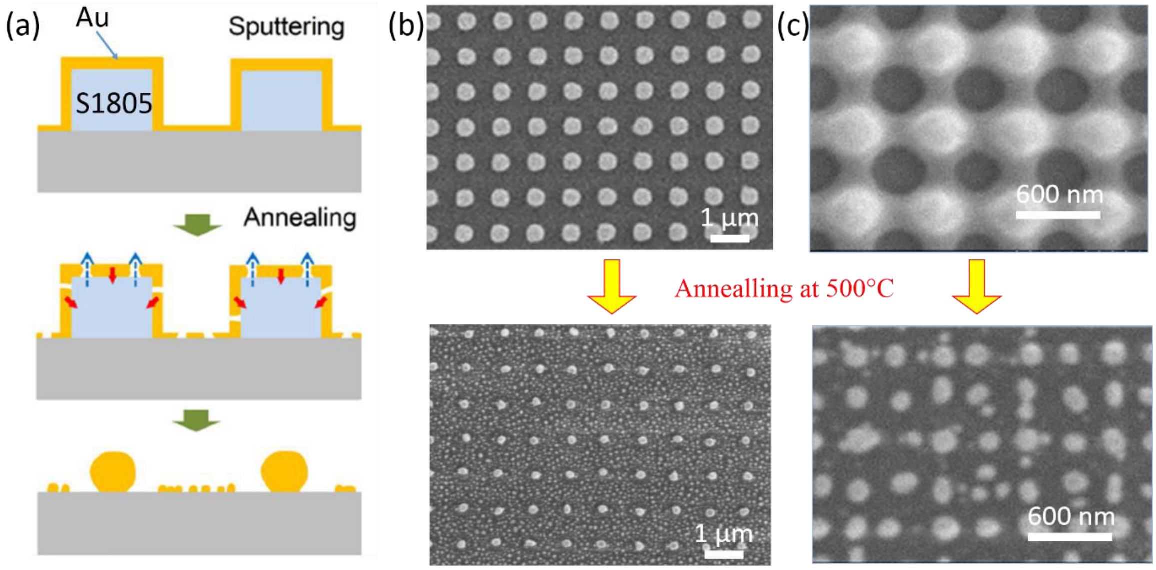

Figure 6. *(a) Schéma du mécanisme expliquant la formation de réseaux en or. (b), (c) Images au MEB de matrices photo-résine recouvertes de couches d'or pulvérisé (épaisseur = 10 nm) et la structure en or correspondante obtenue après réticulation à 500°C pendant 30 minutes.*

différente, allant jusqu'à 500 nm. Ces structures ont également été recouvertes par une couche protectrice en SU8. Ces structures ont été lues par une caméra CCD de haute résolution et par une technique d'imagerie fluorescente. Nous considérons que cette technique de fabrication directe peut être appliquée pour le stockage de données par l'effet plasmonique avec une capacité supérieure à celle de disque optique actuelle. Il faut souligner que l'écriture sur film d'or est respectueuse de l'environnement et que ces films d'or peuvent être recyclés.

Perspectives

Les futurs travaux peuvent être organisés en deux directions : optimisation de la technique de fabrication d'une part et application des structures obtenues.

Considérons tout d'abord la fabrication de nanostructures.

i) Par une méthode de recuit thermique on peut obtenir des structures métalliques avec une périodicité égale à la moitié de cette de la structure polymère. Cela permet de surmonter la limite de diffraction optique de la technique d'écriture laser directe. Des structures plasmoniques, 1D et 2D, devraient être fabriquées et examinées attentivement vis-à-vis de leurs propriétés optiques.

ii) Dans cette thèse, nous avons limité notre technique de fabrication pour des résines photosensibles positives et le matériau d'or. Néanmoins il est possible de développer cette technique de fabrication à d'autres matériaux comme l'argent ou le cuivre, et également des matériaux hybrides (composite polymère-inorganique ou polymère magnétique). Cela permet d'ouvrir beaucoup d'autres applications intéressantes.

iii) La souplesse de l'écriture directe par laser permet non seulement d'imprimer sur les substrats de verre les plus courant mais aussi sur des fibres optiques. La fabrication de structures photoniques sur fibre optique peut se révéler importante pour réaliser des capteurs, des filtres ou des lentilles optiques.

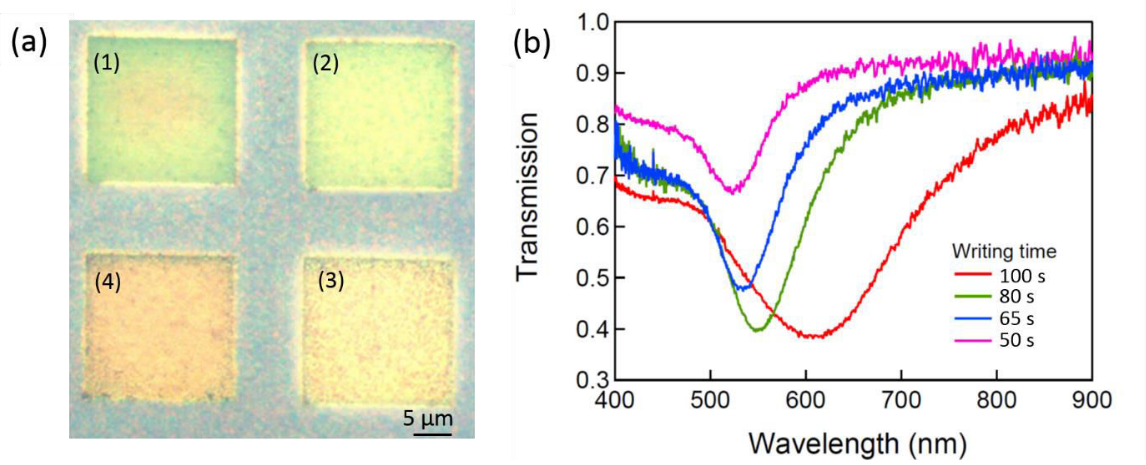

Figure 7. *Images microscopes (a) et spectres de transmissions (b) des nanoparticules d'or fabriquées par la méthode d'écriture directe par laser, par une puissance de 40 mW et avec les temps d'exposition différents: (1) 100 s, (2) 80 s, (3) 65 s, (4) 50 s.*

En ce qui concerne les applications, une optimisation des GNHA est nécessaire pour améliorer la sensibilité concernant la mesure d'indice de réfraction. L'argent serait un matériau à utiliser pour l'impression couleur car il possède des bandes SP qui couvre le domaine des longueurs d'onde du visible. Les structures cristaux photoniques 1D, 2D et 3D doivent elles aussi être optimisées pour des applications comme les miroirs ou les microcavités.